JPL PUBLICATION 81-49

An Analysis of Radio Interferometry with the Block 0 System

J. B. Thomas

December 15, 1981

National Aeronautics and
Space Administration

Jet Propulsion Laboratory
California Institute of Technology
Pasadena, California

JPL PUBLICATION 81-49

An Analysis of Radio Interferometry with the Block 0 System

J. B. Thomas

December 15, 1981

National Aeronautics and
Space Administration

Jet Propulsion Laboratory
California Institute of Technology
Pasadena, California

The research described in this publication was carried out by the Jet Propulsion Laboratory, California Institute of Technology, under contract with the National Aeronautics and Space Administration.

CONTENTS

APPENDIXES

Figures

Figures

Tables

DEFINITION OF SYMBOLS

$A(\hat{k},\omega)$ = random Fourier amplitude at frequency ω received from direction $\hat{k}$ for an extended source

A_s = solve-for amplitude in fringe fitting

$A(\omega)$ = random Fourier amplitude at frequency ω for point source

a_1 = first harmonic of quantized stopping function

$\vec{B}_r$ = retarded baseline

$\vec{B}(t)$ = instantaneous baseline vector

b = bit interval = 250 nsec for BLKO

C_s = coefficient in dual-band calibration

C_x = coefficient in dual-band calibration

c = speed of light

D_c = delay function

D_N = amplitude normalization

d_s = source diameter

$d(t)$ = normalized noise added to calibration signal

$d\Omega$ = differential solid angle

$E(\vec{x}, t)$ = electric field at $\vec{x}$, t.

F_q = quantization or fractional bit-shift filter

G_A = $D_N/(2W)$

$\overline{G^2}$ = average of square of bandpass amplitude across W.

$G_j(\omega)$ = bandpass amplitude at station j

$g(\omega_k)$ = amplitude normalization function, BAMPL

$h(\omega_k')$ = frequency-domain fringes

$\hat{k}$ = apparent wave vector

$\hat{k}_a$ = apparent wave vector from reference point in source

K_c = constant in charged particle delay equation

$\hat{k}_m$ = model for direction of source wave vector

ℓ = lag offset of correlator

ℓ_0 = lag value that produces largest fringe amplitude

N_ℓ = total number of lags in FFT over lag

N_c = number of BWS channels

N_e = differential integrated electron content

N_h = number of tones in passband

n_j = normalized additive noise, station j

N_t = number of bits in fringe-stopping sum

N_u = number of tones used

N_1, N_2 = upper and lower sum limits for FFT over lag

P_N = power of noise term associated with calibrator signal

P_s = total power of calibration signal

$Q(v)$ = sample function

q_r = normalized natural source signal

$r(t_G,\ell)$ = cross-correlation function

$R(u,v)$ = brightness transform

r_m = "calibrated" fringe amplitude

$S_p(\omega)$ = natural source power spectrum

$S(t)$ = total calibrator signal

$S_T(\omega)$ = frequency resolution function resulting from FFT over lag

t_G = common Greenwich time

t_o = true time "origin"

t_s = correlator reference time

t_z = reference time in fringe-fitting

t = true time

$\hat{t}_{bi}$ = shorthand for arguments in Equation 16

t_{bj} = bit time, station j

t_{cj} = ϕ-cal time, station j

T_n = additive noise temperature

T_q = natural source temperature

T_s = total or system noise temperature

u = component of sky-projected baseline vector in direction of declination in units of wavelength

$u_\ell(t_G)$ = complex stopped fringes for lag ℓ at time t_G

V_j = baseband voltage signal

v = component of sky-projected baseline vector in direction of declination in units of wavelength

$\bar{v}$ = average amplitude of tones in passband

v_f = fringe visibility = correlated flux/total flux

v_n = amplitude of nth harmonic of calibration signal

v_{sn} = stopped tone

W = nominal bandpass width = sample rate/2 = 2 MHz

W_b = actual width of rectangular bandpass

W_d = doppler shifted width of rectangular bandpass

$\vec{x}$ = position in geocentric coordinates

$\vec{x}_j(t)$ = location of station j as function of true time

$\vec{x}_{mj}$ = model for position of station j

y_j = doppler-shifted frequency, station j

z_j = normalized analog signal at station j

α = right ascension

β = structure coordinate in direction of right ascension

γ = structure coordinate in direction of declination

Δf_k = frequency separation of k^{th} pair

$\Delta\tau_{BWS}$ = residual BWS delay

$\Delta\tau_f$ = residual delay from fringe fitting

$\Delta\tau$ = residual delay in uncalibrated fringes

$\Delta\dot{\tau}_\phi$ = measured residual phase delay rate from phase slope

$\Delta\phi_f$ = stopped fringe phase

$\Delta\phi_h$ = "stopped heterodyne phase"

$\Delta\phi_j(\omega_n)$ = stopped phase of n^{th} tone station j

$\Delta\psi_c$ = corrected fringe phase

$\Delta\omega_c$ = true frequency minus nominal frequency

δ = declination

ε = tone power/total power

η_j = all noise added to recorded signal, station j

λ = wavelength of recorded radio signal

σ_k = error in delay for k^{th} BWS delay

σ_N = rms noise associated with calibration signal

σ_s = system noise error in phase for a single channel

σ_V = system noise on stopped tone

σ_ϕ = dispersive phase error for single channel

τ = geometric delay plus clock synch offset

τ_{aj} = antenna delay* before injection point, station j

---

*Use without subscript denotes difference j minus i

τ_{BWS} = final BWS delay

τ_{bj} = error in bit time*, station j

τ_{cj} = error in ϕ-cal time*, station j

τ_{e} = group delay due to charged particles

τ_{g} = conventional geometric delay

τ'_{g} = interim geometric delay

τ_{Ij} = instrumental group delay*, station j

τ_{m} = $\tau_{mi} - \tau_{mj}$

τ_{mj} = correlator model delay, station j

τ_{MA} = total model delay to be restored

τ_{mg} = model geometric delay restored

τ'_{mg} = model geometric delay removed

τ_{tj} = troposphere delay for station j

τ_{uj} = delay between clock reference point and ϕ-cal injection point, station j

τ_{ϕ} = final phase delay

$\tau_{\phi R}$ = delay concocted to represent phase-delay rate

$\dot{\tau}_{\phi s}$ = solve-for phase-delay rate in fringe fitting

ϕ_{B} = phase shift due to source structure

ϕ_{c} = oscillator phase at clock reference point

ϕ_{e} = phase effect due to charged particles

ϕ_{f} = total fringe phase

ϕ_{h} = total heterodyne phase shift

ϕ_{hj} = heterodyne phase shift, station j

*Use without subscript denotes difference j minus i

ϕ_{Ij} = instrumental phase shift*, station j

$\phi_m(t_G)$ = model phase for counter-rotation

ϕ_n = phase of n^{th} ϕ-cal tone at injection point

ϕ_s = solve-for phase in fringe fitting

$\phi_t(\omega_k)$ = calibration phase at frequency ω_k

ψ_j = signal phase at station j

ψ_n = stopping phase for n^{th} tone

ψ_s = total phase in fringe model

ω = RF frequency in geocentric coordinates

$\bar{\omega}$ = centroid frequency** of bandpass product, geocentric coordinates

ω_{BWS} = effective frequency for charged particle effect in BWS delay

ω_c = nominal oscillator frequency

ω_{eff} = effective frequency for charged particle effect in BSA delay and phase delay rate

ω'_k = $\omega_k - \omega_{hi}$ = baseband value for frequency ω_k

ω_n = frequency of n^{th} ϕ-cal tone

ω_z = reference frequency in fringe fitting

ω_{hj} = total heterodyne frequency**, station j

ω_t = true frequency

---

*Use without subscript denotes difference j minus i

**A primed value denotes best estimate

ABSTRACT

A second-generation data acquisition and reduction system is now being used at JPL to conduct long-baseline radio interferometry measurements. This system, called the Block 0 system, improves upon the previous 48-kbs system in many ways. Significant improvements include a higher recording rate of 4 Mbits/s, multichannel recording, multistation cross-correlation, phase calibration, S/X calibration of charged particle effects, and single-observation bandwidth synthesis. This report updates and improves the analysis previously performed for the 48-kbs system and traces the form and flow of information from signal reception to recorded bits at each station, through cross-correlation, phase-tracking, phase calibration, and bandwidth synthesis, to final observable formation. In this process, the data volume is greatly compressed for each observation, from $\sim 10^9$ bits on the station tapes to only four final observables: amplitude, delay, phase-delay rate and RF phase. It is shown that, after phase calibration and propagation media calibrations, the final delay observable is the sum of a geometric delay and a clock synchronization offset.

SECTION I

INTRODUCTION

Over the last few years, a second generation system for the acquisition and reduction of very long baseline interferometry (VLBI) data has been developed at JPL. In most respects, this second generation digital system, the Block 0 system, improves considerably on the previous 48-kbs digital system, most significantly by providing (a) a higher record rate of 4 Mbit/s, (b) multichannel recording, (c) multistation cross-correlation, (d) phase calibration, (e) dual-band calibration of charged particle effects and (f) single-observation bandwidth synthesis. Because of these improvements, many changes have been required in the data reduction theory. This report augments and modifies previous analyses (Ref. 1) to encompass the new features. Even though many improvements have been incorporated, some features of the BLKO system were not optimally designed due to various circumstances that prevailed during the development period. A new system now under development, the Block II system, will greatly improve upon the BLKO system, more nearly realizing the potential of VLBI.

The report is organized as follows. Section II provides a summary of the data-processing steps found in the BLKO system. Detailed derivation and analysis of those steps is presented in the subsequent sections. Section III gives fundamental definitions for basic time-keeping quantities. Section IV derives an expression for the recorded signal by tracing the signal from its free-space form through the instrumentation. In Section V, a non-relativistic model is developed for the "fast" fringes (cross-correlation function) produced by the BLKO correlator, the CIT/JPL Mark II correlator. In some respects, this part of the analysis repeats earlier work [1], but differs in important ways. Steps that are essentially the same are only summarized. One new feature is that instrumental terms are now grouped and defined in a more precise manner in order to demonstrate phase calibration through the use of tone phase. Further, the analysis treats delay offsetting of both bitstreams and provides an algorithm for correcting for the fractional-bit-shift errors introduced by the correlator. Section VI analyzes the fringe-stopping (counter-rotation) procedure used by the processor to compress the data. In Section VII, the stopped fringes are converted by a Fourier transform from the lag domain to the frequency domain. Transformation errors resulting from limited-lag reduction are discussed. Section VIII discusses phase calibration and derives an expression for the phase of a stopped tone. In Section IX, tone phase is used to correct fringe phase, thereby removing most instrumental effects and casting the phase into a form subject to simple interpretation. In Section X, the fringe model used in phase tracking is formulated to match the frequency-domain fringes generated by the Fourier transform. As in the lag domain, there are four estimated parameters: fringe amplitude, bit-stream-alignment (BSA) delay, fringe phase and phase-delay rate. Output amplitude is absolutely normalized to first approximation by removing known constant amplitude factors. Further, it is shown that BSA delay and phase delay are cast in the same form with regard to instrumental effects. Finally, Sections XI-XIV present detailed descriptions of the steps that produce the final values for delay and phase-delay rate. Those steps include observable formation, model improvement, propagation-media calibrations, and model restoration. It is shown that the final delay observable is the sum of a geometric delay and a clock synchronization offset.

SECTION II

SUMMARY OF THE BLKO SYSTEM

The BLKO system consists of several subsystems developed by a number of individuals from the Jet Propulsion Laboratory and the California Institute of Technology. The major subsystems and the people who developed them are data acquisition instrumentation (E. J. Cohen, G. S. Parks, E. H. Sigman, L. J. Skjerve, and D. J. Spitzmesser), phase calibrator (G. F. Lutes), correlator (M. S. Ewing and D. H. Rogstad) and postcorrelation software (G. H. Purcell, J. A. Scheid and J. B. Thomas). This report presents a theoretical analysis of the processing of a random broadband signal from a natural source and traces the signal from its free-space form to the final output observables of amplitude, delay, and phase-delay rate.

As shown schematically in Fig. 1, the random signal of a natural source received at an antenna at RF passes through various filters, amplifiers and mixers and a portion of it emerges at baseband spanning a 2-MHz-wide passband. Details of the instrumentation are not discussed here since the instrumental effects can be represented theoretically by a system bandpass function, a composite heterodyne signal, and composite phase shifts and delays. The instrumentation can switch a heterodyne signal through a sequence of frequencies so that the baseband signal cycles through a number of channels corresponding to 2-MHz windows at selected frequencies at RF. In this "time-multiplexed" multichannel mode, the dwell time on each channel can be as short as 0.2 seconds and as long as several seconds. The baseband signal is infinitely clipped, sampled at a 4-Mbit/s rate in a two-level mode and digitally recorded in a time-multiplexed format on magnetic tape by an IVC 825 or RCA 201 recorder. The several channels separated in frequency permit the subsequent reconstruction of a very wide effective bandwidth by a process called bandwidth synthesis (BWS).

When tapes from the antennas are sent to the correlator for data reduction, they are played back at the original data rate and corresponding frequency channels are cross-correlated. Multiple baselines (≤ 10) and multiple channels ($\lesssim 20$) can be simultaneously correlated. The output of the processor, called the stopped (or counter-rotated) fringes, is passed to post-correlation software that (a) transforms the fringes from the lag domain to the frequency domain, and (b) phase-tracks the transformed fringes to extract for each channel several time-specific values for amplitude, bit-stream alignment (BSA) delay, fringe phase and phase-delay rate. In the process, fringe phase is corrected by subtracting the phase obtained from calibration tones in order to remove unwanted instrumental effects.

The phase and BSA delay extracted from all channels can be used to obtain a final measured delay by means of bandwidth synthesis. This process first computes ambiguous delays by means of pairwise combinations of fringe phase from the different frequency channels. Ambiguities are then removed by a multistep process that begins with the unambiguous BSA delay and iteratively removes ambiguities in the BWS delays for ever-wider channel-pair separations until the widest separation (and most precise delay) is reached.

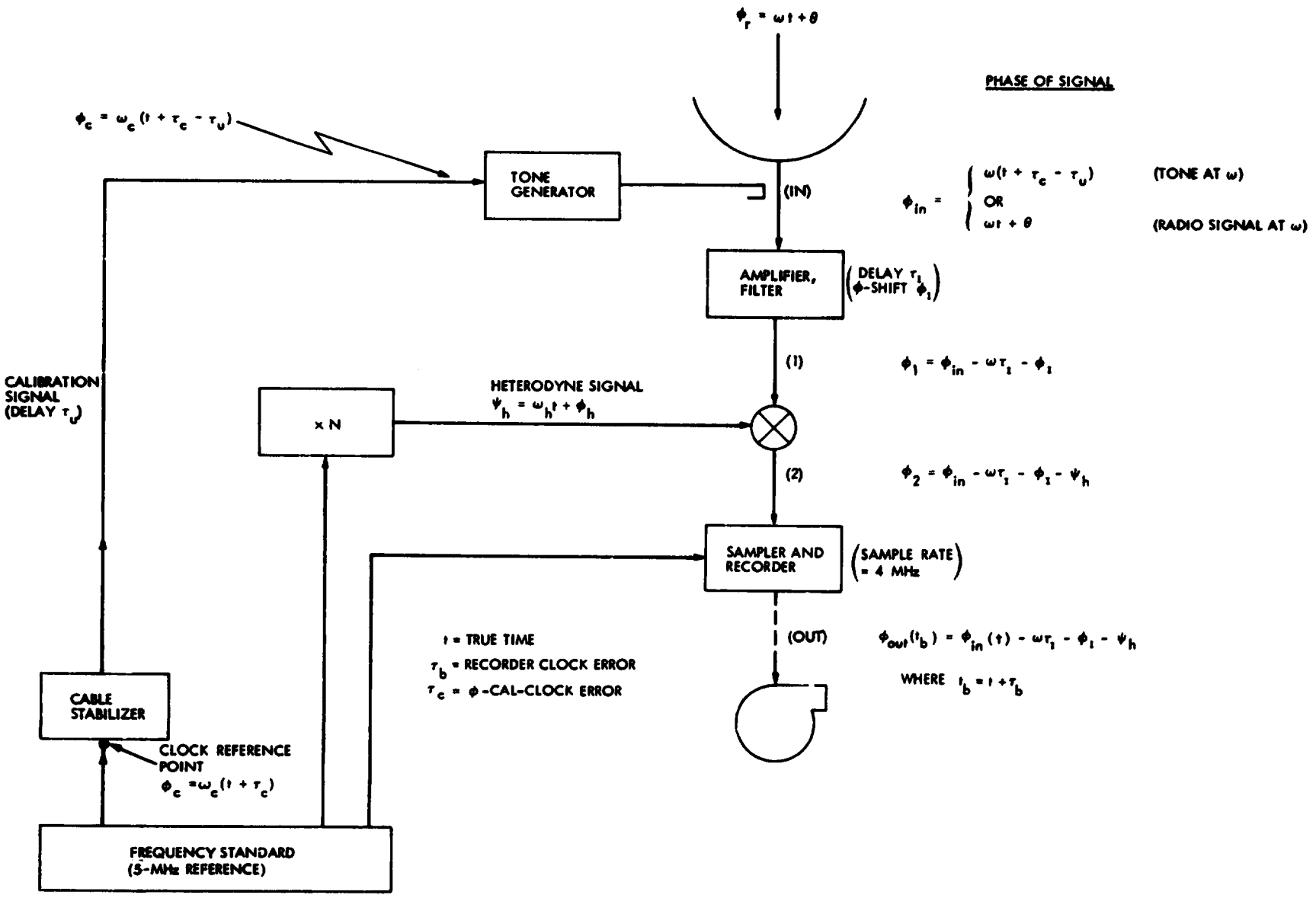

Fig. 1. Simplified illustration of antenna instrumentation

For each observation of a given source (1-10 minute duration), the output observables of the BLKO system are usually one composite value per channel for each of the following: fringe amplitude, fringe phase, phase-delay rate and BSA delay. Further, one value of BWS delay is obtained for each channel pair. From these observables, one can extract a best value of delay and of delay rate for subsequent processing. Currently, the "best" delay is usually the BWS delay from the most widely spaced channel pair. When two RF bands (typically 3.6 cm and 13 cm) are recorded, the final value for delay (delay rate) is obtained by combining the best values for delay (delay rate) from the two bands in a way that removes the effect of charged particles. The resulting delay should be equal to the sum of the geometric delay and the clock offset, while the delay rate is the time derivative of that delay.

A block diagram of the data reduction steps found in the current version of the BLKO system is presented in Appendix G. This report omits later data reduction steps that simultaneously fit the delay and delay-rate observables from many observations to obtain estimates for geophysical, astrometric and clock parameters.

SECTION III

CLOCK MODELING

Before proceeding to cross-correlation analysis, it will help to define a few time-keeping terms. First, define

t = true (universal)time

ω_t = true oscillator frequency (relative to true time)

ω_c = nominal oscillator frequency (e.g., 5 MHz)

Two "clocks" will be defined to assist in the analysis. The time of the first clock, the "recorder clock", is registered by the bits on the tape. This bit time is given in terms of true time by

$$\boxed{t_b = t + \tau_b} \tag{1}$$

where τ_b is the error in the recorder clock.

The second clock, the "ϕ-cal clock", will be established, at least conceptually, near the point where the 5-MHz signal from the station enters the phase calibrator instrumentation, as illustrated in Figure 1. The phase at this reference point is given in terms of true frequency by

$$\phi_c = \omega_t(t - t_o) \tag{2}$$

where t_o is the (unknown) true time at which $\phi_c = 0$. As implied by Eq. (2), we will assume that the oscillator is perfectly stable so that the only imperfections in the station clock are offsets in epoch and rate. If phase ϕ_c is measured at the reference point, ϕ-cal time can be defined by

$$t_c \equiv \phi_c/\omega_c \tag{3}$$

where we assume t_c is zero when ϕ_c is zero. This is possible since a particular zero crossing can be defined to be $t_c = 0$. If the nominal frequency is related to the true frequency by

$$\omega_c = \omega_t + \Delta\omega_c \tag{4}$$

then ϕ-cal time is related to true time by

$$\boxed{t_c = t + \tau_c} \tag{5}$$

where the clock error τ_c is given by

$$\tau_c \approx -\frac{\Delta\omega_c}{\omega_t}(t - t_o) - t_o \qquad (6)$$

Usually the difference between ω_c and ω_t is small, less than a part in 10^{11}.

It is conceptually and instrumentally convenient to define a clock in terms of a 1-pps signal that drives a counter to register the number of received pulses. To establish the 1-pps signal, a particular set of position-going zero crossings (one every 5×10^6 crossings for 5 MHz) must be selected. (Equivalently in Eq. (2), a definition of $\phi_c = 0$ must be made.) This arbitrary selection for the ϕ-cal clock leads to an ambiguity which must be resolved in BLKO clock synch measurements, as discussed in Appendix G. Clock synchronization with the BLKO system will be measured relative to the ϕ-cal clocks.

SECTION IV

THE RECORDED NATURAL SOURCE SIGNAL

This section derives an expression for the analog signal by tracking the incoming signal from its free-space form through the instrumentation to its final form at baseband. In this and subsequent sections, only a nonrelativistic theory will be considered.

In VLBI measurements, two antennas simultaneously receive the signal produced by a very distant, very compact natural source of random radio emissions. In this section, we will assume for simplicity that the natural source is a point source and leave it to Appendix A to generalize the analysis to an extended source. (That generalization greatly complicates the analysis but changes the final cross-correlation function only by inserting an additional factor in the amplitude and an additional term in phase.) Due to the great distance of the natural source, the incoming signal can be modeled by plane waves. Typical natural radio sources used in JPL VLBI work emit noise with a wide smooth frequency distribution. We can model one member of the random ensemble of noise waves as a superposition of plane waves in the form

$$E(\vec{x},t) = \int_{-\infty}^{\infty} A(\omega)\, \exp[i(\omega t - \vec{k} \cdot \vec{x})]\, d\omega \tag{7}$$

where E is the electric field at true time t and point $\vec{x}$, $\vec{k} = \omega\hat{k}/c$ is the apparent wave vector of the plane wave and gives the apparent direction of propagation, and $A(\omega)$ is the (random) Fourier amplitude at frequency ω. All quantities are measured with respect to a geocentric frame with axes defined by true equatorial coordinates of date. The adjective "apparent" refers to the aberration effect that will be observed in a geocentric frame. For simplicity, the wave is assumed to be linearly polarized. We will also assume at this point that the wave propagates in a vacuum and will not include propagation media effects. (Troposphere effects can be included as a simple additive group delay and would add little to the analysis. Space-charge effects are treated in Section XIV.)

Relative to the geocentric frame, the electric field at a given station becomes

$$E_j(t) = E\left(\vec{x}_j(t),t\right) = \int_{-\infty}^{\infty} A(\omega)\, \exp\left[i\left(\omega t - \vec{k} \cdot \vec{x}_j(t)\right)\right] \tag{8}$$

where $\vec{x}_j(t)$ is the location of station j as a function of true time. Station position is defined to be the intersection of axes of the antenna. (We will include below an instrumental delay τ_a to account for the fact that the natural source signal is injected at the horn rather than at the intersection of axes.) Phase is expressed in terms of true time since that time will be common to both antennas in a nonrelativistic analysis.

After injection, the signal passes through several filters and is heterodyned to baseband under the combined effect of various mixing signals. The phase effects of all intervening components can be grouped into three categories. First, the overall effect of the mixing signals can be described by one total mixing signal, $\omega_{hj}t_j + \phi_{hj}$, where ω_{hj} is the total mixing frequency and ϕ_{hj} represents both a constant phase offset and variations in mixing phase that are nonlinear in time. Second, all group delays after the injection point, including effective group delays through filters, can be represented by one total delay τ_{Ij}. Third, all instrumental phase shifts (except ϕ_{hj} and those of the form $\omega\tau_{Ij}$) can be represented by one total shift ϕ_{Ij}. We also include a term τ_a for delays before the tone injection point. This delay is defined to be the difference in path length for the radio wave in its actual propagation to the tone injection point and its theoretical propagation to the intersection of axes. This delay is necessitated by the definition of station location and is theoretically incorporated by delaying the incoming plane wave. The formulation with τ_a assumes that dispersive phase shifts above the injection point are negligible. If they are not, then additional calibrations will be required to remove them.

Figure 1 schematically illustrates the modifications to signal phase as the signal progresses through the instrumentation from injection to recorder. The block diagram has been simplified to show only one element of each type with token phase shifts and group delays. Nevertheless, the following analysis is quite general if the variables are properly defined to represent lumped effects of all the elements in an actual system.

When the lumped instrumental effects are included, the doppler-shifted analog signal at baseband for a given BWS channel at station j at bit time t_{bj} can be written in the form

$$V_j(t_{bj}) = \int_0^\infty A(\omega)\, G_j(y_j)\, e^{i\psi_j}\, d\omega + \text{c.c.} + n_j \tag{9}$$

where

$$y_j = \omega(1 - \hat{k} \cdot \dot{\vec{x}}_j/c) \tag{10}$$

$$\psi_j = \omega(t_j - \tau_{aj}) - \vec{k} \cdot \vec{x}_j(t_j) - \omega_{hj}\, t_j - \phi_{hj} - y_j\, \tau_{Ij} - \phi_{Ij}(y_j) \tag{11}$$

In this expression, G_j is the amplitude of the system bandpass, n_j is additive noise, y_j is the doppler-shifted (station) frequency corresponding to ω and c.c. denotes complex conjugate. The time argument t_j is the true time corresponding to bit time t_{bj} (see Eq. 1).

In the BLKO system, the signal is sampled at a 4-Mbit/s rate and recorded in a bilevel mode. That is, one bit is recorded for each sample point and that bit is 1 if the signal is positive and 0 if the signal is negative. In subsequent analysis, we will ignore this bit code and act as though +1 or -1 were directly recorded on the tape.

Before proceeding to cross-correlation analysis, we will reformulate the expression for the analog signal so all components are normalized in the measured units of noise temperature. For station j, let the normalized analog signal corresponding to V_j be given by

$$z_j(t) = \left[\sqrt{T_{qj}}\, q_j(t) + \sqrt{T_{nj}}\, n_j(t)\right] \Big/ \sqrt{T_{sj}} \qquad (12)$$

where z, q, n are the total signal, natural source signal (first two terms in Equation 9) and additive noise (last term in Eq. 9), respectively. We will assume these quantities are all normalized so that

$$\langle z^2 \rangle = \langle q^2 \rangle = \langle n^2 \rangle = 1 \qquad (13)$$

The quantities T_s, T_q, T_n are the noise temperatures for the total signal, the natural source and additive noise respectively. It is assumed that the spectral power for each noise source is fairly constant across the 2-MHz passband so that one average noise temperature can describe the whole passband. (The noise power per passband is actually kT_sW, but the factor kW drops out in the ratios.) As we shall see, the normalized form in Eq. (12) is more convenient for cross-correlation analysis.

SECTION V

THE CROSS-CORRELATION FUNCTION

The BLKO correlator (the CIT/JPL Mark II correlator) aligns the bits on the two tapes, multiplies them bitwise and fringe-stops (counter-rotates) the resulting fringes. This section develops a detailed model for the cross-correlation function, the expectation value of the product* of the aligned signals. We will explicitly treat only one frequency channel, with the understanding that the correlator also processes the other channels in their time sequence.

The expectation value of the bitstream product, the cross-correlation function (fast fringes), is defined by

$$r(t_G, \ell) \equiv \langle \tilde{V}_i(t_{bi} - \tilde{\tau}_{mi} - \ell b)\, \tilde{V}_j(t_{bj} - \tilde{\tau}_{mj}) \rangle \tag{14}$$

where $\tilde{\tau}_{mi}$, $\tilde{\tau}_{mj}$ are model delays used to offset the two bitstreams (see Appendix B). We will use a tilde to denote a digital or quantized version of a quantity as for the two-level value (± 1) for $\tilde{V}_i$ and for the lag ($\tilde{\tau}_{mi}$), which is quantized to the nearest bit. The term ℓb explicitly represents arbitrary lag offsets (ℓ = -7 to +8) about the central lag of the correlator, by offsetting bitstream i in units of the bit interval b. For the BLKO system, b is equal to $(4\ \text{Mbit/s})^{-1}$ or 250 nsec. The argument t_G is the common Greenwich time defined by the bits on the two tapes. That is, the correlator implicitly enforces the assumption that

$$t_{bi} = t_{bj} \equiv t_G \tag{15}$$

and uses t_G as the time tag.

The van Vleck relation (Ref. 2) gives the cross-correlation function in Eq. (14) in terms of the analog signals:

$$r(t_G, \ell) \approx \frac{2}{\pi} \frac{\langle V_i(t_{bi} - \tilde{\tau}_{mi} - \ell b)\, V_j(t_{bj} - \tilde{\tau}_{mj}) \rangle}{\sqrt{\langle v_i^2 \rangle \langle v_j^2 \rangle}} \tag{16}$$

*In the BLKO correlator, one bit stream is first multiplied by a stopping sinusoid and the resulting product is multiplied by the other bitstream, as explained in Appendix B. Since multiplication is associative, we will reverse the actual order for clarity.

where small correlated amplitude ($r << 1$) has been assumed. (In typical VLBI measurements, one finds $r < 0.2$.) With the normalized representation of the preceding section, the expectation of the normalized voltage product in Eq. (16) becomes

$$\frac{\langle V_i(\hat{t}_{bi})\, V_j(\hat{t}_{bj})\rangle}{\sqrt{\langle V_i^2\rangle \langle V_j^2\rangle}} \equiv \langle z_i(\hat{t}_{bi})\, z_j(\hat{t}_{bj})\rangle \tag{17}$$

$$= \sqrt{\frac{T_{qi}\, T_{qj}}{T_{si}\, T_{sj}}}\ \langle q_i(\hat{t}_{bi}) q_j(\hat{t}_{bj})\rangle \tag{18}$$

since the additive noise n_j is uncorrelated between stations. The arguments $\hat{t}_{bj}$ are shorthand for the sums of terms that are the arguments in Eq. (16). Thus the problem is reduced to finding the correlation between the normalized natural source components (q_k) for the two stations, with the overall amplitude scaled by a multiplicative system temperature factor. Note that this factor times $2/\pi$ gives the amplitude of the cross-correlation function for perfectly correlated natural source components (i.e., $\langle q_i q_j\rangle = 1.0$).

We will now present on the basis of a plausibility discussion the final form for the cross-correlation function. A complete derivation is given in Appendix A, including the effects of source extent and the random nature of the source signal.

The natural source signal q is given by the first two terms in Eq. (9), normalized to have unit power. Thus the product $q_i\, q_j$ is given by a double integral over frequency where the integrand includes the sum of two products of the form $A(\omega)A^*(\omega')$ and $A(\omega)A(\omega')$. Under the expectation-value operation, only the product $\langle A(\omega)A^*(\omega')\rangle$ has a non-zero value and this occurs as a delta function at $\omega = \omega'$. (For a stationary random signal such as that from a natural source, the amplitude at one frequency is uncorrelated with the amplitude at another frequency.) Thus, the double integral over frequency collapses to a single integral over frequency with one term in the integrand. If we let $S_p(\omega)$ denote the source power spectrum arising from $\langle A(\omega)A^*(\omega)\rangle$, the cross correlation function becomes

$$r(t_G, \ell) = \frac{2}{\pi} \frac{r_m}{2} \frac{1}{D_N} \int_0^\infty S_p(\omega)\, G_i(y_i)\, G_j(y_j)\, e^{i\phi_f}\, d\omega + \text{c.c.} \tag{19}$$

where

$$r_m \equiv v_f \sqrt{\frac{T_{qi}\, T_{qj}}{T_{si}\, T_{sj}}} \tag{20}$$

$$D_N^2 \equiv \int_0^\infty S_p(\omega)\, G_i^2(y_i) d\omega \int_0^\infty S_p(\omega)\, G_j^2(y_j) d\omega \tag{21}$$

$$\begin{aligned} \phi_f \equiv\ & \phi_h - \omega_{hj}\, \tilde{\tau}_{mj} + \omega_{hi}\, (\tilde{\tau}_{mi} + \ell b) \\ & + \vec{k}_a \cdot \left[\vec{x}_j(t_j - \tilde{\tau}_{mj}) - x_i(\tilde{t}_i - \tau_{mi} - \ell b)\right] \\ & + \omega(\tau_b + \tau_I + \tau_a - \tilde{\tau}_{mi} + \tilde{\tau}_{mj} - \ell b) + \phi_I + \phi_B \end{aligned} \tag{22}$$

in which

$$\phi_h = (\omega_{hj} t_j + \phi_{hj}) - (\omega_{hi} t_i + \phi_{hi}) \tag{23}$$

and τ_b, τ_I, τ_a, and ϕ_I are differences between the corresponding station quantities in the order j minus i.

The terms in the cross-correlation function in Eq. (19) can be explained as follows. Normalization of the signal in terms of system temperature generates the factor r_m, as suggested by the derivation of Eq. (18). Included in r_m is the fringe visibility v_f, which is equal to the correlated flux divided by the total flux. This factor and a brightness transform phase shift ϕ_B are two of the three modifications to the final cross-correlation function when the analysis is generalized to include extended sources (see Appendix A). The third modification is to change the point-source wave direction $\hat{k}$ to $\hat{k}_a$, a wave direction defined relative to a somewhat arbitrary reference point within the extended source. The factor of $2/\pi$ is the amplitude loss due to two-level sampling (see Eq. 16). The factor of 1/2 is a consequence of complex representation of the fringes and gives the proper definition for the power spectrum S_p (i.e., by cancelling the factor of 2 gained when the complex conjugate in Eq. (19) is added to obtain a real number for the cross-correlation function).

In the denominator, the quantity D_N^2 is the product of the total source power from the two stations and arises from the normalization of the natural source components at each station (that is, from the requirement $\langle q_i^2 \rangle = \langle q_j^2 \rangle = 1$). Note that, as one would expect, the total power at each station is equal to the integrated power across the passband where the power at each frequency is given by the spectral power of the natural source multiplied by the square of the bandpass amplitude.

Within the integral in Eq. (19), the various terms can be explained as follows. Since a component of the natural source signal at one frequency is uncorrelated with a component at any other frequency, the correlated signal can

be obtained by multiplying each frequency component at one station by the corresponding component at the other station and summing over all frequencies. By corresponding frequency components, we mean the components with the same frequency in geocentric coordinates. Due to the earth's rotation, a given geocentric frequency will be doppler shifted when measured by station instrumentation. Those shifts are accounted for by the doppler-shifted arguments y_k in the bandpass functions G_k.

Since interferometers are differencing devices, the phase ϕ_f in Eqs. (19) and (22) is the difference in the phase for the two stations, each with the proper offset in time. All of the phase terms in Eq. (22) can be derived in this manner except for three which involve special considerations. First, the brightness transform phase ϕ_B is a consequence of source structure as shown in Appendix A and is included without proof. Second, in the instrumental delay terms $y_j \tau_{Ij}$, we have neglected small doppler effects of the order

$$(\hat{k}_a \cdot \dot{\vec{x}}_j/c)\, \tau_{Ij} \lesssim 10^{-6} * 10^{-6} \text{ sec} = 10^{-12} \text{ sec} \tag{24}$$

which can shift the phase by 0.01 cycle at X-band. In practice these small doppler terms can be removed by applying a correction based on instrumental group delay, if necessary. Third, the quantity τ_b arises from the difference $t_i - t_j$ which, through the use of Eq. (1) plus (15), can be shown to equal

$$t_i - t_j = \tau_{bj} - \tau_{bi} = \tau_b \tag{25}$$

where τ_{bk} is the total error in bit time at station k.

Introduction of τ_g', an interim delay approximately equal to the usual geometric delay, simplifies fringe phase ϕ_f. We define τ_g' by

$$\omega\tau_g' \equiv \vec{k}_a \cdot \left[\vec{x}_j(t_j - \tilde{\tau}_{mj}) - \vec{x}_i(t_i - \tilde{\tau}_{mi} - \ell b)\right] \tag{26}$$

This delay is discussed in Section XII. Note that τ_g' depends weakly on ℓ, so that X-band phase changes by less than 0.005 cycle when one lag is traversed. In the following analysis, we neglect this dependence and evaluate τ_g' at ℓ_o, the lag with peak fringe amplitude. Since this lag dependence can be accurately modeled, it can be easily accounted for during processing, if necessary. When Eq. (26) is substituted into Eq. (22), fringe phase becomes

$$\begin{aligned}\phi_f = {} & \phi_h - \omega_{hj}\,\tilde{\tau}_{mj} + \omega_{hi}\,(\tilde{\tau}_{mi} + \ell b) \\ & + \omega(\tau_g' + \tau_b + \tau_I + \tau_a - \tilde{\tau}_{mi} + \tilde{\tau}_{mj} - \ell b) + \phi_I + \phi_B\end{aligned} \tag{27}$$

The phase rate $\dot{\phi}_f$ can reach about 20 kHz at X-band. Therefore, before the data can be compressed by summing over bits, the fringe phase must be counter-rotated to a very low rate (<0.1 Hz). The next section discusses that procedure.

SECTION VI

FRINGE COUNTER-ROTATION

In most observations of natural sources, the system noise is much greater than the correlated amplitude so that the SNR for a single bit product (Eq. 19) is very small (0.0002 - 0.2). Thus many bits of data ($\sim 10^4$ - 10^9) must be collected to raise the SNR to a usable level. However, due to the high phase rate that the fast fringes typically possess (as high as 20 kHz at X-band), the data volume cannot be compressed by directly summing the fringes over time (bits). This section explains fringe stopping, a process that counter-rotates the fringes (i.e., digitally heterodynes the fringes to a low frequency) and thereby allows sums over an interval of time (correlation interval) that compress an observation containing many bits ($\sim 10^8$ to 10^9) into a relatively small number (100 - 1000) of points (correlation coefficients). In addition to permitting a massive data compression, counter-rotation can, with modification, partially remove the effects of model-delay quantization, as we shall see.

For fringe stopping to be successful, the model phase and model delay used by the correlator must accurately reproduce the time dependence of the actual fringes. Specifically, to avoid significant losses in amplitude in the output fringes, the geometric model must be accurate to a part in 10^6 or better. The model phase can then be constructed with sufficient accuracy to insure that only a small fraction of a cycle of the stopped fringes will be traversed in a correlation interval (e.g., 20 kHz $\times$ 10^{-6} $\times$ 1 sec = 0.02 cycle). Thus, amplitude loss due to incoherent addition can be avoided. We will assume the correlator model delay is sufficiently accurate.

The model phase* used by the correlator for counterrotation is given by

$$\phi_m(t_G) = (\omega'_{hj} - \omega'_{hi})(t_{bi} - t_s) - \omega'_{hj}\,\tilde{\tau}_{mj} + \omega'_{hi}\,\tilde{\tau}_{mi} + \bar{\omega}'(\tilde{\tau}_{mj} - \tau_{mj} - \tilde{\tau}_{mi} + \tau_{mi}) \qquad (28)$$

where ω'_{hn} is the best estimate of ω_{hn} and $\bar{\omega}'$ is the best estimate of the centroid ($\bar{\omega}$) of the bandpass product. The time t_s is a reference time adopted at the correlator and is usually the start of the observation. The last three terms involving quantized delays are designed to remove the average quantization effect from the overall stopped phase (at effective frequency $\bar{\omega}$).

To counter-rotate, the voltage product discussed in Section V is multiplied at each bit by the appropriate model phasor and summed over N_t bits within a correlation interval, producing one complex value for the fringes for that interval:

$$u_\ell(t_G) = \frac{1}{N_t} \sum_{t'_G} \tilde{V}_i(t'_G - \tilde{\tau}_{mi} - \ell s)\, \tilde{V}_j(t'_G - \tilde{\tau}_{mj})\, e^{-i\phi_m(t'_G)} \qquad (29)$$

*For simplicity, we will neglect a constant-frequency term that can be included in model phase.

where Σ denotes a sum over the bits in the interval and t_G is now the common bit time at the middle of that interval. (As explained above through Eq. 15, t'_G is the Greenwich time defined by both bitstreams.) The sum interval (correlation interval), which ranges from 0.2 seconds to several seconds and contains at least 8×10^5 bits, is equal to the total dwell time for the given BWS channel within a multiplexing cycle. By combining Eq. (14) with the expectation value of Eq. (29), one finds that the expectation value for the complex stopped fringes is given by

$$\langle u_\ell(t_G) \rangle = \frac{1}{N_t} \sum_{t'_G} r(t'_G, \ell)\ e^{-i\phi_m(t'_G)} \tag{30}$$

When Eq. (19) is substituted for $r(t,\ell)$, two terms result: a sum-frequency term and a difference-frequency term. For sufficiently high fringe rates ($\dot{\phi}_f \gtrsim 100$ Hz), the sum-frequency term essentially averages to zero in the sum over time leaving only the difference term:

$$\langle u_\ell(t_G) \rangle = \frac{1}{N_t} \frac{1}{\pi} \frac{r_m}{D_N} \sum_{t'_G} \int_0^\infty S_p\ G_i\ G_j\ e^{i\Delta\phi_f}\ d\omega \tag{31}$$

where the stopped phase is given theoretically by

$$\Delta\phi_f \equiv \phi_f - \phi_m \tag{32}$$

$$= \Delta\phi_h + \omega\Delta\tau + \phi_I - (\omega - \omega_{hi})\ \ell b + (\omega - \bar{\omega}')\ (\tau_m - \tilde{\tau}_m) + \phi_B \tag{33}$$

for which we have made the definitions

$$\Delta\tau \equiv \tau'_g + \tau_b + \tau_I + \tau_a - \tau_m \tag{34}$$

$$\Delta\phi_h \equiv \phi_h - (\omega'_{hj} - \omega'_{hi})\ (t_{bi} - t_s) \tag{35}$$

$$\tau_m \equiv \tau_{mi} - \tau_{mj} \tag{36}$$

Two terms of the form $(\omega_{hj} - \omega'_{hj})\tilde{\tau}_{mj}$ that are of the order of 10^{-4} cycle or less have been omitted. We would emphasize that τ_m is the model delay used by the correlator at the central lag ($\ell = 0$).

The fringe-stopping analysis in this section ignores the fact that the BLKO correlator actually uses a trilevel quantized model for the stopping sinusoids, as explained in Appendix B. We will assume that the use of such a model changes the amplitude of the stopped fringes by a multiplicative factor but otherwise will not significantly change Eq. (31). That multiplicative factor is the

amplitude of the first harmonic of the quantized stopping sinusoid and is equal to 1.176 for the quantization scheme used in the BLKO correlator (see Appendix B). One can see how this amplitude factor enters by expanding the quantized sinusoid in terms of its harmonics and showing that only the first harmonic beats the cross-correlation signal to a low frequency. That is, the sum over correlation interval filters out all terms except this low frequency term. Thus, except for the coefficient of the first harmonic, the resulting fringes are assumed to be the same form as those generated by the pure stopping function of this section. Exceptions can occur in special cases due to interactions between various frequency components in the signal and stopping function, but those cases will not be treated in this report.

The theoretical expression for the stopped fringes can be rewritten by interchanging the sum and integral in Eq. (31) to obtain

$$\langle u_\ell(t_G)\rangle = \frac{a_1}{\pi}\frac{r_m}{D_N}\int_o^\infty S_p(\omega)\, G_i(y_i)\, G_j(y_j)\, F_q\, e^{i[\Delta\psi_f - (\omega-\omega_{hi})\ell b]}\, d\omega \qquad (37)$$

where

$$\Delta\psi_f \equiv \Delta\phi_h + \omega\Delta\tau + \phi_I + \phi_B \qquad (38)$$

$$F_q(\omega - \bar{\omega}') \equiv \frac{1}{N_t}\sum_{t'_G} e^{i(\omega - \bar{\omega}')\,(\tau_m - \tilde{\tau}_m)} \qquad (39)$$

The factor a_1 has been inserted to account for quantization of the stopping sinusoid, as discussed above. The sum over time has been applied only to the "quantized-delay phasor" (from fifth term in Eq. 33) since the time variation of that factor will dominate when an accurate model delay is used. That is, the rate of the residual phase ($\Delta\psi_f$) can be made very small ($\lesssim$0.01 Hz) so that the phase $\Delta\psi_f$ will change by only a small amount ($\lesssim$0.01 cycle) over a sum interval ($\sim$1.0 second). On the other hand, the phase $(\omega-\bar{\omega}')$ $(\tau_m-\tilde{\tau}_m)$ changes by 0.25 cycle over a delay quantization update interval, which can be as small as 0.1 second. As explained in Appendix D, the quantization filter F_q can easily be calculated on the basis of delay quantization history. Exceptions to the above assumption of small residual rate can occur in "initialization" runs involving a poorly known baseline or source position. However, this will occur only for the first pass through the correlator since the results of that pass can be used to improve the a priori for all subsequent passes involving that baseline or source.

In the BLKO correlator, correlation sums are made over time intervals that are often large compared to the delay quantization update interval (bit-jump interval). An alternate correlator design is to form intermediate sums for very short intervals over which the delay quantization error changes only by a small

fraction of a bit. For each of these shorter intervals, the correlator would perform a Fourier transform from the lag domain to the frequency domain. After the transformation, the quantization error appears purely as a phase effect that can then be removed by appropriately counterrotating fringe phase. This approach produces a slightly better SNR (by 0 to 3.5%) than the BLKO system because the correlated signal is added coherently for each frequency across the 2-MHz passband. However, it also increases the complexity and cost of the correlator. By accepting a small loss in SNR, the BLKO system can employ a simpler correlator and let postcorrelation software handle the quantization problem with the quantization filter F_q. Even though the quantization problem itself does not necessarily require it, the postcorrelation software (i.e., the phase tracking program) does eventually transform to the frequency domain for other reasons, as discussed in the next section.

SECTION VII

TRANSFORMING TO THE FREQUENCY DOMAIN

After the stopped fringes leave the correlator, they are passed to the phase-tracking program (PHASOR). In the present version of PHASOR, the stopped fringes are Fourier transformed from the lag domain to the frequency domain. The reasons for this transformation are as follows. In the lag domain, the phase is implicitly referenced to the true centroid frequency, which depends on bandpass shape. Since this reference frequency enters in the calculation of BWS delay, uncertainties in bandpass shape can introduce errors in BWS delay. In the frequency domain, an exact reference frequency can be forced on the data so that output phase will not depend on bandpass shape. Thus, frequency-domain analysis eliminates a possible source of error and avoids the operational burden of precisely determining bandpass shape, at least for phase measurements. However, for the most precise measurements of correlated amplitude, it may be necessary to determine bandpass shape accurately.

One disadvantage of the frequency domain approach is that, in practical applications, a Fourier transform can introduce phase errors. Those errors arise because in practice only a small number of lags can be summed in the transform, leading to poor resolution ($\approx$ bandwidth/4) in the frequency domain. However, accuracy studies show that the errors introduced are not as serious as one might guess. When complex fringes based on typical bandpass shapes were simulated (see Appendix E), it was found that a nine-lag transform reproduced the actual overall input phase to better than 0.1 millicycle (with the peak amplitude placed at the central lag to within 0.5 bit). For a nearly rectangular bandpass, the "odd" frequencies (n/2N, n odd) more accurately reproduced the input phase than did the "even" frequencies. The transformed shape deviated from the input shape by as much as 9% for the 9-lag transform. These amplitude deviations should be no problem since the transformed shape can be modeled if the actual bandpass shape is known. An alternate approach is to determine directly the transformed shape by measuring for a strong source of known strength the amplitude of the cross-correlated signal in each frequency bin of the frequency-domain fringes.

Two other considerations arise in the choice between domains — phase calibration and fractional-bit-shift correction. Both of these corrections can be carried out in either domain, although they are more easily applied in the frequency domain. Thus, primarily because of the decoupling of phase from amplitude, frequency domain analysis appears to be the preferred approach in phase-tracking and that approach has been followed.

The remainder of this section transforms the fringes from the lag domain (Eq. 39) to the frequency domain. For reference, Appendix C reformulates the lag-domain fringes to cast them in a form used in the past.

Before transforming to the frequency domain, one must detect the fringes and determine which lag offset produces the largest fringe amplitude. This is accomplished by performing an FFT over time on the fringes for each lag offset within a lag range believed to contain fringe power. The output of these FFT's can be viewed as a function of lag and frequency (where the frequency variable

is fringe frequency associated with time dependence rather than observing frequency). The amplitudes of the FFT points are searched over lag and fringe frequency to determine which lag and which frequency bin has the largest amplitude. The maximum amplitude is checked to verify that it exceeds the SNR threshold. Only fringes for lags near this central lag are used in subsequent processing.

The stopped fringes for each correlation interval (Eq. 37) are transformed to the frequency domain by a discrete Fourier transform over a subset of the 16 lags passed by the correlator:

$$h(\omega_k') = \sum_{\ell'=N_1}^{N_2} u_{\ell_o+\ell'} \, e^{i\omega_k'\ell' b} \tag{40}$$

where b is the interval, ℓ_o is the central lag with the largest amplitude and ℓ' is summed over N_ℓ lags centered about ℓ_o ($N_\ell = N_2 - N_1 + 1$). In the present BLKO system, a 9-lag transform is used since the phase errors associated with a nine-lag transform are apparently the best for values of N_ℓ less than 12 (see Appendix E). For $N_\ell = 9$, we would have $N_1 = -4$ and $N_2 = 4$. The frequencies ω_k' are baseband frequencies spaced at equal intervals across the system passband. To obtain an adequate sampling rate in the frequency domain while maintaining statistical independence of the noise on the transformed points $h(\omega_k')$, the frequencies are given the spacing

$$\frac{|\omega_{k+1}' - \omega_k'|}{2\pi} = \frac{1}{N_\ell b} \tag{41}$$

As observed above, the "odd" frequencies give the best phase accuracy so we will use

$$\frac{|\omega_k'|}{2\pi} = \frac{2k-1}{2N_\ell b}, \quad k = 1, 2, \ldots \tag{42}$$

$$= \frac{2k-1}{N_\ell} W \tag{43}$$

where W is the nominal channel bandwidth of 2 MHz (half the sample rate). For $N_\ell = 9$ only the fringes associated with the first four values of k (i.e., k = 1 to 4) have significant amplitude. The frequency values for these points are W/9, 3W/9, 5W/9, 7W/9. The point at W (k = 5) has very small amplitude for the BLKO passband.

Some of the comments found earlier in this section can be clarified by calculating the expectation value for the transformed fringes:

$$\langle h(\omega_k') \rangle = \sum_{\ell'} \langle u_{\ell_o+\ell'} \rangle \, e^{\pm i|\omega_k'|\ell' b} \tag{44}$$

where $\omega_k' = \pm|\omega_k'|$ and where the plus (minus) sign is used for USB (LSB). The sign selection depends on the sign of $\omega-\omega_{hi}$, which is positive for upper sideband (USB) and negative for lower sideband (LSB). By substituting the expression for $\langle u_\ell \rangle$ found in Eq. (37) and interchanging the sum and integral, one obtains

$$\langle h(\omega_k') \rangle = \frac{a_1}{\pi} \frac{r_m}{D_N} \int_o^\infty S_p\, G_i\, G_j\, F_q\, S_T(\omega'-\omega_k')\, e^{i(\Delta\psi_f - \omega' \ell_o b)}\, d\omega' \qquad (45)$$

where

$$\omega' = \omega - \omega_{hi} \qquad (46)$$

$$S_T(\Delta\omega) = e^{i\Delta\omega(N_1+N_2)b/2}\, \frac{\sin(\Delta\omega N_\ell b/2)}{\sin(\Delta\omega\, b/2)} \qquad (47)$$

One can show

$$\lim_{N_\ell \to \infty} S_T(\Delta\omega) = 4\pi W\, \delta(\Delta\omega) \qquad (48)$$

where $\delta(x)$ is the delta or impulse function. Thus, for an infinite number of lags we would obtain precisely the cross-correlation spectrum:

$$\boxed{\langle h(\omega_k') \rangle = \frac{2}{\pi} a_1\, r_m\, \frac{S_p(\omega_k)\, G_i(y_{ik})\, G_j(y_{jk})}{G_A}\, F_q\, e^{i\Delta\psi_f \mp i|\omega_k'|\ell_o b} \quad \begin{pmatrix} - \text{ for USB} \\ + \text{ for LSB} \end{pmatrix}} \qquad (49)$$

where

$$G_A \equiv \frac{D_N}{2\pi W} \qquad (50)$$

and

$$\boxed{\Delta\psi_f = \Delta\phi_h + \omega_k\, (\tau_g' + \tau_b + \tau_I + \tau_a - \tau_m) + \phi_I + \phi_B} \qquad (51)$$

$$y_{ik} = \omega_k\, (1 - \hat{k}\cdot\dot{\vec{x}}_i/c) \qquad (52)$$

There are practical limits to the number of lags that can be transformed. For example, as more lags are used, the power is spread over more points in frequency, making data reduction more costly. Further, the cost of the correlator increases as the number of lags increases. On the other hand, transformation errors decrease as the number of lags increases. A reasonable compromise for the BLKO system appears to be 9 lags. For this value, the power is spread over a manageable number of points (4) in the frequency domain while transformation errors are fairly small, as discussed in Appendix E.

In the following analysis, we neglect the small transformation errors and use Eq. (51) to describe the phase in the frequency domain. If necessary, the transformation errors can be corrected to a large extent through modeling.

It is informative to note that, for a flat power spectrum S_p and for identical bandpass shapes at the two stations, the bandpass ratio in Eq. (49) can be converted through the use of Eqs. (21) and (50) to the form

$$\frac{S_p\, G_i(y_{ik})\, G_j(y_{jk})}{G_A} \approx \frac{G^2(\omega_k)}{\overline{G^2}} \tag{53}$$

where the bar denotes an average across the passband. We have assumed that the passband amplitude is nearly zero at W (2 MHz for the BLKO system) and that doppler shifting is negligible ($\Delta f_d/W \lesssim 0.01$ for the BLKO system). For a rectangular bandpass this ratio is 1.0.

With the fringes in the frequency domain, the uncertain bandpass amplitude appears as a multiplicative factor. The fact that this form (Eq. 49) decouples phase from amplitude can be demonstrated heuristically by computing phase at each frequency by means of the inverse tangent of the ratio of real and imaginary parts. (This method is not actually used for phase computation, as seen in Section X.) In such a computation, the amplitude would cancel in the ratio. As mentioned above, another advantage of the frequency domain is that phase corrections can be directly and simply applied to the fringes by means of a phase counter-rotation to each frequency component $h(\omega_k')$. That technique is used in the phase calibration procedure discussed in the next section.

SECTION VIII

STOPPED TONE PHASE

This section digresses to treat the subject of phase calibration by means of the tone generator and derives an expression for stopped tone phase. Appendix F derives expressions for tone amplitude and tone SNR.

In VLBI measurements, the observed phase is corrupted by unknown and unstable shifts due to instrumentation. Such phase effects can degrade the accuracy of geophysical measurements and complicate measurements of clock synchronization. However, most of these instrumental effects can be removed through the use of a phase calibrator. The commonly used approach, pioneered by A. E. E. Rogers (Ref. 3), is to inject at a point near the front of the instrumentation a calibration signal consisting of a set of tones, equally spaced in frequency and derived from the station frequency standard. Properly used, this technique can both correct for system phase instabilities and allow absolute calibration of interferometer phase so that clock synchronization is possible.

The calibrator signal is injected at a low power level and is imbedded in the radio source data. The phases of the injected tones for the current tone generator are expected to be stable at the 10-psec level and can be calibrated absolutely to the nanosecond level. Each channel bandpass will contain more than one tone, but the exact number in a given application will depend on system characteristics and specific accuracy goals. At the correlator, each tone is counter-rotated to nearly zero frequency by digitally mixing each single-station bitstream with a frequency that closely approximates the baseband frequency for that tone. After the resulting tone phase has been extracted and differenced between stations, it is subtracted from interferometer (fringe) phase. Since the tones are subjected to the same instrumental effects as the natural source signal, instrumental effects after the injection point cancel in the final difference. (This report will not consider difficulties encountered in calibration of instrumental effects before the injection point.) After instrumental calibration, the measured delay is reduced to the sum of a geometric delay and a clock synchronization offset, as we shall see in the following sections. (For simplicity, propagation media terms are ignored until Section XIII.)

In this section, tone phase is separated into the various effects that enter the calibrator signal in transit from the clock through the instrumentation and then through data reduction. Since the analysis will be based on an "ideal" model for the system, extra effort might be required to account for deviations from ideal behavior. It is beyond the scope of this report to assess all complications.

The model for stopped tone phase is developed in the following sequence: (a) from the ϕ-cal clock to the injection point, (b) from the injection point to the recorder and (c) through the data reduction procedure. The simplified block diagram of the instrumentation shown in Fig. 1 will be useful in tracing the signal through the instrumentation.

First, for step (a), the phase of the signal at the clock reference point (ϕ-cal clock) discussed in Section III and illustrated in Figure 1 is given in terms of true time and nominal frequency by

$$\phi_c = \omega_c (t + \tau_c) \tag{54}$$

as indicated by Eqs. (3) and (5). We have chosen to represent calibration phase in this way since (a) the clock error τ_c is explicitly shown, (b) true time t is common to both stations, and (c) tone frequencies are calculated at the correlator on the basis of the nominal frequency ω_c. The signal will experience a cable delay τ_u so that its phase entering the tone generator will be given by

$$\phi_c = \omega_c (t + \tau_c - \tau_u) \tag{55}$$

The "ideal" tone generator detects the zero crossings of the 5-MHz input signal and converts the positive-going zero crossing into rectangular pulses as indicated schematically in Fig. 2. The nominal width (τ_p) of the output pulses for the current tone generator is about 20 psec. Repetition rates slower than 5 MHz are obtained by blanking pulses. For example, by passing every 10th pulse, the pulse repetition rate would be 500 kHz. The passed repetition rate will be denoted by ω_p. As indicated below, the tone frequencies are the harmonics of the fundamental repetition rate ω_p.

In practice, there will be deviations from the ideal waveforms shown in Fig. 2, deviations such as delays, phase shifts and an amplitude distortion arising in both the tone generator and connecting elements. For example, a zero crossing is not precisely at the center of a rectangular pulse and the pulse shapes are not perfect rectangles. This report will not consider such deviations but most of these effects can be formally included by making a complex Fourier expansion rather than the cosine expansion presented below. (It should be pointed out that a constant deviation from rectangularity will cause clock synchronization measurements to be biased by a constant error that is less than the pulse width but will cause no error in geophysical/astrometric measurements.)

The output of the tone generator can be decomposed into its harmonics, which will have frequencies given by $n\omega_p$ (see Appendix F). The phase of the n^{th} calibration harmonic (tone) at the injection point will be given by

$$\phi_n = \omega_n (t + \tau_c - \tau_u) \tag{56}$$

The small group delays from the input of the tone generator to the injection point have not been explicitly represented since they (or any other group-delay between ϕ-cal clock and injection point) can be included in τ_u.

We are now prepared to model effects on tone phase introduced in transit from the injection point to the recorder and then through the tone-stopping process. After injection, the tones, along with the natural source signal, pass through various filters and mixers until they reach baseband within a 2-MHz bandwidth. As in the case of the natural source signal (Eq. 11), the effects of these instrumental stages can be represented by lumped variables so

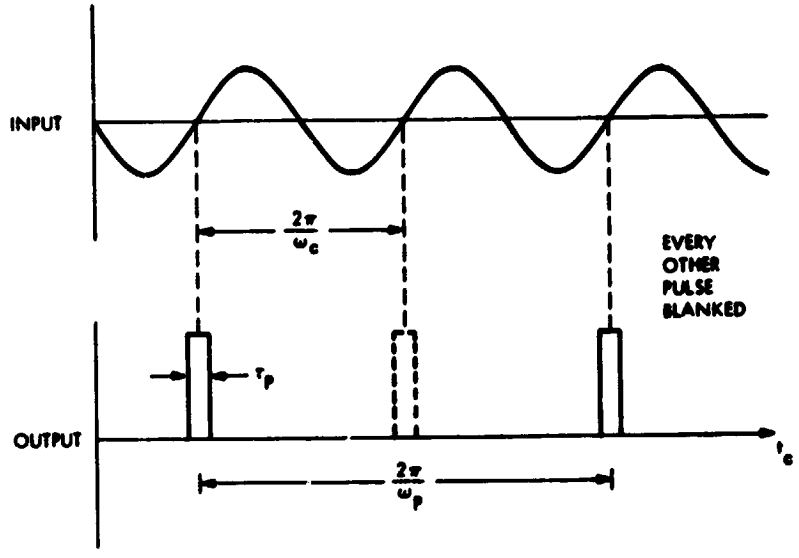

Fig. 2. Input and output signals for ideal tone generator

that the phase of the n^{th} tone recorded at bit time t_{bj} for station j becomes

$$\phi_n(t_{bj}) = \omega_n (t_j + \tau_{cj} - \tau_{uj}) - \psi_{Instr.} \tag{57}$$

where the instrumental phase effects are given by

$$\psi_{Instr.} = \omega_{hj} t_j + \phi_{hj} + \omega_n \tau_{Ij} + \phi_{Ij}(\omega_n) \tag{58}$$

Note that the delay τ_{aj} does not appear since the phase-calibration signal is not subjected to antenna delays. Again, t_j is the true time that corresponds to bit time t_{bj} at station j.

The recorded tones are processed at the same time the tapes are cross-correlated. The correlator operator will use a best estimate for the baseband frequency of each calibrator tone to separately "fringe-stop" each tone in a bit-stream (see Appendix F). That is, in effect, the correlator will subtract from the phase of the n^{th} tone the phase

$$\psi_{nj} = (\omega_n - \omega'_{hj}) (t_{bj} - t_s) \tag{59}$$

$$= (\omega_n - \omega'_{hj}) (t_j + \tau_{bj} - t_s) \tag{60}$$

where ω'_{hj} is the best (nominal) estimate for the heterodyne frequency, t_{bj} is bit time at station j, and t_s is the reference time adopted by the correlator. For phase calibration to work properly, it is necessary to use the same values for ω'_{hi}, and ω'_{hj}, and t_s in both the tone model phase (Eq. 59) and the cross-correlation model phase (Eq. 28). Based on Eqs. (57), (58) and (60), the theoretical expression for the resulting stopped-tone phase at station j becomes

$$\Delta\phi_j(\omega_n) = \phi_{nj} - \psi_{nj} \tag{61}$$

which is equal to

$$\boxed{\Delta\phi_j(\omega_n) = -\omega_n(\tau_{bj} - \tau_{cj} + \tau_{uj} + \tau_{Ij} - t_s) - \phi_{Ij}(\omega_n) - \Delta\phi_{hj}} \tag{62}$$

where the "stopped" heretodyne phase is given by

$$\Delta\phi_{hj} = \omega_{hj} t_j + \phi_{hj} - \omega'_{hj}(t_{bj} - t_s) \tag{63}$$

This puts the stopped-tone phase in the form we want, expressed in terms of contributing effects due to instrumentation and data reduction.

This analysis has neglected some subtle but important problems that can seriously degrade the stopped tone phase. These problems arise from unwanted intermodulation of frequency components in the calibrated signal with frequency components in the stopping function, where the resultant, possibly aliased frequency of the intermodulation product happens to be close to the frequency of the stopped tone. With careful design, these problems can be substantially avoided.

Several methods exist for extracting tone phase from the stopped tones. The method used in the present version of the BLKO system is discussed in Appendix G. In the following section, we will assume tone phase has been successfully extracted.

Another fact ignored to this point is that measured tone phase, like interferometer phase, has integer-cycle ambiguities. Ambiguity resolution for tones falls into two categories — relative and absolute. By relative ambiguity resolution, we mean the removal of ambiguities in a relative sense between tones within a channel passband. If such ambiguities are present, the variation of phase with frequency within a passband cannot be determined and correct interpolations in frequency cannot be made. For example, if one wishes to obtain an absolute estimate of bitstream-alignment (BSA) delay after phase calibration, one must either explicitly or implicitly determine the correct effective phase-frequency slope for the tones in the passband. To remove relative ambiguities, one must have an a priori estimate of the slope of phase vs. frequency, which means one must have estimates for terms multiplying ω_n in Eq. (62). Those terms are the correlator reference time t_s, the calibrator cable delay* (τ_u), the instrumental delay from the tone injection point to the recorder (τ_I), and the epoch offset ($\tau_b - \tau_c$) between the recorder clock and the ϕ-cal clock. The maximum allowed a priori error on these terms depends on tone spacing. For example, if the closest tones are separated by 500 kHz, then the collective a priori error (3 σ) on these terms must be less than one microsecond. Ambiguities on the other, more widely spaced tones can be removed by an iterative procedure akin to the bandwidth synthesis method. An example of relative ambiguity removal is given in Appendix G.

After relative ambiguities have been removed, there will remain in tone phase an overall (absolute) ambiguity which is the same for all frequency points in the passband. Thus, the overall calibrated interferometer phase obtained from each passband will not be corrected for absolute integer cycles due to instrumentation. As we shall see, it is not necessary to consider absolute instrumental ambiguities. Accurate measurement and application of only the fractional part of overall tone phase is sufficient for the ultimate removal of absolute ambiguities in corrected BWS delays and corrected interferometer phase, provided the BWS channels are properly spaced.

*More exactly stated, τ_u includes all delays from the clock reference point to the tone injection point.

SECTION IX

PHASE CALIBRATION

The next step in data reduction is to correct the fringe phase from each BWS channel with the phase derived from the tones injected by the phase calibrator. We will assume that there are several tones spaced across each passband and that integer-cycle ambiguities in tone phase can be removed in a relative sense between tones (see Appendix G) so that calibration phase at any frequency in a passband (i.e., at the frequencies ω_k in Section VII) can be obtained through interpolation. We will neglect errors in this process such as interpolation errors that might occur as a result of phase ripple across a passband.

The calibration phase at frequency ω_k within a passband is given by the difference in tone phase obtained for the two stations:

$$\phi_t(\omega_k) = \Delta\phi_i(\omega_k) - \Delta\phi_j(\omega_k) \tag{64}$$

Based on Eq. (62), this phase is theoretically equal to

$$\phi_t(\omega_k) = \omega_k(\tau_b - \tau_c + \tau_u + \tau_I) + \phi_I + \Delta\phi_h \tag{65}$$

where τ_b, τ_c, τ_u, τ_I, ϕ_I and $\Delta\phi_h$ are differences between stations in the order j minus i. For simplicity we have assumed that all dispersive phase shifts in ϕ_{Ij} in Eq. (61) occur after the tone injection point so that they appear identically in tone and fringe phase. If significant dispersive phase shifts occur before the injection point, separate calibrations will have to be applied.

For each frequency component $h(\omega_k')$ in the transformed fringes (Eq. 49), we will assume tone phase is subtracted from fringe phase by means of a counter-rotation (multiplying by $e^{-i\phi t}$) of the fringes at each fringe point (correlation interval). Other methods can be used to apply phase calibration at various stages in processing, but all of those approaches will not be discussed here. Fringe-point counter-rotation is chosen for the analysis in the text because it purifies the phase at an early point, making the fringes easy to interpret and use at an early stage. However, phase calibration in the BLKO system is currently applied to the final overall value obtained for each observable from an observation. That approach changes the order of the operations described here and leads to essentially the same final value for all observables. See Appendix G for a description of that procedure.

When the fringes in Eq. (49) have been counter-rotated with the tone phase in Eq. (65), one obtains

$$\langle h(\omega_k') \rangle = \frac{2a_1}{\pi} r_m \frac{S_p(\omega_k)\, G_i(y_{ik})\, G_j(y_{jk})}{G_A} F_q\, e^{i\Delta\phi_c} \tag{66}$$

where the corrected phase is given by

$$\Delta\psi_c = \omega_k (\tau_g' + \tau_c + \tau_a - \tau_u - \tau_m) + \phi_B(\omega_k) \qquad (67)$$

We have dropped the lag-shift term ($\omega_k' \ell_o \Delta$) in Eq. (49) since it is known and can also be counterrotated out of fringe phase along with tone phase. Removal of this term references the model delay to the central lag of the processor, thereby insuring that the residual phase from all BWS channels is based on the same model delay. As discussed in Section X, the current version of PHASOR does not correct for the lag-shift term until phase tracking of each BWS channel is completed. We have removed it here to simplify the analysis.

At this point, it is instructive to make a simple interpretation of interferometer phase given by Eq. (67). If separate measurements were made to determine the cable delay τ_u and antenna delay τ_a, these quantities could be removed from phase. The model delay τ_m is known exactly and could also be removed. (In practice, these quantities are actually removed at a later stage in processing, as discussed in Section XIII.) The interferometer phase would then be left in a clean and useful form: $\omega_k(\tau_g' + \tau_c)$. This is the phase that would result from measurements made at RF by ideal instrumentation (i.e., no cable delays, phase shifts, instabilities, etc.). Such ideal instrumentation can be visualized as a "point RF recorder" placed at the intersection of axes with no instrumental components to complicate the phase that is received and directly recorded at RF at each station. Under such ideal assumptions, one can easily derive the interferometer phase $\omega_k (\tau_g' + \tau_c)$ by means of a simple subtraction of the RF phases from the two stations after offsets to account for geometric delay and clock offset.

In the calibration process described above, a subtle point has been neglected. Only the fractional part (in cycles) of both interferometer phase and tone phase can be determined when phase is extracted after counterrotation. Thus, when tone phase is subtracted from interferometer phase, the subtraction actually denotes removal of the fractional part of instrumental phase. We can ignore integer-cycle errors at this point since we realize that there are integer-cycle ambiguities due to delay modeling that must be resolved later in the BWS process. The BWS process requires as input precise values for only the fractional part of interferometer phase, free of unwanted instrumental phase (fractional part). The integer-cycle part (due to τ_g' and τ_c) is then determined in a recursive process described in Appendix H. The output is a delay measurement free of postinjection instrumental effects. It is a peculiarity of this technique that, even though BWS delay and interferometer phase can be ultimately calibrated absolutely with regard to instrumental effects, instrumental phase, including integer cycles, is never absolutely measured.

SECTION X

PHASE TRACKING

At this stage, we are prepared to extract the observables of amplitude, phase, phase-delay rate, and BSA delay from the stopped fringes. More than one method is available for extracting observables from the fringes. The two most familiar approaches are phase-tracking and coherent integration across channels. The coherent integration approach (Ref. 4) is based on relatively simple, fast algorithms and has the important advantage of better SNR for signal detection. However, for this approach to work, the fringes must be made coherent across all summed channels by means of phase calibration. Since the phase-tracking approach does not require such coherence, we chose that approach in the early development of the BLKO system when phase calibration was not available. Further advantages of the phase-track approach include (a) versatility in modeling and weighting fringes, (b) easy access to intermediate observables for system trouble-shooting, (c) computation of RMS fringe residuals, and (d) simple adaptability to single-channel spacecraft applications with poorly known nonlinear phase.

In the phase-tracking technique, the fringes are analyzed (by a program called PHASOR) to extract all of their information content, including phase as a function of time during an observation. To obtain the time dependence, each observation is divided into equal sections, whose length falls in the range of a few seconds to a few minutes. As discussed below, the transformed fringes are fit within each section with a parametrized function to determine four quantities: amplitude, bit-stream-alignment (BSA) delay, phase-delay rate, and phase. The connection of phase between sections is discussed below. Phase tracking results in a further compression of the data in that each observation will be characterized by four parameters for each of 1-30 sections instead of 200-1000 complex fringe values.

As suggested by Eq. (67) and demonstrated below, a suitable mathematical model for the fringes within a section is given by

$$T(\omega_k, t_G) = A_s \, g(\omega_k') F_q \, e^{i\psi_s} \tag{68}$$

where the model phase is given by

$$\psi_s = (\omega_k - \omega_s) \, \tau_s + \omega_k \, \dot{\tau}_{\phi s} \, (t_G - t_z) + \phi_s \tag{69}$$

and

$$\omega_k = \pm |\omega_k'| + \omega_{hi} \tag{70}$$

The parameters A_s, τ_s, $\dot{\tau}_{\phi s}$ and ϕ_s are the four solve-for parameters mentioned above. The complex filter F_q accounts for the delay quantization and is derived in Appendix D. The reference frequency ω_z and reference time t_z will be placed at the center of the bandpass and center of the fitting interval, respectively, in order to minimize correlations and errors for phase, delay and delay rate. With this selection, the solve-for phase ϕ_s will be the phase at frequency ω_z

and time t_z. As implied by the fitting equation, it is assumed that the fringe phase can be adequately modeled as a linear function of time and as a linear function of frequency over the fitting interval. For some applications, the amplitude function $g(\omega_k')$, which becomes a real four-point array called BAMPL in PHASOR, can be calculated with adequate accuracy from the equation

$$g(\omega_k') \approx \frac{2}{\pi} a_1 \frac{G^2(\omega_k')}{\overline{G^2}} \tag{71}$$

where G is the measured bandpass amplitude (assumed to be the same for both stations as in Eq. 53). For a rectangular bandpass, we obtain $g(\omega_k') = 2a_1/\pi$. For more accurate amplitude measurements, a more complicated relation than Eq. (71) can be used as discussed in Appendix E.

Since the model is not linear in all parameters, a priori estimates of the four solve-for parameters must be obtained before a least-squares fit can be performed. Three of the parameters (A_s, τ_s, $\dot{\tau}_{\phi s}$) are obtained from the FFT's over time (one for each lag) that were used to detect the central lag (see Section VII). FFT integration times can range, in theory, from a few seconds to an observation length, depending on the application. The output of the FFT's over time can be viewed as a function of lag and fringe frequency (ideally with a sin x/x dependence in both directions) that peaks for unique values of those quantities. The determination of the location of this peak in lag-frequency space gives a direct estimate of the BSA delay (τ_s) and residual fringe frequency (and thus delay rate, $\dot{\tau}_{\phi s}$). The peak amplitude gives an estimate of fringe amplitude A_s.

Once A_s, τ_s and $\dot{\tau}_{\phi s}$ have been estimated, one can make an initial estimate of ϕ_s by means of a least-squares search (with the frequency-domain fringes) that minimizes the differences in the actual fringes and the model fringes as a function of ϕ_s. In this process, the model fringes are computed from Eq. (68) using as fixed values the estimates of A_s, τ_s and $\dot{\tau}_{\phi s}$ explained above. In the search, ϕ_s is incremented in small steps ($\sim$0.1 cycle) from 0 to 1 cycle. (This procedure will reveal only the fractional part of phase. Procedures for dealing with the integer part will be discussed below.) For each phase increment, the square of the difference between the actual and model fringes is summed over time points in the given section. The resulting values for the ($\sim$10) sums are then searched for the minimum that reveals which phase value was the best estimate. (In practice, an interpolation between steps is carried out to obtain a more accurate estimate.)

After all four a priori estimates have been determined, the fringes are subjected to a standard least-squares fit that simultaneously estimates all four parameters for the section. Theoretical expressions for the resulting parameter estimates can be formally demonstrated as follows. Comparison of Eq. (66) and Eq. (68) indicates that the solve-for amplitude will be given by

$$\boxed{A_s \approx r_m \doteq v_f \sqrt{\frac{T_{qi}\, T_{qj}}{T_{si}\, T_{sj}}}} \tag{72}$$

Further, the solution will require the phases to be equal so that we will have from Eqs. (67) and (69)

$$(\omega_k - \omega_z)\,\tau_s + \omega_k\,\dot{\tau}_{\phi s}\,(t_G - t_z) + \phi_s = \omega_k\,(\tau'_g + \tau_c + \tau_a - \tau_u - \tau_m) + \phi_B(\omega_k) + 2n\pi \tag{73}$$

where $2n\pi$ represents the integer-cycle ambiguity mentioned above. Expanding the right-hand side of this equation in terms of frequency and time about ω_z and t_z and equating like terms on each side, one finds that the solve-for parameters will be given by

$$\tau_s = \Delta\tau_f + \frac{\partial\phi_B}{\partial\omega} \tag{74}$$

$$\dot{\tau}_s = \Delta\dot{\tau}_f + \frac{\dot{\phi}_B}{\omega_z} \tag{75}$$

$$\phi_s = \omega_z\,\Delta\tau_f + \phi_B(\omega_z) + 2n\pi \tag{76}$$

where

$$\Delta\tau_f \equiv \tau'_g + \tau_c + \tau_a - \tau_u - \tau_m \tag{77}$$

All of these terms are evaluated at time t_z and frequency ω_z. The delay τ_m is the model delay at the central lag of the correlator, as indicated in Section VI.

Thus, all three of these solve-for parameters depend on $\Delta\tau_f$. Note that (ignoring the $2n\pi$ ambiguity and structure effects in ϕ_B) $\tau_g = \phi_s/\omega_z = \Delta\tau_f$, while delay rate is approximately equal to the time derivative of that quantity. This relationship between τ_s and ϕ_s is a fundamental requirement for single-observation bandwidth synthesis (BWS), a process that is used to account for effects of integer-cycle ambiguities in ϕ_s. The removal of ambiguities between frequency channels by single-observation BWS is discussed in Appendix H. For each BWS channel, ambiguities are removed between sections within an observation by means of another procedure to be discussed below.

Examples of fringes in the frequency domain are given for an intercontinental baseline in Fig. 3 and for a short baseline in Fig. 4. The fringes in Fig. 3 are the frequency-domain counterparts of the lag-domain fringes presented in Appendix C. The solve-for values of amplitude, frequency, phase and BSA delay are given at the top of the figure, where the errors are the covariance errors based on RMS fringe residuals computed for the fit interval. (Note that amplitude has been multiplied by 10^5 for convenience.) Except for amplitude, the solve-for values in Fig. 3 are in agreement with the values for the same parameters estimated in the lag domain in Appendix C. Amplitude is different since different normalizations are applied in the two domains. That is, the solve-for amplitude

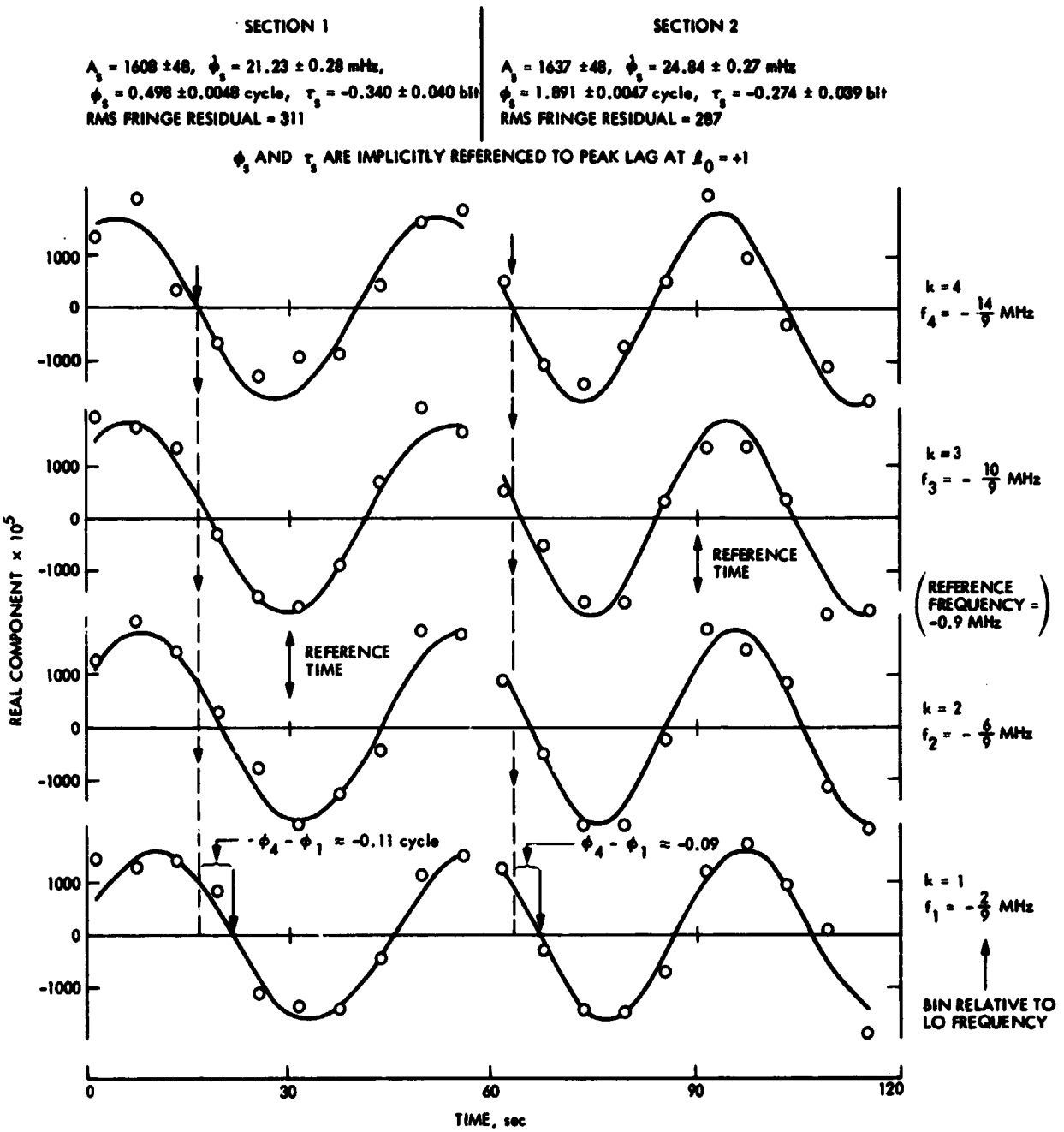

Fig. 3. Long-baseline example of stopped fringes for the BLKO system

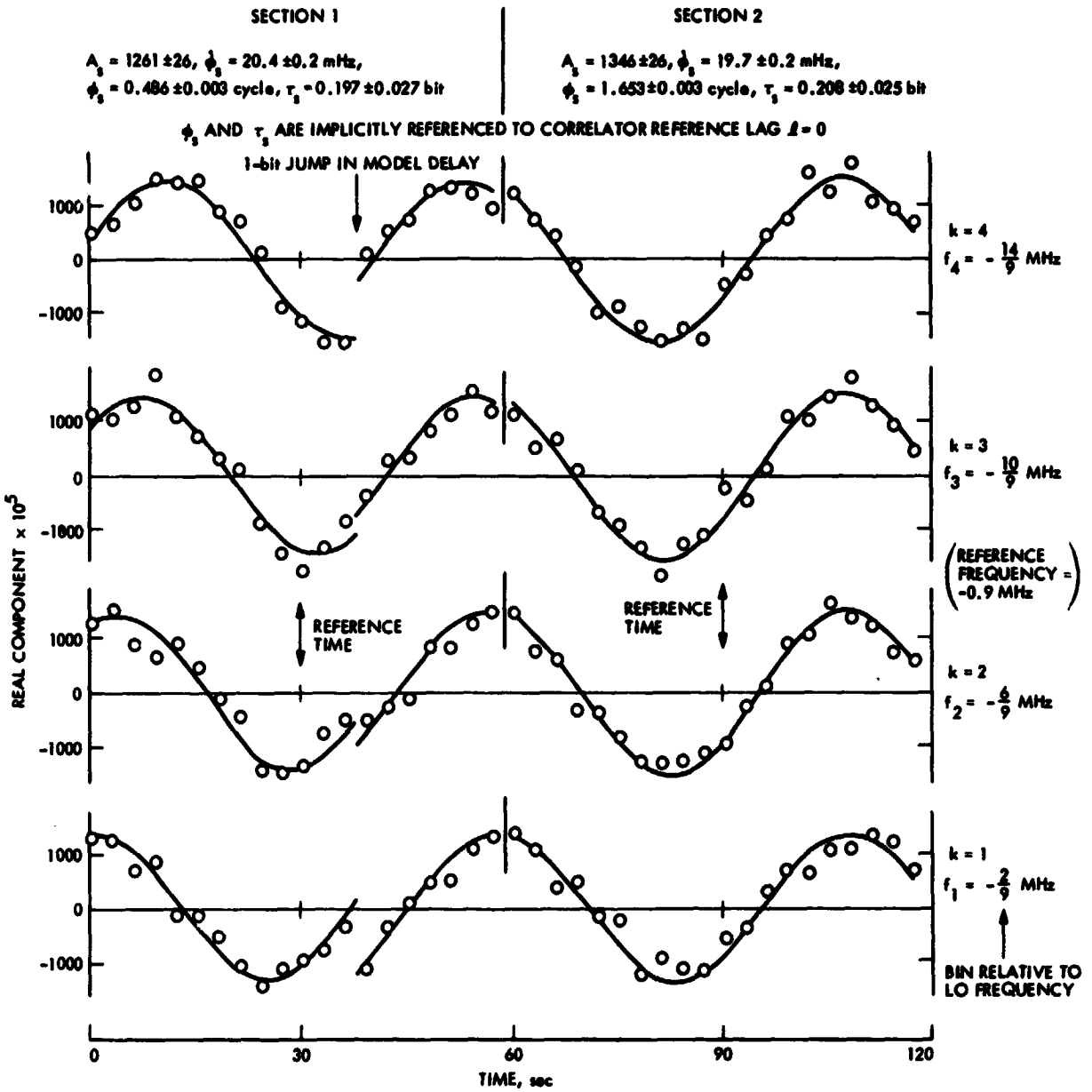

Fig. 4. Short-baseline example of stopped fringes for the BLKO system

in the lag domain is equal to the amplitude of the fringes in Eq. (37) while, in the frequency domain, it is given to first approximation by Eq. (72). The current ratio for these normalizations is about 2.0. For these particular fits, the amplitude normalization matrix, BAMPL, has been assigned the values (1.02, 1.14, 1.14, 1.14) for the four frequency bins. These values appear to match the data fairly well and are not very different from the theoretical BAMPL values calculated in Appendix E on the basis of nominal bandpass shape. However, the differences between the two BAMPL arrays illustrate the level of difficulty in obtaining one bandpass shape that is suitable for all data. (For very accurate amplitude measurements, it may be necessary to use a strong source of known strength to generate calibration fringes from which both the relative magnitudes of the BAMPL components and the overall BAMPL normalization can be determined for each channel.)

By inspecting the plot, one can readily see that the solve-for values are in accord with values easily estimated by inspection. The frequency can be estimated from the period of the fringes. The phase is referenced in time to the center of the interval (arrow) and in frequency to a nominal centroid frequency (0.9 MHz). A value for phase can be estimated by interpolating to the reference frequency at the reference time. BSA delay can be roughly estimated by extracting the shift in phase (see dotted arrows in Fig. 3) between the two outer frequency bins in the plot and dividing this shift by the frequency difference ($2W/3 = 4/3$ MHz) between the bins.

The short baseline fringes in Fig. 4 are provided to illustrate the discontinuity in the fringes introduced by a particular 1-bit jump in delay, as modeled through F_q (see Appendix D) in Eq. (68). As mentioned earlier, such discontinuities are also present for intercontinental baselines but occur so frequently that a number of jumps are averaged over in a single fringe point.

Up to this point, we have considered parameter estimation for only one section in an observation. In most cases, an observation is divided into several sections of equal length (5 - 120 seconds), each of which is separately fit for A_s, τ_s, $\dot{\tau}_{\phi s}$, and ϕ_s. An observation can be divided into sections so that there is less chance for the time dependence of the solve-for parameters (particularly nonlinear phase rate) to violate the assumptions underlying the fringe model and so that the time dependence can be observed. However, the section must be long enough to provide enough "SNR" for a successful fit.

Since fringe fits yield only the fractional part of fringe phase, additional effort is required to properly connect phase between sections. The phase for the first section is forced to fall in the range 0-1 cycle. (It is this arbitrary assignment that gives rise to the absolute ambiguity in overall phase from the observation.) A preliminary estimate of the phase of the second section is made by adding to the least-squares phase of the first section the phase change predicted by multiplying the estimated fringe frequency (from the FFT or from fringe fitting) by the time interval between section centers. This preliminary estimate is then compared with the more precise but ambiguous phase produced by the fit to the second section. The two are forced into agreement by incrementing or decrementing the fit phase by integer cycles. Clearly, the phase extrapolation to the second section must be in error by no more than ±0.5 cycle for this procedure to work. Once the ambiguity in the second section has been

removed, its phase and the fringe frequency are used in the same fashion to resolve the relative ambiguity in the third section, and so on, until the last section is completed.

Figure 5 displays the phase values (lower curve) associated with the fringes in Fig. 3. However, to obtain those phase values, the fringes in Fig. 3 were rerun through PHASOR with the section length reduced from 60 seconds to 12 seconds. This shorter section length was chosen to better reveal the time behavior of phase. As explained in the figure, a phase correction equal to $(\omega_k - \omega_{hi})\ \ell_o b$ has been applied in order to shift the measured phase, $\phi_s(\omega_z)$, from the peak lag (ℓ_o) to the reference lag of the correlator (ℓ=0). (See Eqs. 49 and 66 and the comments after Eq. 67.) Note that the phase rates of the two plotted channels are about the same, as one would expect, and that the nonlinear phase excursions of the two channels are highly correlated, as one would expect for many error sources (e.g., ionospheric fluctuations and station oscillator instability).

In summary, the output from this stage in processing consists of values for amplitude, BSA delay, phase-delay rate and phase, computed for each frequency channel as a function of time (section) across an observation. A formal error for each parameter value is computed by means of a standard covariance analysis based on the RMS residuals found in the fringe fits.

SECTION XI

DELAY MODEL IMPROVEMENT

Although it is adequate for cross-correlation, the delay model used by the correlator is fairly crude and is inadequate for subsequent processing. After phase tracking, PHASOR replaces the inaccurate correlator delay model with a more accurate model by appropriately adding back to the three solve-for parameters given theoretically by Eqs. (74-76) the correlator model τ_m (which is numerically passed) and then subtracting a new more accurate model. As indicated by Eq. (26), the geometric component of the new model should accurately reproduce the "geometric" delay that has been set up in fringe phase by time-offsetting in the correlator. The new more accurate model delay is given by

$$\tau'_{mg} = \frac{\hat{k}_m \cdot [\vec{x}_{mj}(t_j - \tau_{mj}) - \vec{x}_{mi}(t_i - \tau_{mi} - \ell_o b]}{c} \tag{78}$$

where we have used the central lag (ℓ_o) for the lag offset ℓ under the assumption that such an approximation is sufficiently accurate or that lag-dependent corrections have been made (see Section V). The station positions $\vec{x}_{mk}(t)$ are highly accurate models for the motions of the stations, while $\hat{k}_m$ is an accurate model for the source direction. In the most demanding applications, one must make a distinction between the bit time (t_{bj}) and true time (t_j) when calculating the above delay, since the geometric delay will be parametrized in terms of true time. This can be accomplished by inputting a clock error (τ_{bj}) for each station and using it to compute true time from bit time (see Eq. 1). The resulting values of true time are then used in model calculations as suggested in Eq. (78). The confusing presence of a different true time for each station is a consequence of correlator design, as discussed in Section V.

Model replacement is carried out for each of the three aforementioned solve-for parameters from each section in an observation. For each section, the time arguments in the model delay are determined from the section reference time (i.e., $t_{bj} = t_{bi} = t_z$ = section reference time so that $t_i = t_z - \tau_{bi}$ and $t_j = t_z - \tau_{bj}$).

In addition to the geometric delay, one can also replace at this step the model for troposphere, the clock or other delay components if desired.

In subsequent sections, we will still refer to Eqs. (74-76) as the theoretical forms for the observables, but with the understanding that the model delay has been replaced with an improved value. The resulting change in the observables can be accounted for by changing Eq. (77) to the form

$$(\Delta\tau_f)_{new} = (\Delta\tau_f)_{old} + \tau_m - \tau'_m \tag{79}$$

$$= \tau'_g + \tau_c + \tau_a - \tau_u - \tau'_m \tag{80}$$

where τ_m' is the new model delay. BSA delay, BWS delay, and phase delay (except for cycle ambiguities and structure effects) are now all theoretically equal to this expression for delay but are known at different levels of precision.

Even though model improvement is always applied in actual data reduction, we will suppress it in our example observation so that data flow can be continuously traced from figure to figure.

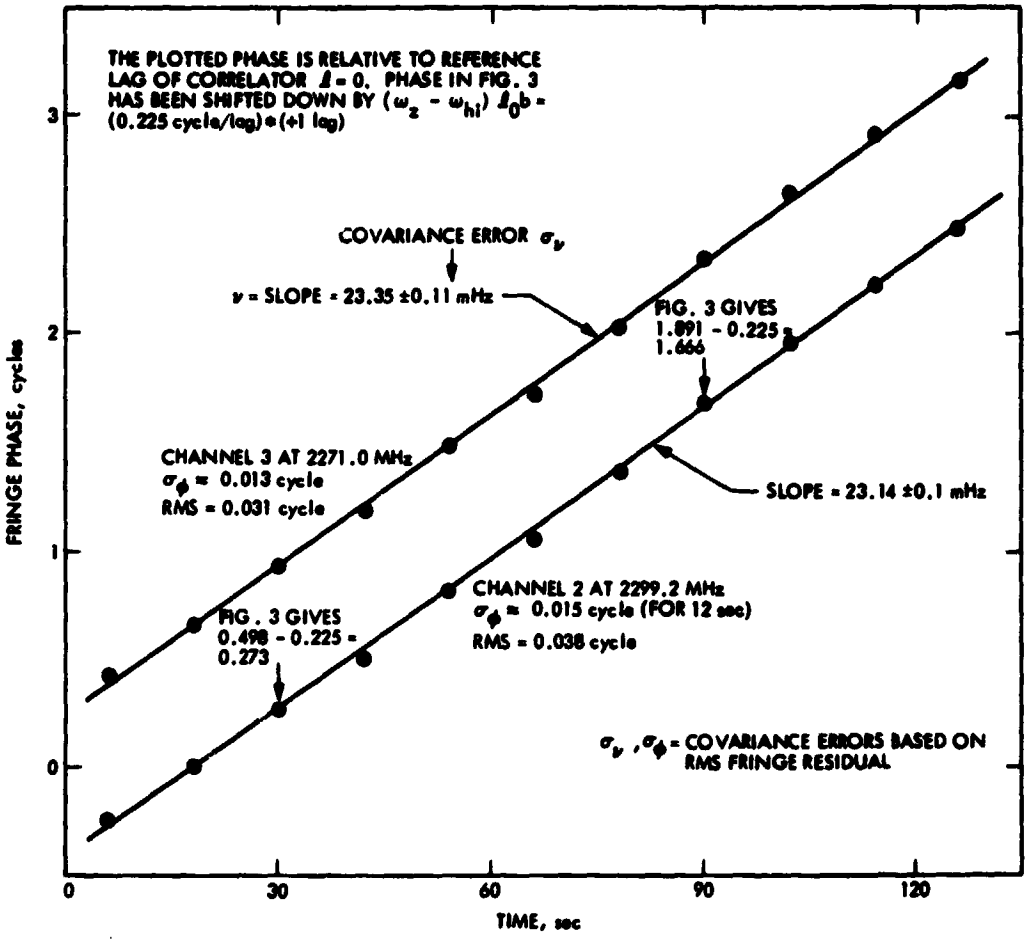

Fig. 5. Example of stopped fringe phase

SECTION XII

OBSERVABLE FORMATION

After the four solve-for quantities (amplitude, BSA delay, phase-delay rate, phase) have been extracted from the fringes for each section across an observation, they must be analyzed to obtain the final observables. As mentioned above, the behavior of the parameters as a function of section (time) is often informative when there are equipment problems, ionosphere signatures, and the like. However, to reduce final data volume, it is usually desirable to pass on to subsequent software one composite value per observation for each parameter. Composite values for amplitude and BSA delay are obtained in PHASOR by averaging the values for all sections in an observation. On the other hand, all of the delay rate values from individual sections are discarded since a better estimate of delay rate can be derived from the section phases as follows.

As illustrated in Fig. 5, the phase values at the section centers of a BWS channel are fit by least-squares with a linear function of time to generate a composite phase-delay rate (slope) and a composite phase (constant). The composite phase from this fit becomes the final estimate for the RF phase for that channel. In order to minimize correlations, the reference time for the composite phase is defined in the fit to be the center of the observation. After the fit, phase residuals are computed to reveal nonlinear trends. In addition, a covariance analysis based on the formal errors (obtained from fringe fitting) in section phase is performed to obtain the formal errors in the composite phase and phase-delay rate.

As mentioned above, the usefulness of the phase observable is greatly reduced by an absolute ambiguity that currently remains unresolved in the BLKO system. On the other hand, the composite phase-delay rate from the fit is absolutely known (except for occasional and resolvable aliasing) and becomes the composite observable for the given channel. For the final observables of phase-delay rate and BSA delay, one has the option of either using the composite value from one channel or averaging over all channels.

The calculation of the composite BWS delay observable is somewhat more complicated. First, BWS delays are computed for each section of a channel pair by combining the section phases according to the formula

$$\Delta\tau_{BWS} = \frac{\phi_a - \phi_b}{\omega_a - \omega_b} \tag{81a}$$

where the phases (ϕ_a, ϕ_b) and frequencies (ω_a, ω_b) come from channels (a, b). From Eq. 76, one finds the theoretical value for BWS delay is given by

$$\Delta\tau_{BWS} \approx \Delta\tau_f + \frac{\partial\phi_B}{\partial\omega} + \frac{2n'\pi}{\omega_a - \omega_b} \tag{81b}$$

where the partial of structure phase approximates the associated finite difference (assuming that $\Delta\omega/\omega \ll 1$) and where the last term represents the integer-cycle

ambiguity. To reveal time dependence across an observation, a separate BWS delay value is computed for each section in an observation, as illustrated in Fig. 6 for the phase values in Fig. 5. Integer-cycle ambiguities are then removed in a relative sense by comparing delays from adjacent sections. (Residual delay typically changes very slowly across an observation.) The section delays from each channel pair are then fit by least-squares with a linear function of time (section) to determine a composite BWS delay rate (slope) and a composite BWS delay (constant) for that pair. In the fit, the reference time is defined to be the middle of the observation. The BWS delay rates for the separate channel pairs should be equal, within errors, to one another and (ignoring the effects of space charge) to the phase-delay rates obtained above for the separate channels. Since the BWS delay rates are less precise, they serve mainly as a consistency check. (In cases with very poor a priori delay models, BWS delay rates can be used to remove aliasing in phase-delay rates.) It should be pointed out that the rates for the particular case in Figs. 5 and 6 should differ by about 15 mHz due to an artificial frequency-independent offset inserted in model phase during fringe stopping. If that offset, which was included for fringe plotting purposes, is removed from the rate in Fig. 5, the rates from the two figures are in fair agreement.

Among the final composite values, we have an ambiguous BWS delay from each channel pair and an unambiguous BSA delay. It is clear from Eqs. (74) and (81b) that all of these delays are given theoretically by Eq. (77) plus the source structure partial, except for integer-cycle ambiguities in the BWS delays. That makes it possible to eliminate the BWS ambiguities by single-observation bandwidth synthesis, a bootstrap technique that begins with the unambiguous (but least precise) BSA delay and successively removes ambiguities in the (increasingly precise) BWS delays for ever-wider channel separations. The details of this procedure are given in Appendix H and are illustrated by completing the reduction of the long-baseline observation presented in preceding sections. When phase calibration is available, a slight improvement in precision can be obtained by using an alternate method to obtain BWS delay. In that method, the channel phase values, corrected for relative ambiguities, are fit with a linear function of observing frequency to obtain the BWS delay (slope). After extraction by either method, the BWS delay is given theoretically by Eq. (81b) without the ambiguity term.

In summary, the processing of a single observation produces one composite value for each of four observables: amplitude, phase-delay rate, BWS delay and RF phase. Ambiguities are absolutely removed in the BWS delay but are not currently removed in RF phase. Therefore, RF phase is not used in subsequent processing for geophysical information although it probably will be in the future. Presently, the composite BWS delay from the most widely spaced channel pair is generally taken as the final delay observable.

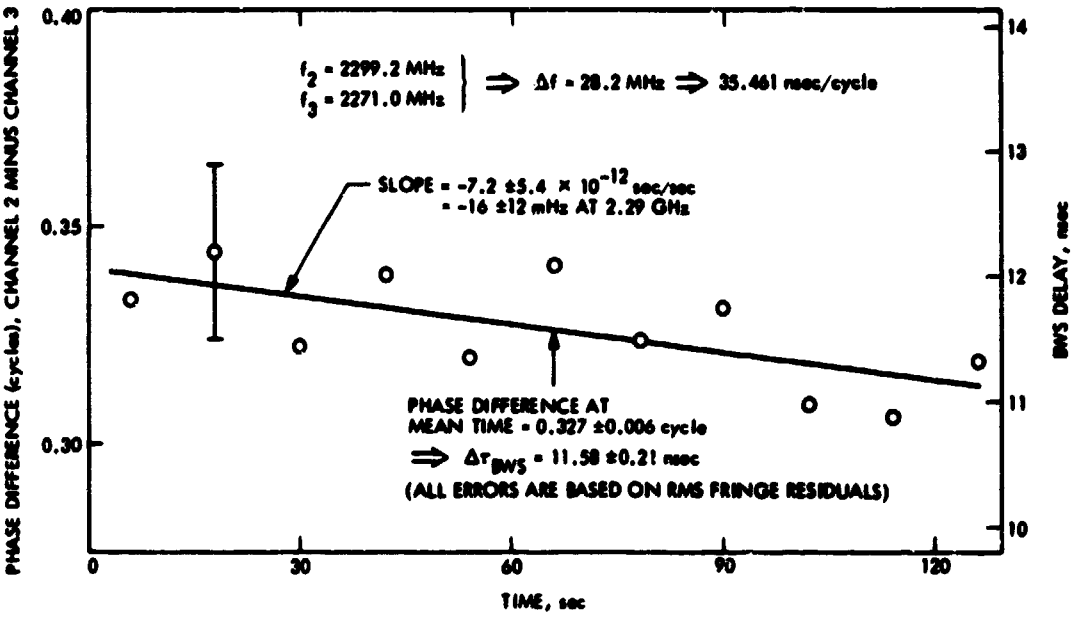

Fig. 6. Calculation of BWS delay from channel phase values in Fig. 5

SECTION XIII

CALIBRATION OF PROPAGATION MEDIA DELAYS

For simplicity, we have neglected in the preceding analysis the delays due to propagation media. In the case of the troposphere, the propagation delay enters simply as a group delay (i.e., adds another term to $\Delta\tau_f$ in Eq. 80). Consequently, once the troposphere has been calibrated, its effect can be removed from delay or delay rate by a simple subtraction. On the other hand, the treatment of delays due to charged particles is a little more complicated.

The effect of charged particles on fringe phase (in radians) can be represented by

$$\phi_e(\omega) = \frac{K_c N_e}{\omega} \tag{82}$$

where ω is the observing frequency (rad/sec), K_c is a constant, and N_e is the difference in the integrated electron content along the two raypaths of the interferometer. The group delay corresponding to this phase shift is given by the usual expression:

$$\tau_e(\omega) = \frac{\partial\phi_e}{\partial\omega} = -\frac{K_c N_e}{\omega^2} \tag{83}$$

It can readily be shown that, neglecting source structure effects, charge-particle effects will show up in the interferometer observables (Eqs. 74-76) in the form

$$\tau_s = \Delta\tau_f + \tau_e(\omega_z) \tag{84}$$

$$\dot{t}_s = \Delta\dot{t}_f + \dot{\phi}_e(\omega_z)/\omega_z \tag{85}$$

$$\phi_s/\omega_z = \Delta\tau_f + \phi_e(\omega_z)/\omega_z \qquad \text{(neglecting } 2n\pi\text{)} \tag{86}$$

where ω_z is the reference (centroid) frequency for the channel under consideration. In some experiments, the final BSA delay and delay rate are obtained by respectively averaging τ_s and $\dot{t}_{\phi s}$ over all channels in the band. In these cases, the frequency ω_z in Eqs. 84 and 85 should be changed to the effective frequency given by

$$\omega_{eff}^{-2} = \frac{1}{N_c}\sum_z \omega_z^{-2} \tag{87}$$

where N_c is the number of channels.

For the two-channel BWS delay (Eq. 78), the charged-particle delays enters in the form

$$\Delta\tau_{BWS} \approx \Delta\tau_f + \frac{\phi_e(\omega_a) - \phi_e(\omega_b)}{\omega_a - \omega_b} \tag{88}$$

$$\approx \Delta\tau_f - \frac{K_c N_e}{\omega_a \omega_b} \tag{89}$$

Thus the effective frequency for the charge-particle delay in two-channel $\Delta\tau_{BWS}$ is given by

$$\omega_{BWS} = \sqrt{\omega_a \omega_b} \tag{90}$$

We are now in a position to discuss S/X calibration of charged-particle effects. Suppose that we have measured the interferometer observables in Eqs. 84, 85, 86 and 89 at both S-band and X-band. Note that τ_s, $\dot{\tau}_{\phi s}$, ϕ_s/ω_z and τ_{BWS} are all equal to a group delay term plus a charged-particle term proportional to ω^{-2}. One can easily show that the ω^{-2} term for any one of these observable types can be removed by means of a linear combination of the S-band and X-band observables for that observable-type:

$$O_{sx} = c_s O_s + c_x O_x \tag{91}$$

where O_s and O_x are the observables at S- and X-band and

$$c_s = \omega_s^2/(\omega_s^2 - \omega_x^2) \tag{92}$$

$$c_x = \omega_x^2/(\omega_x^2 - \omega_s^2) \tag{93}$$

The effective frequencies ω_s and ω_x are computed for each observable type as discussed above. With this choice of the constants, the calibrated observable O_{sx} will be independent of charged-particle effects (i.e., only the first term in Eqs. 84, 85, 86 or 89 will remain).

The observables at S- and X-band can also be used to extract the electron content (or its rate). The constants used in the linear combination for this purpose are

$$c_s' = -c_x' = K_c^{-1}\, \omega_s^2\, \omega_x^2/(\omega_x^2 - \omega_s^2) \tag{94}$$

This second linear combination will give

$$0'_{sx} = -N_3 \quad \text{from 3SA delay } \tau_s \tag{95}$$

$$= \dot{N}_e \quad \text{from delay rate } \dot{\tau}_{\phi s} \tag{96}$$

$$= N_e \quad \text{from phase delay } \phi_s/\omega_z \text{ (neglecting } 2n\pi) \tag{97}$$

$$= -N_e \quad \text{from BWS delay} \tag{98}$$

We should note that, if residual observables are used in the S/X combination, as in the BLKO system, the model delay implicitly applied in $\Delta\tau_f$ must be the same for the S-band and X-band observables. In presenting the expression for the coefficients in Eqs. 92, 93, and 94, we have assumed combinations of one observable type: BWS delay with BWS delay, phase delay with phase delay or delay rate with delay rate. If BWS delay from one band is combined with phase delay from the other, then the coefficients will change somewhat. Those expressions can be easily derived and will not be presented here.

After S/X calibration, the residual observables are theoretically free of charged particle effects except for dispersive errors in measured delay. One "dispersive" effect in dual-band calibration, the source structure terms neglected in Eqs. 84-86, is discussed in Reference [5].

SECTION XIV

MODEL RESTORATION

For computational and interpretive convenience, residual delays (i.e., Eqs. 74, 75, 76 and 81b) rather than total delays have been utilized in the reduction up to this point. However, since the desired final observable is the total delay with the model delay restored, one must compute the model delay that must be added to the residual BWS delay. The geometric component of this model delay is chosen so that the geometric component of the resulting total delay is equal to the conventional geometric delay. The conventional geometric delay is defined as the difference in time of arrival of a wavefront at the intersection of axes of the two antennas, where one station is taken as reference. As derived in Appendix I, the model geometric delay resulting from this definition is given by

$$\tau_{mg}(t_i) \approx \frac{\hat{k}_m \cdot [\vec{x}_{mj}(t_i) - \vec{x}_{mi}(t_i)]}{c(1 + \hat{k}_m \cdot \dot{\vec{x}}_{mj}/c)} \tag{99}$$

where station i has been chosen as the reference station and where the denominator accounts for the motion of station j during wave transit (transit time correction). The source position $\hat{k}_m$ and station-position $\vec{x}_{mi}(t)$ in this expression must be exactly equal to those used in the model removed (Eq. 78). The time argument t_i, which becomes the time tag for the final observables, is set equal to true time at the middle of the observation. (Since residual delay and delay rate essentially remain the same over time intervals that typically separates true time from bit time, one has the freedom to make this choice for time tag).

It might seem strange that the restored model (Eq. 99) is not equal to the model removed (Eq. 78). The models differ in the offsets in the time arguments of the station positions (compare Eq. 78 with Eq. I2 in Appendix I). In the model removed, both stations must be given argument offsets in order to match the phase produced by the correlator when both bitstreams are offset by model delays. The modeled argument offsets for the two stations must be precisely equal to those correlator model delays. In the model restored, the conventional definition of geometric delay requires that only station j be offset in time where that offset is equal to the geometric delay (see Appendix I). The reason one has some freedom in selecting the restored model delay is that the delay effects due to such argument offsets are small ($\dot{\vec{x}}_{mj}\,\tau_g/c < 2 \times 10^{-6} * 20$ msec = 40 nsec). This means that they can be accurately modeled and, therefore, accurately removed or inserted. We can then choose to restore the model that makes the final total delay conform to the conventional definition of geometric delay.

The total model delay to be restored is equal to τ_{mg} plus all other terms in τ_m' except the geometric model τ_{mg}' (see Section XI) and is most easily expressed as

$$\tau_{mA} = \tau_{mg} + \tau_m' - \tau_{mg}' \tag{100}$$

After this model is added back and after measured values for the "cable delay" τ_u and the "antenna delay" τ_a are removed, the resulting delay observables from Equations 76 and 81b (with $\Delta\tau_f$ given by Equation 80) become

$$\tau_\phi = \tau + \frac{\phi_B}{\omega_z} + \frac{2n\pi}{\omega_z} \tag{101}$$

for phase delay and

$$\tau_{BWS} \approx \tau + \frac{\partial \phi_s}{\partial \omega_z} \tag{102}$$

for BWS delay (with ambiguity removed) where

$$\tau \equiv \tau_g + \tau_c \tag{103}$$

The total geometric delay, which entered the preceding equations in the form

$$\tau_g = \tau'_g - \tau'_{mg} + \tau_{mg} \tag{104}$$

now has the conventional definition given in Appendix I and is defined relative to a reference position $\hat{k}_a$. Thus, except for structure effects and an integer-cycle ambiguity, the BWS delay and phase delay are equal to the same delay: a geometric delay plus a clock synchronization term. When these observables are obtained through S/X calibration, the structure terms are evaluated at X-band. Strictly speaking, the structure effect is a geometric effect and can be absorbed in the geometric delay by placing the reference position at the effective position [5]. However, a single reference position cannot be used to make the structure effect disappear for both τ_ϕ and τ_{BWS} since the effective positions for the two observables usually are not the same.

For computational convenience, phase-delay rate, which as a measured residual has the form given in Equation 75 (but is obtained from residual phase slope), is passed to subsequent software not as an observed rate but as two delays whose difference will represent the delay rate. The measured residual phase-delay rate $\Delta\dot{\tau}_\phi$ is converted to two total delay values by the relations

$$\tau_{\phi R}(t + \delta t/2) = \tau_{mA}(t + \delta t/2) + \Delta\dot{\tau}_\phi \, \delta t/2 \tag{105}$$

$$\tau_{\phi R}(t - \delta t/2) = \tau_{mA}(t - \delta t/2) - \Delta\dot{\tau}_\phi \, \delta t/2 \tag{106}$$

where δt = 1 to 4 seconds. In subsequent processing, these delays are converted to a delay-rate-like observable by the relation

$$\frac{\delta\tau_{\phi R}}{\delta t} = \frac{\tau_{\phi R}(t + \delta t/2) - \tau_{\phi R}(t - \delta t/2)}{\delta t} \tag{107}$$

This reconstructured rate observable is essentially equal to

$$\dot{\tau}_\phi = \dot{\tau} + \frac{\dot{\phi}_B}{\omega_z} \tag{108}$$

which is the time derivative of the phase-delay observable.

With regard to structure effects, it can be shown [5], that, for each observation, one effective position can be found that, when used as the reference position $\hat{k}_a$, will set the structure terms in both BWS delay and phase-delay rate equal to zero. Thus, those observables can be represented by $\tau_g + \tau_c$ and $\dot{\tau}_g + \dot{\tau}_c$ where τ_g is the geometric delay relative to the effective position for those two observables.

SECTION XV

SUMMARY

For each of several baselines ($\leq$10), the BLKO system can cross-correlate and compress approximately a gigabit of recorded data for a natural source to four final observables. After phase-calibration and dual-band charged-particle calibration, the four final observables are fringe amplitude (Equation 72), phase-delay (Equation 101), phase-delay rate (Equation 107), and BWS delay (Equation 102). Multiple baseline observations of fringe amplitude, perhaps coupled with triangle-closure values for the other observables, can be used in subsequent analysis to study source structure. If the delay and delay-rate observables are measured for many sources, they can be subjected to a multi-parameter fit to obtain astrometric and geophysical parameters.

The Block II system now under development will be superior to the BLKO system in many ways. The improvements include (a) a lower fringe-detection threshold, as well as simpler and faster operation, through coherent integration across frequency channels (a BLK II option that requires phase-calibration), (b) more frequency channels (28), (c) a higher total bit rate through continuous recording of each frequency channel, (d) better phase calibration by using four tones per channel and by frequent "real-time" counter-rotation of fringe phase (at every correlation interval), (e) reduced intermodulation and aliasing in stopped tone phase by quantizing the tone-stopping sinusoids to 128 amplitude levels rather than 3, (f) improved capability for spectral-line work (224 lag integrations), (g) longer integration times for a given data-storage-array size by means of data compression through digital filtering, and (h) an improved fractional-bit-shift correction through frequent ($\sim$ every 10 msec) counter-rotation of fringe phase. The Block II system is scheduled for completion in 1982.

REFERENCES

1. Thomas, J. B., "An Analysis of Long Baseline Radio Interferometry," DSN Progress Report 32-1526, Vol. V, p. 45, 1971; Vol. VII p. 37, 1972; Vol. VIII, p. 29, 1972, Jet Propulsion Laboratory, Pasadena, Calif.

2. van Vleck, J. H., and Middleton, D., "The Spectrum of Clipped Noise," Proc. IEEE, Vol. 54, No. 1, 1966.

3. Rogers, A. E. E., "A Receiver Phase and Group Delay Calibrator for Use in Very Long Baseline Interferometry," Haystack Observatory Technical Note 1975-6.

4. Rogers, A. E. E., "Very-Long-Baseline Interferometry with Large Effective Bandwidth for Phase-Delay Measurements," Radio Science, 5, P. 1239, 1970.

5. Thomas, J. B., "An Analysis of Source Structure Effects in Radio Interferometry Measurements," Publication 80-84, Jet Propulsion Laboratory, Pasadena, Calif., 1980.

6. Purcell, G. H., "A Procedure for Preliminary Reduction of Bandwidth Synthesis Data," DSN Progress Report 42-33, P. 149, Jet Propulsion Laboratory, Pasadena, Calif., June 15, 1976.

APPENDIX A

A COMPLETE DERIVATION OF THE CROSS-CORRELATION FUNCTION

This appendix presents a complete derivation of the cross-correlation function, taking into account the statistics and the spatial distribution of the emissions of the natural source.

The radio noise generated by a very distant extended natural source can be expressed as a superposition of plane waves in the form

$$E(\vec{x},t) = \int_{\hat{k}} \int_0^\infty A(\hat{k},\omega)\ \exp[i\omega(t - \hat{k}\cdot\vec{x}/c)]\ d\omega\ d\Omega + c.c. \qquad (A1)$$

where $E(\vec{x},t)$ is the electric field at position $\vec{x}$ and true time t. For simplicity, the electric field is assumed to be linearly polarized. The function $A(\hat{k},\omega)$ is the Fourier amplitude at frequency ω for the wave received from direction $\hat{k}$, while c.c. denotes complex conjugate. As in Section IV, all quantities are measured with respect to a geocentric frame. The wave direction $\hat{k}$ can be expressed as a function of two parameters and, in the case of right ascension and declination, becomes

$$\hat{k} = -(\cos\delta\ \cos\alpha,\ \cos\delta\ \sin\alpha,\ \sin\delta) \qquad (A2)$$

where α, δ are the apparent right ascension and declination relative to true equatorial coordinates of date. The quantity $d\Omega$ represents a differential solid angle such as $\cos\delta d\alpha d\delta$ in the case of right ascension and declination. In the following steps, we will use the wave vector: $\vec{k} = \omega\hat{k}/c$.

The electric field detected at antenna j is given by

$$E_j(t) = E(\vec{x}_j(t),t) = \int_{\hat{k}} \int_0^\infty A(\hat{k},\omega)\ e^{i[\omega t - \vec{k}\cdot\vec{x}_j(t)]}\ d\omega\ d\Omega + c.c. \qquad (A3)$$

where $\vec{x}_j(t)$ is the position of antenna j as a function of true time. (See Section IV for a definition of antenna location.) This signal will be received by the antenna and passed through various filters and mixers. The modeling of the composite effect of instrumentation is discussed in Section IV. Following that derivation, the signal component due to the natural source can be written in the form

$$V_j^q(t_{bj}) = \int_{\hat{k}} \int_0^\infty A(\hat{k},\omega)\ G_j(y_j)\ e^{i[\omega t_j - \vec{k}\cdot\vec{x}_j(t_j) - \alpha_j(\omega,t_j)]} d\omega\ d\Omega + c.c. \qquad (A4)$$

where the doppler-snifted passband argument is given by

$$y_j = \omega(1 - \hat{k}\cdot\vec{x}_j/c) \tag{A5}$$

and where instrumental phase terms are given by

$$\alpha_j(\omega,t_j) \equiv \omega_{hj}\, t_j + \phi_{hj} + y_j\, \tau_{Ij} + \omega\tau_a + \phi_{Ij}(y_j) \tag{A6}$$

As in the text, t_j is the true time that corresponds to bit time t_{bj}.

We will first compute the expectation of the product of two analog signals as described by Eq. (A4) and then compute the normalization. The expectation value of the voltage product is given by

$$\begin{aligned}\langle V_i^q(\hat{t}_{bi})\, V_j^q(\hat{t}_{bj})\rangle = {} & \int_{\hat{k}'}\int_0^\infty\int_{\hat{k}}\int_0^\infty \langle A(\hat{k},\omega)A^*(k',\omega')\rangle G_i(y_i)G_j(y_j')e^{i\psi}\, d\omega\, d\Omega\, d\omega'\, d\Omega' \\ & + \int_{\hat{k}'}\int_0^\infty\int_{\hat{k}}\int_0^\infty \langle A(\hat{k},\omega)\, A(\hat{k}',\omega')\rangle G_i(y_i)G_j(y_j')e^{i\psi_c}\, d\omega\, d\Omega\, d\omega'\, d\Omega' \\ & + \text{c.c.}\end{aligned} \tag{A7}$$

where

$$y_i = \omega\,(1 - \hat{k}\cdot\vec{x}_i/c) \tag{A8}$$

$$y_j' = \omega'(1 - \hat{k}'\cdot\vec{x}_j/c) \tag{A9}$$

$$\psi = \omega\hat{t}_i - \vec{k}\cdot\vec{x}_i(\hat{t}_i) - \omega'\hat{t}_j + \vec{k}'\cdot\vec{x}_j(\hat{t}_j) - \alpha_i(\omega,\hat{t}_i) + \alpha_j(\omega',\hat{t}_j) \tag{A10}$$

and ψ_c is a similar expression that will not be needed. The quantities $\hat{t}_k$ are the offset values for true time corresponding to t_{bk} as in Eqs. (16) and (17) in the text (i.e., $\hat{t}_{bj} = t_{bj} + \Delta$ implies $\hat{t}_j = t_j + \Delta$).

We will assume that the natural source is completely incoherent, which means

$$\boxed{\langle A(k,\omega)\, A^*(k',\omega')\rangle = \frac{1}{2}\, S_p(\hat{k},\omega)\, \delta(\hat{k} - \hat{k}')\, \delta(\omega - \omega')} \tag{A11}$$

where $S_p(\hat{k},\omega)$ is the power spectrum for direction $\hat{k}$ and $\delta(z)$ is a Dirac delta function.[1] That is, emissions from different areas of the source are uncorrelated. Furthermore, the noise emitted by a given area is stationary and therefore possesses uncorrelated frequency components. Since the signal is real, we know

$$A(\hat{k},\omega) = A^*(\hat{k},-\omega) \tag{A12}$$

This relation and Eq. (A11) give

$$\langle A(\hat{k},\omega)A(\hat{k}',\omega')\rangle = \frac{1}{2} S_p(\hat{k},\omega)\ \delta(\hat{k}-\hat{k}')\ \delta(\omega+\omega') \tag{A13}$$

$$= 0 \text{ for } \omega \text{ and } \omega' > 0 \tag{A14}$$

Under these assumptions, Eq. (A7) becomes

$$\langle V_i^q(\hat{t}_{bi})\ V_j^q(\hat{t}_{bj})\rangle = \frac{1}{2}\int_{\hat{k}}\int_0^\infty S_p(\hat{k},\omega)\ G_i(y_i)\ G_j(y_j)\ \exp(i\psi_I)d\omega\ d\Omega + \text{c.c.} \tag{A15}$$

where

$$y_i = \omega\ (1 - \hat{k}\cdot\dot{\vec{x}}_i/c) \tag{A16}$$

$$y_j = \omega\ (1 - \hat{k}\cdot\dot{\vec{x}}_j/c) \tag{A17}$$

$$\psi_I = \omega\ (\hat{t}_i-\hat{t}_j) + \vec{k}\cdot\vec{B}_r - \alpha_i(\omega,\hat{t}_i) + \alpha_j(\omega,\hat{t}_j) \tag{A18}$$

The $A(\hat{k},\omega)\ A(k',\omega)$ term has dropped out since $\omega = -\omega'$ is not covered in the region of the integration. We have also defined a "retarded baseline:"

$$\vec{B}_r \equiv \vec{x}_j(\hat{t}_j) - \vec{x}_i(\hat{t}_i) \tag{A19}$$

Let two particular parameters (β,γ) define the direction vector. Suppose the brightness distribution is very narrow about some reference direction k_a

$$\hat{k}_a = \hat{k}(\beta_a,\gamma_a) \tag{A20}$$

[1] For two particular direction parameters (β, γ), the delta function denotes $\delta(\beta - \beta')\ \delta(\gamma - \gamma')$. Furthermore, we will require β and γ to satisfy the relation $d\beta d\gamma = d\Omega$.

If the brightness distribution is sufficiently compact, we can approximate the wave direction by

$$\hat{k} = \hat{k}_a + \frac{\partial \hat{k}}{\partial \beta}\bigg|_a (\beta - \beta_a) + \frac{\partial \hat{k}}{\partial \gamma}\bigg|_a (\gamma - \gamma_a) \tag{A21}$$

where the partials* are evaluated at the reference point β_a, γ_a. We then obtain

$$\langle V_i^q(\hat{t}_{bi})\ V_j^q(\hat{t}_{bj})\rangle = \frac{1}{2}\int_0^\infty R(u,v,\omega)\ G_i(\bar{y}_i)\ G_j(\bar{y}_j)\ \exp(i\psi_f)\ d\omega + c.c. \tag{A22}$$

where

$$\bar{y}_i = \omega\ (1 - \hat{k}_a \cdot \dot{\vec{x}}_i/c) \tag{A23}$$

$$\bar{y}_j = \omega\ (1 - \hat{k}_a \cdot \dot{\vec{x}}_j/c) \tag{A24}$$

$$\psi_f = \omega\ (\hat{t}_i - \hat{t}_j) + \vec{k}_a \cdot \vec{B}_r - \alpha_i(\omega, \hat{t}_i) + \alpha_j(\omega, \hat{t}_j) \tag{A25}$$

and where

$$R(u,v,\omega) \equiv \int_{-\infty}^{\infty}\int_{-\infty}^{\infty} S_p(\beta,\gamma,\omega)\ e^{-2\pi i[u(\beta-\beta_a)+v(\gamma-\gamma_a)]} d\beta d\gamma \tag{A26}$$

for which

$$u \equiv -\frac{\partial \hat{k}}{\partial \beta}\bigg|_a \cdot \frac{\vec{B}_r}{\lambda} \tag{A27}$$

$$v \equiv -\frac{\partial \hat{k}}{\partial \gamma}\bigg|_a \cdot \frac{\vec{B}_r}{\lambda} \tag{A28}$$

$$\lambda \equiv 2\pi c/\omega \tag{A29}$$

*Structure coordinates are usually defined as $\beta = (\alpha - \alpha_c)\cos\delta_c$ and $\gamma = \delta - \delta_c$ where (α_c, δ_c) is the origin of structure coordinates relative to r.a. and declination. With this definition, the β partial and γ partial are in the direction of increasing right ascension and declination, respectively.

With this definition, u and v are the components of the baseline vector projected on the plane of the sky. Two approximations have been made in Eq. (A22). First, the weak $\hat{k}$ dependence in the bandpass functions has been neglected so that the y_i, y_j values have been evaluated at $\hat{k}_a$. Second, the limits of the (β,γ) integration have been extended to infinity under the assumption that the brightness distribution is very compact and terminates the integration. The function $R(u,v,\omega)$ is referred to as the brightness transform. A more detailed treatment of the brightness transform and of structure effects is given in Ref. 5.

The fringe visibility is the normalized modulus of the brightness transform and is a measure of the spatial extent of the source relative to the resolution of the interferometer for the given observation. It is equal to the ratio of "correlated flux" to total flux and is defined by

$$v_f(u,v,\omega) \equiv \left| \frac{R(u,v,\omega)}{R(0,0,\omega)} \right| \tag{A30}$$

$$= \frac{|R(u,v,\omega)|}{S_p(\omega)} \tag{A31}$$

where $S_p(\omega)$ is the total power emitted by all parts of the source at frequency ω. For a point source, the fringe visibility is unity for all baselines. For a diffuse source, the visibility is unity for a "null" baseline and decreases on average as baseline length increases. The decrease can become substantial for baselines satisfying

$$\left|\vec{B}_r\right| \gtrsim \frac{\lambda}{2d_s} \tag{A32}$$

where d_s is the source diameter in radians and λ is the radio wavelength.

In addition to this normalization of the brightness transform, we must normalize the voltage signal in Eq. (A4). Using Eqs. (A11) and A14), one can easily show that expectation of the squared voltage is given by

$$(V_j^q)^2 = \int_k \int_o S_p(\hat{k},\omega)\, G_j^2(y_j)\, d\omega\, d\Omega \tag{A33}$$

$$= \int_o^\infty S_p(\omega)\, G_j^2(\bar{y}_j) d\omega \tag{A34}$$

where we have again neglected the weak dependence of y_i on $\hat{k}$ and evaluated y_i at the reference position $\hat{k}_a$. Using Eqs. (23), (A6), (A22), (A31) and (A34), we

can now compute the cross-correlation function for the normalized voltage components for the natural source:

$$\langle q_i(\hat{t}_{bi})\, q_j(\hat{t}_{bj})\rangle \equiv \frac{\langle V_i^q(t_{bi}-\tilde{\tau}_{mi}-\ell s)\, V_j^q(t_{bj}-\tilde{\tau}_{mj})\rangle}{\left[\langle (V_i^q)^2\rangle \langle (V_j^q)^2\rangle\right]^{1/2}} \tag{A35}$$

$$= \frac{v_f}{2D_N} \int_0^\infty S_p(\omega)\, G_i(\bar{y}_i)\, G_j(\bar{y}_j)\, e^{i\psi_f}\, d\omega + \text{c.c.} \tag{A36}$$

where

$$D_N^2 \equiv \int_o^\infty S_p(\omega)\, G_i^2(\bar{y}_i)\, d\omega \int_o^\infty S_p(\omega)\, G_j^2(\bar{y}_j)\, d\omega \tag{A37}$$

and, like Eq. 27,

$$\psi_f = \omega\,(\tau_g' + \tau_b + \tau_I + \tau_a - \tilde{\tau}_{mi} + \tilde{\tau}_{mj} - \ell b) + \phi_h - \omega_{hj}\,\tilde{\tau}_{mj} + \omega_{hi}(\tilde{\tau}_{mi} + \ell b) + \phi_I + \phi_B \tag{A38}$$

in which τ_b, τ_I, τ_a, and ϕ_I are differences between station quantities in the order j minus i.

As explained in the text, the quantity $\tau_b = t_i - t_j$ is the difference between the errors in the bit times of the two stations. We have pulled v_f out of the integral, recognizing that resolution of the source will vary very little across a 2-MHz passband located at RF. A phase term ϕ_B has been added to fringe phase ϕ_f to represent the phase term from the brightness transform R. Further, we have used the definition of the instrumental phase from Eq. (A6), properly offset in time. In analogy with Eq. (26), a definition of an interim geometric delay has been made:

$$\omega\tau_g' \equiv \hat{k}_a \cdot \vec{B}_r \tag{A39}$$

$$= \hat{k}_a \cdot [\vec{x}_j(t_j-\tilde{\tau}_{mj}) - \vec{x}_i(t_i-\tilde{\tau}_{mi} - \ell s)] \tag{A40}$$

where we have used the reference position $\hat{k}_a$ of the extended source.

As indicated in Eqs. (16) and (18), the final expression (Eq. 19) for the cross-correlation function of an extended source is obtained by multiplying Eq. A36 by $2/\pi$ and by a noise temperature factor. One can easily show that this result for an extended source is the same as that for a point source except that (a) an amplitude factor ($v_f \leq 1$) must be included, (b) a phase shift due to structure must be added to the phase, and (c) the interim delay τ_g' is computed relative to the reference position k_a.

APPENDIX B

BIT MANIPULATIONS IN THE CIT/JPL MARK II CORRELATOR

The JPL/CIT Mark II correlator has the capability of simultaneously processing up to five stations, including all 10 possible baselines. There are two stages in processing: single-station delay offsetting followed by two-station (pairwise) operations. Figure B1 illustrates these two types of operations in a 5-station application and shows the numbering system for station pairs. Figure B2 presents in greater detail the operations performed on a particular pair. Each bitstream is offset by a single-station model delay whose geometric component is the transit time between the station and the earth center of mass. The single-station delay for station i is given by

$$\tau'_{mi} = -\frac{\hat{k}_m \cdot \vec{x}_{mi}(t_G)}{c} + \tau_{ti} + \tau_{ci} \qquad \text{(B1)}$$

where the first term is the geometric delay relative to the earth center of mass, expressed in terms of station location $\vec{x}_{mi}$ and apparent wave direction $\hat{k}_m$ (both in geocentric coordinates). The term τ_{ti} represents the troposphere delay along the raypath to antenna i, while τ_{ci} represents the station clock error (offset and rate). The single-station approach works because the resulting differential offset between the two members of a pair of bitstreams will contain the differences for all important delay components. For example, the resulting difference in geometric delays can easily be shown to equal the desired geometric delay (Eq. 26) between antennas (except for small effects due to argument offsets that are accounted for in post-correlation software).

The pairwise operations illustrated in Fig. B2 consist of the following steps. Since the difference between two rounded numbers is not necessarily equal to the rounded difference between the raw numbers, the relative offset between two separately rounded and offset bitstreams can be in error by as much as ±1 bit relative to the desired rounded two-station delay. Thus a pairwise vernier correction (1, 2, or 3 bits) is applied to the first bitstream of each station pair, where a 2-bit delay corresponds to zero correction. The same bitstream is then simultaneously subjected to each of a number (16) of lags. At the same time, the second bitstream is delayed by 10 bits so that its pairwise delay will match the total pairwise delay (for zero vernier correction) applied to the first bitstream in order to reach the reference lag (#8) for that bitstream (i.e., 2-bit vernier + 8 lags = 10 bits). The second bitstream is then multiplied in quadrature by two pairwise stopping functions ($\cos\phi_m$, $\sin\phi_m$) with phase (and rate) given by Eq. 28. The computation of phase through Eq. (28) must be based on total delays (τ_{mi}) used by the correlator in offsetting to the reference (central) lag. That is, for each bitstream, the total unquantized delay is equal to the single-station delay (Eq. B1) plus 10 bits (i.e., $\tau_{mi} = \tau'_{mi}$ + 10 bits). The quantized delay τ_{mi} in Eq. 30 is equal to τ_{mi} rounded to the nearest bit except that τ_{mi} for the first bitstream is shifted by (-1, 0, +1) bit according to the vernier delay setting. After these pairwise operations, the two bitstreams (one now complex) are multiplied bitwise and a complex sum over bits is performed for each of the 16 lags applied to the first bitstream.

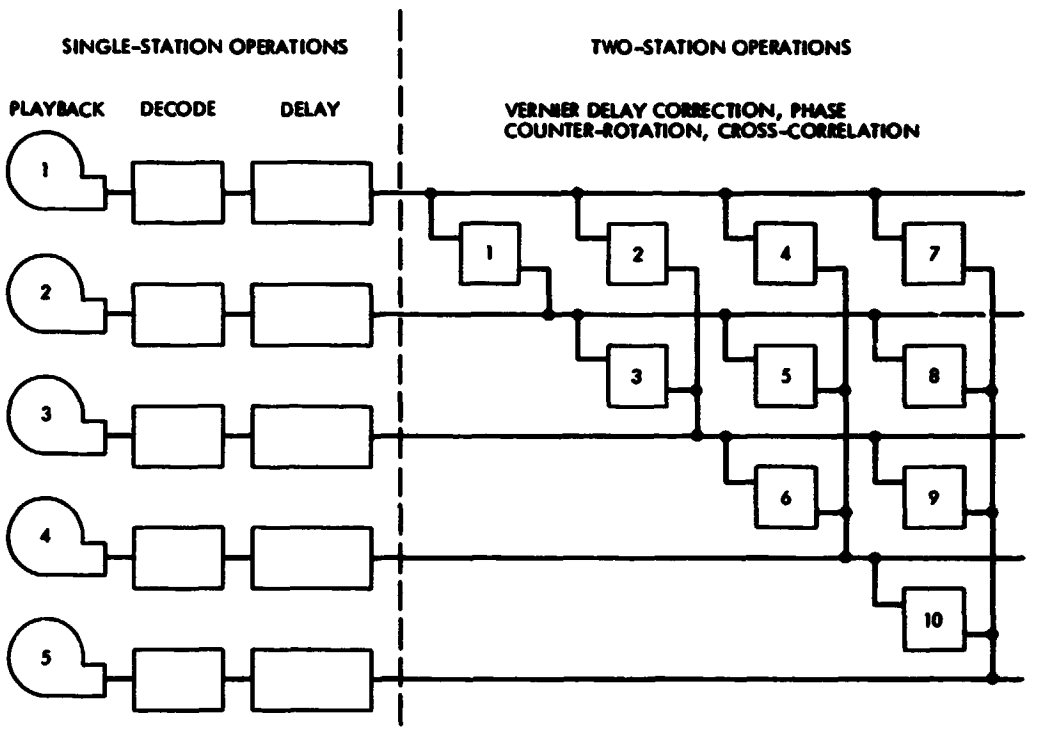

Fig. B1. Block diagram of the CIT/JPL Mark II multistation/correlator

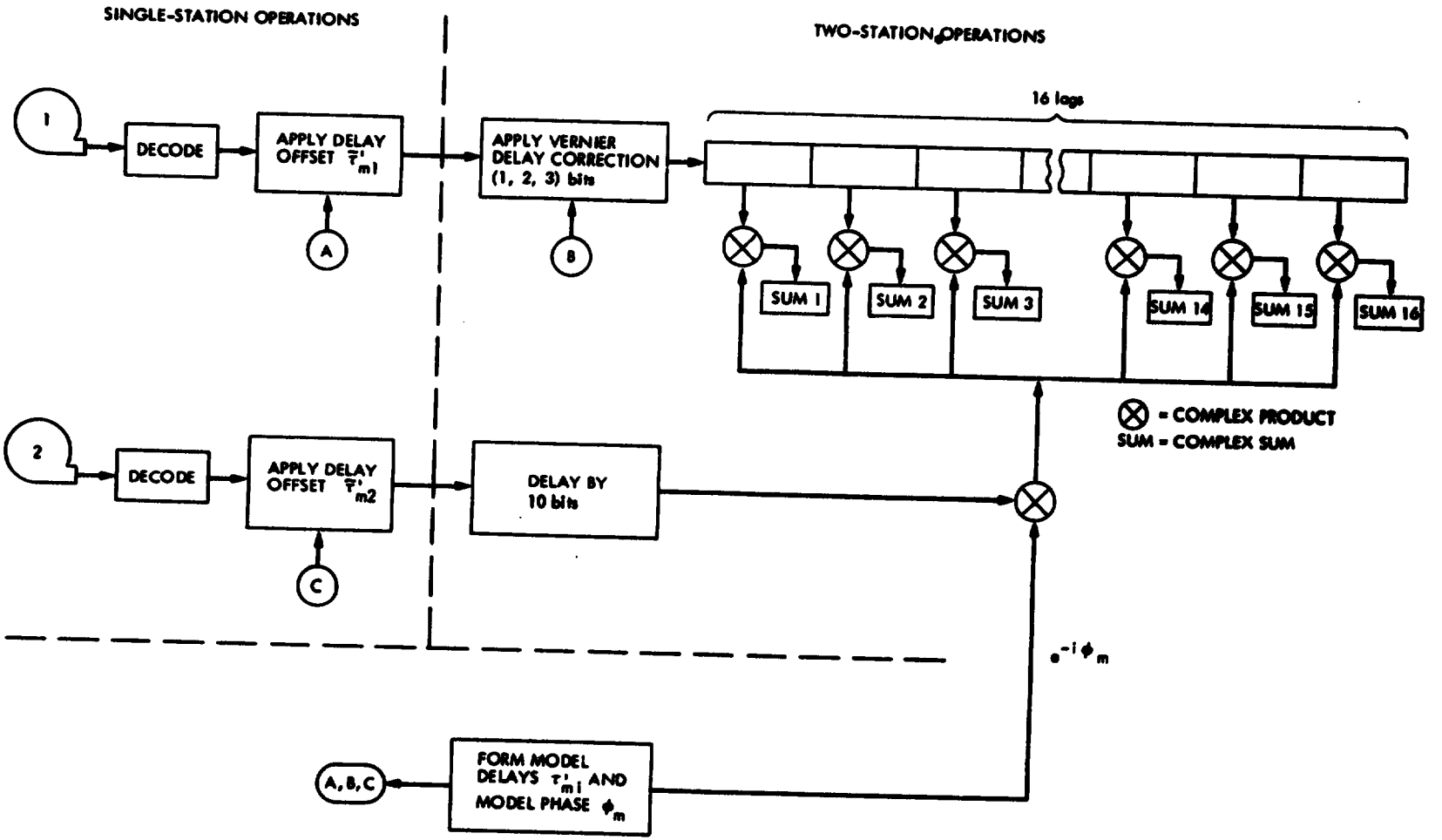

Fig. B2. Schematic diagram of two-station cross-correlation with the CIT/JPL correlator

Figure B3 illustrates in terms of devised bits these bit manipulations for two bitstreams as they pass through the correlator. For the two possible levels of the recorded signal, a plus sign (minus sign) is used to denote a +1 (-1). Contrary to the impression created by the figure, the bits are processed serially, not simultaneously. The figure depicts a correlation interval of 8 bits even though correlation (averaging) intervals are typically 0.2 - 1.0 seconds (0.8 - 4 megabits) in length. No signal pattern has been made evident in the two bitstreams since the signal is typically much less than system noise for each 1-bit sample point. As indicated above, the first step is to offset both bit-streams by their respective single-station delays given by Eq. B1 but rounded to the nearest bit. For illustration, those delays have been set equal to very small numbers (<3 bits) even though in practice they could be as large as 20 msec (8×10^4 bits). After single-station offsetting, one bit-stream (left) is subjected to the 1-bit vernier correction for roundoff errors, while the other bitstream is multiplied by the quadrature stopping functions. For simplicity in the pairwise operations, the vernier delay is represented as (-1, 0, +1) bit rather than (1, 2, 3) bit; only one lag offset (i.e., no offset) is shown for the left bitstream; and, consequently, the related 10-bit delay that would have been required for referencing the right bitstream to the central lag (the only lag in the example) is unnecessary. The stopping sinusoids are quantized to three amplitude levels equal to (-1, 0, +1). Over a cycle of stopped phase, the quantization subintervals are 3/8 cycle at +1, 1/8 cycle at 0, 3/8 cycle at -1 and 1/8 cycle at 0, with appropriate shifting for sine and cosine. One can readily show that the amplitude of the first harmonic is equal to 1.176 for this quantization scheme. For our example, the fringe rate has been set equal to $(8 \text{ bits})^{-1}$ or 0.5 MHz in order to make each quantization subinterval equal to a small integer number of bits. This rate, of course, is much greater than the normal VLBI rates, which are 25 kHz or less at X-band. After multiplication by the quadrature stopping functions, the second bitstream has branched into two "counter-rotated" bitstreams, with some bits blanked out by the zeros in the stopping function.

The two bitstreams derived from the second station are separately multiplied by the first bitstream to give two cross-correlated bitstreams. The bits in each of the product bitstreams are summed over the correlation interval to obtain the excess (or deficit) of +1's relative to -1's. When divided by the total number of bits in the sum (see N_t in Eq. 30), the two sums become the real and imaginary parts of the complex stopped fringes for which the theoretical expectation value is given by Eq. 37 with $a_1 = 1.176$ and $\ell = 0$. The time tag (i.e., bit time $t_G = t_{bi} = t_{bj}$ in Eq. 29) for the correlation coefficients is the center of the sum interval in (unshifted) UT seconds.

Phase calibrator tones are extracted in the correlator by means of an artificial application of the cross-correlation operations. To set up for single-station tone stopping, each playback bitstream is cross-correlated with (multiplied by) an artificial bitstream filled with +1's. The artificial "DC" bitstreams are constructed in some or all of the bitstream channels left unoccupied by real data. The model phase used for quadrature tone stopping is made to equal Eq. 60 by an artificial assignment of the parameter values in the interferometer phase model in Eq. (28). Since tone stopping requires the use of unoccupied bitstream channels (see Fig. B1), the maximum number of tones/frequency channel that can be extracted in a single pass through the correlator (without time-multiplexing between tones within a channel) is $5 - N_r$ is the number of real bitstreams being

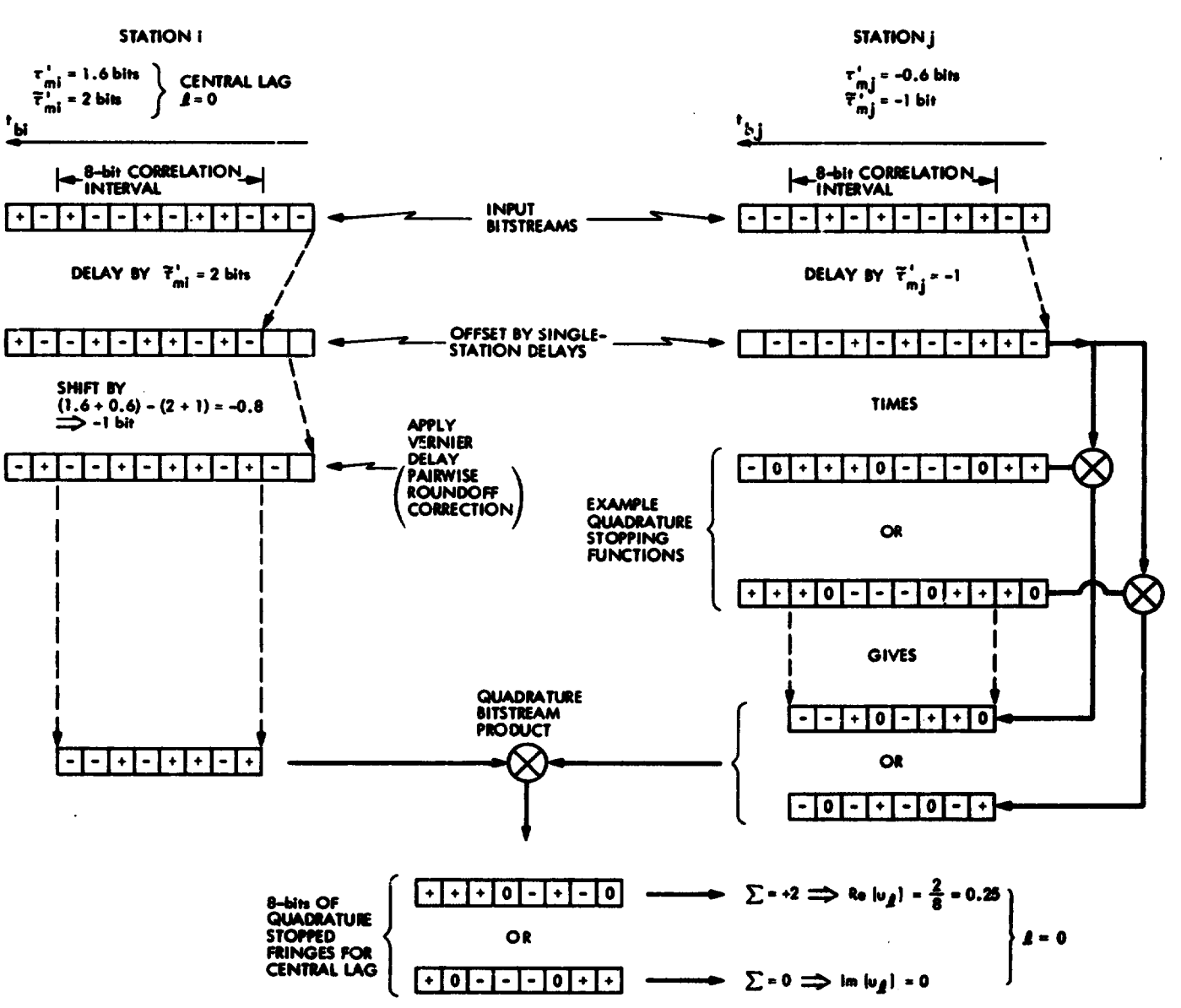

Fig. B3. Bit manipulations with the CIT/JPL Mark II correlator

processed. Thus, for two-antenna processing, a maximum of three continuous tones/frequency-channel can be obtained. By correlator design, more tones/channel could be obtained by time-multiplexing between tone phase models. However, as one increases the number of input bitstreams, increases the number of time-multiplexed frequency channels, decreases the dwell time per channel or increases the number of time-multiplexed tones within a channel, greater demand is placed on the available memory and computing power of the correlator. It is beyond the scope of this report to discuss correlator limits for these parameters.

APPENDIX C

REFORMULATION AND ILLUSTRATION OF FRINGES IN THE LAG DOMAIN

This appendix reformulates the stopped fringes in Section VI to place them in the form that is commonly used in the lag domain. An example of stopped fringes is presented.

The identity

$$e^{i\bar{\omega}\Delta\tau_\ell}\, e^{-\bar{\omega}\Delta\tau_\ell} = 1 \tag{C1}$$

can be used to place the stopped fringes of Eq. (37) in the form

$$\boxed{\langle u_\ell(t_G)\rangle = a_1 \frac{r_m}{\pi} D_c(\Delta\tau_\ell)\, e^{i[\Delta\bar{\psi}_f - (\bar{\omega}-\omega_{hi})\ell b]}} \tag{C2}$$

where the delay function is given by

$$D_c(\Delta\tau_\ell) \equiv \frac{1}{D_N} \int S_p(\omega)\, G_i(y_i)\, G_j(y_j)\, F_q\, e^{i(\omega-\bar{\omega})\Delta\tau_\ell}\, d\omega \tag{C3}$$

and where the overall residual fringe phase at the reference lag (ℓ=0) is given by

$$\Delta\bar{\psi}_f = \Delta\phi_h + \bar{\omega}\Delta\tau + \phi_I + \phi_B \tag{C4}$$

and residual delay by

$$\Delta\tau_\ell = \Delta\tau - \ell b \tag{C5}$$

The frequency $\bar{\omega}$ will be equal to the centroid of the bandpass product. One can show that this choice for $\bar{\omega}$ will relegate virtually all of the time dependence in the fringes to the fringe phase $\bar{\psi}_f$.

Suppose that the natural source spectrum $S_p(\omega)$ is flat and that the bandpass shapes at the two stations are identical. Under these assumptions, the delay function becomes

$$D_c(\Delta\tau) = \frac{1}{D_N'} \int G(y_i)G(y_j)F_q e^{i(\omega-\bar{\omega})\Delta\tau}\, d\omega \tag{C6}$$

where D_N in Eq. (21) becomes

$$D_N' = \int G^2(\omega)d\omega \tag{C7}$$

Given the bandpass shape, the quantization filter F_q, and the doppler shift in y_i and y_j, this integral can be readily evaluated. The simple case of a rectangular bandpass of width W_b proceeds as follows. The BLKO system operates in the single-sideband mode in which the total mixing frequency is placed at the edge of the 2-MHz passband. If the doppler shift at station j is D_j and the total mixing frequency is f_j, then the centroid frequency will be

$$\frac{\bar{\omega}}{2\pi} \equiv \frac{f_i + f_j \pm W_b - D_i - D_j}{2} \tag{C8}$$

where the plus (minus) sign is used for upper (lower) sideband. Effective bandpass width will restrict the limits on the integral in Eq. (C7) to the range

$$\omega = \bar{\omega} \pm W_d/2 \tag{C9}$$

where W_d is the bandpass overlap after doppler-shifting given by

$$W_d = W_b - |f_j - f_i + D_i - D_j| \tag{C10}$$

provided there is overlap. Given these values, the integral in Eq. C6 becomes

$$D_c(\Delta\tau) = \frac{W_d}{W_b} \frac{\sin(\pi W_d \Delta\tau)}{\pi W_d \Delta\tau} \tag{C11}$$

where we have assumed $F_q = 1$. The factor W_d/W_b, which lies between zero and one, is the ratio of actual overlap to total bandwidth. It gives the fractional power remaining after doppler shifting has caused misalignment of the two station bandpasses and has thereby dropped power at the bandpass edges. For the BLKO system, such losses are almost negligible since doppler shifting is very small relative to a 2-MHz bandwidth. For example, the maximum doppler shift at X-band is about 20 kHz so that $W_d/W_b \geq 0.99$. (In the BLKO system, $f_i - f_j$ is often zero since the same mixing frequencies are often used at both stations. In narrowband systems, the mixing frequencies are sometimes given different values so that their difference compensates for the bandpass misalignment caused by doppler shifting.)

Thus for a rectangular bandpass, the stopped fringes are given by

$$\boxed{\langle u_\ell(t_G)\rangle = a_1 \frac{r_m}{\pi} \frac{W_d}{W_b} \frac{\sin(\pi W_d \Delta\tau_\ell)}{\pi W_d \Delta\tau_\ell} e^{i[\Delta\bar{\psi}_f - (\bar{\omega}-\omega_{hi})\ell b]}} \tag{C12}$$

where $\Delta\bar{\psi}_f$ is given by Eq. (C4). If power loss due to doppler shifting is negligible ($W_d/W_b = 1$), the maximum amplitude of the fringes is given by $a_1 r_m/\pi$ for perfect bitstream alignment ($\Delta\tau = 0$).

Examples of lag-domain fringes that correspond to the frequency-domain fringes in Fig. 3 are given in Fig. C1 and are plotted as a function of time for three lags (ℓ). Note the phase shift of about $\pi/2$ between the sinusoids for adjacent lags. This shift is a consequence of the term $(\bar{\omega}-\omega_{hi})\ell b$ in Eq. (C2), which is caused by lag offsetting of bitstream i. Since the average (centroid) frequency at baseband $(\bar{\omega} - \omega_{hi})$ is about 1 MHz, a shift of one lag will produce a phase shift equal to

$$\frac{1}{2\pi}(\bar{\omega}-\omega_{hi})b \approx \pm 1 \text{ MHz} * 1 \text{ bit} \qquad \text{(C13)}$$

$$\approx \pm 0.25 \text{ cycle}$$

where the ± pertains to upper and lower sidebands. The actual phase shift is slightly smaller (≈0.22 cycles) since the bandpass falls off before reaching 2 MHz. In fringe stopping, the same stopping phase is used for the fringes for all lag offsets so that this phase jump between lags is not removed. Also displayed in this figure are fit fringes based on the model in Eq. (C12), where the bandwidth (W_b=W_d) has been set equal to 1.8 MHz. In the fit, the behavior of the amplitude as a function of lag allows determination of the fringe amplitude and BSA delay. For the first section, one can visually fit a sin x/x function to the amplitude vs lag in Fig. C1 and verify the fringe amplitude of ~800 and the BSA delay of ~0.3 bit that result from phase-tracking. By noting the zero crossings, one can also verify the fringe rate of about 21 mHz and the fringe phase of about 0.5 cycle at the indicated midsection reference time. The SNR per fringe point is about 8 in this example.

With regard to amplitude, the solve-for amplitude in the lag-domain should be approximately equal to $a_1 r_m/\pi$ (see Eq. C2) since no amplitude scaling is provided in the lag-domain model fringes. This amplitude is smaller than the frequency-domain result by about a factor of 2.0 due to amplitude scaling through BAMPL, as explained in Section X.

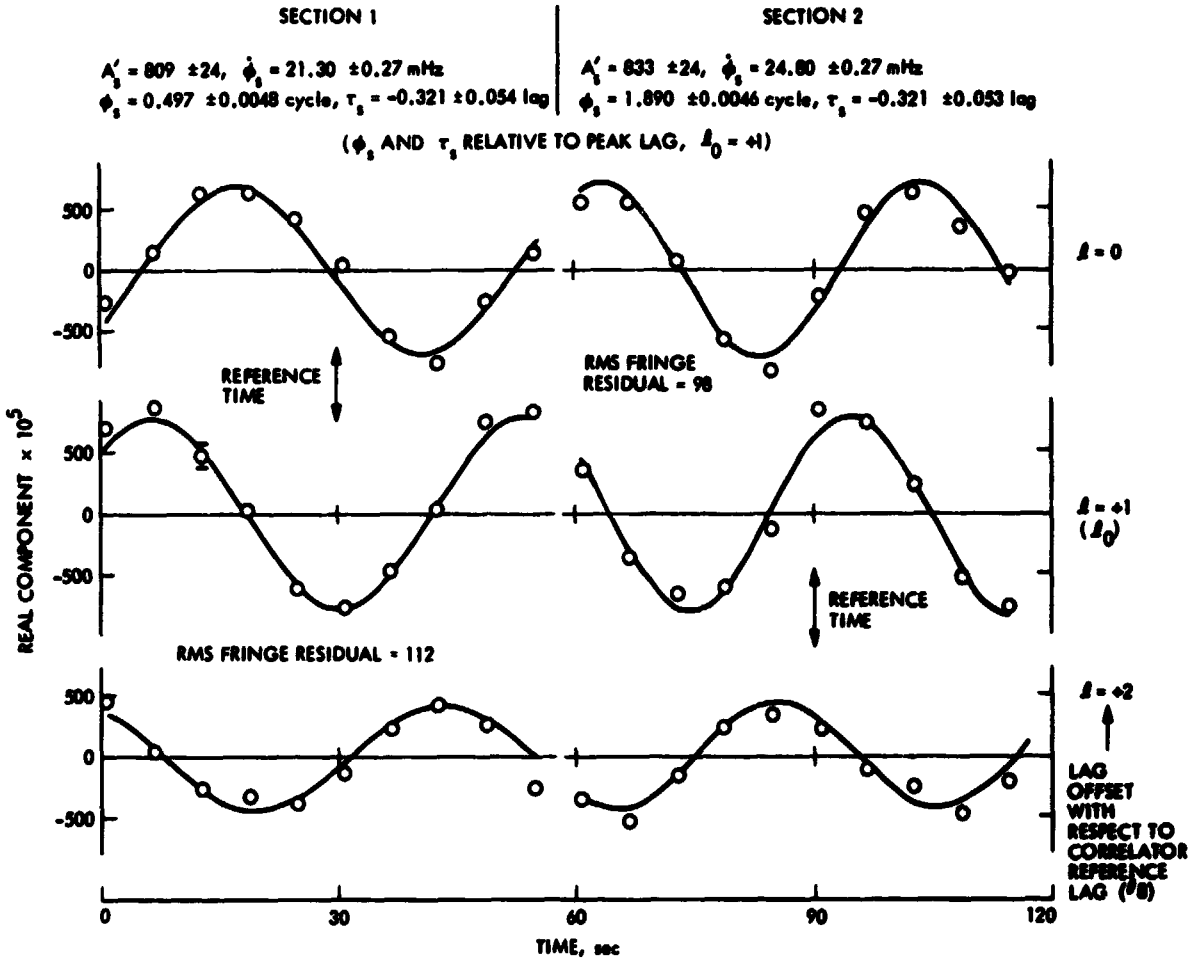

Fig. C1. Long-baseline example of stopped fringes in the lag domain

APPENDIX D

QUANTIZATION FILTER

This appendix obtains an expression for the quantization (fractional-bit-shift) filter by evaluating the sum

$$F_q(z) = \frac{1}{N_t} \sum_{t_G} e^{iz(\tau_m - \tilde{\tau}_m)} \tag{D1}$$

We will assume in the following analysis that the correlator keeps the quantized model delay within 0.5 bit of the model delay (i.e., $|\tilde{\tau}_m - \tau_m| \leq b/2$). If one assumes that delay rate ($\dot{\tau}_m$) is constant across the sum (correlation) interval (which it very nearly will be for correlation intervals as short as 1 sec or less), then the sum over time can be converted to an integral over τ. The integral over τ, however, must be broken into intervals with boundaries at bit jump points.

We will model the general case in which the quantization error ($\Delta\tau = \tau_m - \tilde{\tau}_m$) exhibits the following behavior. In the first interval with continuous behavior, let $\Delta\tau$ progress from $\Delta\tau_1$ to b/2. This will be followed by N_q intervals in which $\Delta\tau$ traverses its full range from -b/2 to b/2. In the final interval, $\Delta\tau$ then changes from -b/2 to $\Delta\tau_2$. By evaluating the appropriate integral in each interval and summing, one can show that the quantization filter will be equal to

$$F_q(z) = \frac{1}{\tau_{m2} - \tau_{m1}} \left[\frac{e^{iz\Delta\tau_2} - e^{iz\Delta\tau_1}}{iz} + N_J b \, \frac{\sin zb/2}{zb/2} \right] \tag{D2}$$

where τ_{m1} and τ_{m2} are the initial and final values of τ_m, respectively, and where N_J is the number of "jumps" in the quantized delay τ_m over the full correlation interval ($N_J = N_q + 1 = \tilde{\tau}_{m2} - \tilde{\tau}_{m1}$). Equation D2 is quite general and is valid when there are no jumps in the quantized delay ($N_J = 0$) and when the delay rate is negative ($\tau_{m2} - \tau_{m1} < 0$ and $N_J < 0$).

Two limiting cases are of interest. First, in the limit of large N_J, the quantization filter introduces no phase shifts and, as one would expect, becomes a pure sin x/x filter. This is also true whenever $\Delta\tau_1 = \Delta\tau_2 = 0$ and $|N_J| > 0$. Second, as the delay rate approaches zero, we will have $\tau_{m2} - \tau_{m1} \to 0$ and $N_J = 0$. In this limit, we obtain the expected result

$$F_q(z) = \exp[iz(\tau_m - \tilde{\tau}_m)] \tag{D3}$$

where τ_m is the delay at the middle of the correlation interval.

The most important feature of the formulation of the quantization filter in Eq. (D2) is that only the initial and final values for τ_m are needed to compute the composite effect of quantization over the whole interval. Given the initial and final values, one can easily compute $\tau_{m2} - \tau_{m1}$, $\Delta\tau_1$, $\Delta\tau_2$ and N_J. For this reason, τ_{m1} and τ_{m2} values for each correlation interval are numerically passed to the modeling subroutine in PHASOR.

APPENDIX E

ERRORS IN THE LAG-TO-FREQUENCY TRANSFORMATION

In the transformation of the fringes from the lag domain to the frequency domain, the use of a limited number of lags can introduce errors in the output phase and amplitude. This appendix develops a model to assess the magnitude of such errors as a function of the total number of lags used in the transform.

To stress the important features in the lag transform, we cast the fringes of Eq. (37) in the form

$$\langle u_\ell \rangle \propto \int_0^\infty H(\omega') e^{i\omega'(\Delta\tau' - \ell b)} \, d\omega' \qquad \text{(E1)}$$

where $H(\omega')$ is equal to the bandpass product $S_p G_i G_j$ and ω' is the translated frequency $\omega' = \omega - \omega_{hi}$. We will neglect doppler shifting and will assume that the two bandpasses are identical ($G_i G_j = G^2$). The delay $\Delta\tau'$ is the residual after all model terms are subtracted. In this appendix, we will let the integer ℓ equal zero at the central lag, which is chosen, of course, to cancel all but the fractional bit part of $\Delta\tau'$. Thus the "remaining" $\Delta\tau'$ will fall between ±0.5 bit. Although we will not do it here, it can be shown that the quantization filter F_q has little effect on the transformation errors and can be neglected. All phase terms independent of frequency have been discarded since they will only cause a phase shift in the transformed fringes and have no effect on lag transform errors (although they are otherwise important).

The error calculation proceeds as follows. For a given bandpass-product shape and delay $\Delta\tau'$, the integral in Eq. (E1) is calculated numerically for each of N_ℓ values of ℓ centered about the central lag, thereby simulating the processor output. The resulting N_ℓ complex numbers are then subjected to the limited inverse transformation in Eq. (40), which is the way the postcorrelation software transforms the fringes to the frequency domain. The resulting complex numbers in the frequency domain will belong to frequency "bins" centered at the frequencies in Eq. (43). These frequency-domain values should be approximately equal to the complex input integrand in Eq. (E1) (without ℓs) at each frequency bin.

An example of the process is shown in Figs. E1a and E1b for a nine-lag transform and a Butterworth filter approximating the BLKO bandpass. The solid lines represent the input amplitude (G^2) and phase ($\omega'\Delta\tau'$) in the frequency domain, while the points represent the limited-lag transform output that should be approximately equal to this input. For this particular case, the output amplitude deviates from the input amplitude by as much as 9%, relative to maximum amplitude, while the output phase oscillates about the input phase by about ±0.5 millicycles. The directions of the deviations in this example are fairly typical, although the magnitudes are not.

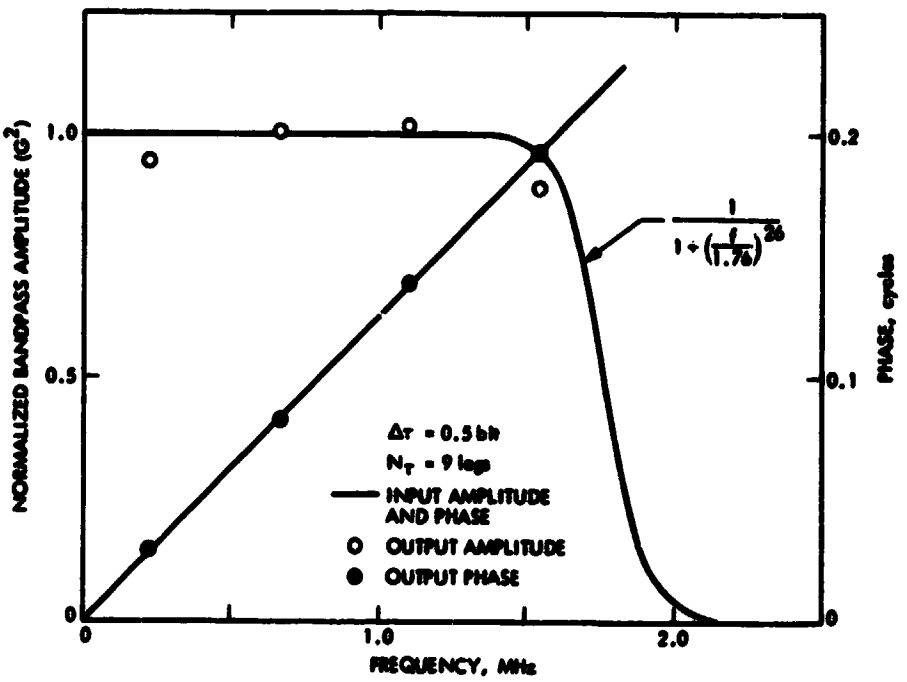

Fig. E1a. An example of limited-lag transformation errors for an ideal Butterworth filter

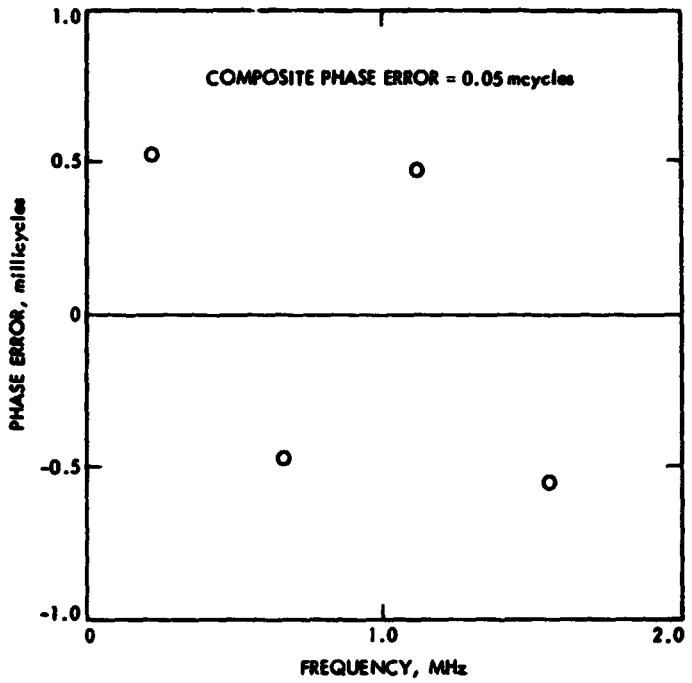

Fig. Elb. Plot of phase errors in Fig. Ela on a finer scale

Since complete results for all cases would be too lengthy, we have summarized in Table E1 the transformation errors calculated for certain useful cases. Bandpass A roughly approximates the BLKO bandpass, while bandpass B is somewhat wider as explained in the table caption. The table was constructed as follows. For a given bandpass shape and given lag count, the transformation errors were calculated for various values of $\Delta\tau'$ between ±0.5 bit. Results are shown only for odd bin frequencies [$n/(2N_\ell)$, n odd]. It was found that the amplitude errors for fixed bandpass and fixed lag count (N_ℓ) are virtually independent of $\Delta\tau'$ while the phase errors depend strongly on $\Delta\tau'$. The table gives only the maximum error in bin phase across the bandpass for the worst case of $\Delta\tau'$. In addition, the table lists the worst-case error in aggregate phase (referenced to the bandpass center) obtained from a weighted least-squares fit of a linear function of frequency to the bin phase errors. In the fit, the bin-phase values were weighted by the square of the bin amplitude. (As suggested by Section X, such a fit is implicitly performed when the transformed fringes are phase-tracked.) Due to the oscillation of the bin errors, the worst-case error in aggregate phase is typically much smaller than the bin phase errors. The error in aggregate phase falls to an acceptable level ($\lesssim$0.001 cycle) at 7 or 8 lags. From the table, it appears that a 9-lag transform yields the smallest phase errors, both bin and aggregate, for N_ℓ below 12. For N_ℓ = 9, bin-phase errors are less than a millicycle and aggregate phase error is less than 0.1 millicycle.

With regard to amplitude errors, the table also gives, for each case, (a) the largest discrepancy between input amplitude and output amplitude across the passband, expressed as a percentage of input amplitude, and (b) an estimate of aggregate amplitude error for the case in which bin amplitude in fringe fitting is approximated with the actual bandpass amplitude in Eq. (71) (i.e., the bin amplitude for $N_\ell \to \infty$). From the table, we see that the worst bin-amplitude error usually occurs at the first or last bin in the bandpass, where edge effects are most significant. The aggregate amplitude error is 2 or 3% when the lag number is 9. For very accurate amplitude work, this error can be eliminated in principle by making accurate measurements of the bandpass shape and calculating bin amplitudes by means of the simulation analysis described above. Although it does not appear to be necessary for any current applications, bin-phase errors could be largely eliminated in a similar fashion.

A word of caution is necessary in using these results. While the numerical values can provide a useful rough estimate of transformation errors, the simulated errors might deviate considerably from actual errors. The main reason is that actual bandpass shapes can deviate considerably from the assumed ideal Butterworth shapes. More accurate representations of bandpass shape might lead to large changes in aggregate phase errors, which were reduced to small values by cancellation of large bin-phase errors of varying sign.

The shape of the transform bandpass obtained in this appendix can be used to compute nominal values for BAMPL, the four-element array in PHASOR for normalizing bin amplitudes in frequency-domain fits. On the basis of Eqs. (45) and (49), one can readily show that

$$\text{BAMPL} = 1.176\,\frac{2}{\pi}\,\frac{1}{0.75}\,\frac{1}{0.88}\,(0.94,\ 1.0,\ 1.02,\ 0.89) \qquad \text{(E2)}$$

Table E1. Transformation errors from limited-lag transforms [Bandpass A (≈BLKO) is an ideal 13-pole Butterworth filter with -3 dB at 1.76 MHz; Bandpass B is an ideal 7-pole Butterworth with -3 dB at 1.83 MHz]

Lag count N_ℓ	Band pass	Largest bin-phase error, mcycle	Largest composite phase error, mcycle	Largest bin amplitude error,* %	Composite amplitude error* %
4	A	10.4	1.1	-21	-12
	B	6.0	0.5	-13	-8
5	A	5.8	2.5	-7	-2.0
	B	5.7	2.4	-7	-2.1
6	A	10.3	1.0	-17	-5.8
	B	5.1	0.8	-9	-3.7
7	A	1.6	0.5	-7	-3.3
	B	2.0	0.6	-7	-2.6
8	A	9.0	0.25	+5	-0.5
	B	3.7	0.03	-6	-1.5
9	A	0.55	0.05	-9	-3.1
	B	0.51	0.05	-6	-1.8
10	A	7.5	0.02	-7	-0.2
	B	2.4	0.10	-7	-1.2
11	A	1.7	0.17	-10	-2.5
	B	0.2	0.02	-7	-1.4
12	A	5.3	0.15	+7	-0.7
	B	1.3	0.02	-6	-1.0

*As percent of maximum input amplitude.

where the first factor is a_1 and 0.88 is the value of G_A in Eq. (50) computed on the basis of the bandpass shape (solid curve) in Fig. E1a. (More exactly, for constant S_p and identical band passes at both stations, G_A becomes $\overline{G}^2$ after S_p has cancelled in numerator and denominator of Eq. 49). The four numbers in the array are the four bin amplitudes in Fig. E1a. The new factor 0.75 enters because the correlator divides by the number of unblanked bits ($0.75N_t$) rather than the total number of bits (N_t). The overall value for the BAMPL array becomes

$$\text{BAMPL} = (1.07,\ 1.14,\ 1.16,\ 1.01) \qquad \text{(E3)}$$

These values for BAMPL are used as the default values in PHASOR. These BAMPL values correspond to a "b-factor" of about 2.0 whereas experimental determinations of the b-factor have resulted in a value about 25% larger. That is, if the default BAMPL array is used, the output amplitudes are reported to be about 20% too small. The cause of the bulk of this discrepancy is not currently known.

APPENDIX F

THE PHASE CALIBRATION SIGNAL

This appendix treats the phase calibrator signal and includes an analysis of (a) tone power, (b) the effect of bilevel clipping on the recorded signal, (c) tone stopping, and (d) stopped-tone SNR. Since it is not necessary for these topics, this appendix will not decompose tone phase into signal-path components but will treat it as a single variable. An analysis of the components of tone phase is given in the text.

The analog baseband signal (before clipping) can be represented in the form

$$V(t) = S(t) + \sigma_N d(t) \tag{F1}$$

where S(t) is the total calibrator signal and the second term is additive noise, which includes instrumental effects, sky noise and source noise. We have normalized the noise to unity (i.e., $\langle d^2 \rangle = 1$) and included a factor σ_N equal to the rms voltage of the noise term.

The calibrator signal can be decomposed in terms of its harmonics to give

$$V(t) = \sum_n v_n \cos \phi_n + \sigma_N s(t) \tag{F2}$$

where ϕ_n is the phase of the n^{th} tone and v_n is the maximum voltage of the n^{th} tone. For more detail concerning ϕ_n, see Eq. (57) and the discussion in the text. The amplitude v_n will be discussed below.

Total power of the calibrator signal is given by

$$P_s \propto \frac{1}{2} \sum_n v_n^2 \tag{F3}$$

while the power of the noise term is given by

$$P_N \propto \sigma_N^2 \tag{F4}$$

If we specify total calibrator power relative to total noise power (both within passband), we can express the tone amplitude in terms of σ_N. That is, if the ratio (P_S/P_N) of total calibrator power to total noise is ε, then the ratio (SNR) of tone amplitude to rms noise voltage becomes

$$\frac{\bar{v}}{\sigma_N} \approx \sqrt{\frac{2\varepsilon}{N_h}} \tag{F5}$$

where N_h is the number of tones in the passband, and $\bar{v}$ is maximum tone amplitude, ideally assumed to be the same ($v_n = \bar{v}$) for all tones in the passband. (It is unnecessary for our purposes to resolve the uncertain status of tones on the passband edges.) We currently plan to keep the total calibrator power low — about 2% of the system noise. Thus, if there are three tones in the passband, the SNR for a tone becomes

$$\frac{\bar{v}}{\sigma_N} \approx \sqrt{\frac{2 \times 0.02}{3}} \approx 0.12 \qquad \text{(F6)}$$

(For all examples, we will assume a nominal system with a 2% power level and 3 tones/passband. It is outside the scope of this report to determine optimum values for these parameters.) This "single-sample" SNR is large compared to that of typical intercontinental cross-correlation fringes, which are usually in the range of 0.001 to 0.04. The tone SNR will be modified slightly below when two-level sampling is taken into account and will increase when many bits are collected in the tone-stopping process.

The maximum amplitude of the signal S occurs whenever all tones are in phase and is given by

$$\frac{S_{max}}{\sigma_N} \approx \frac{N_h \bar{v}}{\sigma_N} \qquad \text{(F7)}$$

This maximum occurs, of course, every time a calibrator pulse reaches the recorder and equals about 0.35 for the example above. (The pulse width at baseband is approximately equal to the inverse of the system bandwidth when a number of tones are in the passband.)

As indicated in the text, the baseband signal is subjected to bilevel sampling and recorded at 4 Mbit/sec. We will use a tilde (~) to denote the bilevel value (±1) at each sample point. Unlike interferometric cross-correlation in which both the signal and noise are random, here the tone signal is deterministic and the noise d(t) is random. Thus the expectation of a sample point becomes

$$\langle \tilde{V} \rangle = \int_{-\infty}^{\infty} Q(V)P(V)dV \qquad \text{(F8)}$$

where the sampling function is given by

$$Q(V) = +1, \; V > 0 \qquad \text{(F9)}$$

$$= -1, \; V < 0$$

and where the probability distribution of V (about S in Eq. F1) is given by

$$P(V) = \frac{1}{\sqrt{2\pi}\,\sigma_N} \exp[-(V-S)^2/(2\sigma_N^2)] \tag{F10}$$

Equation (F8) becomes

$$\langle \tilde{V} \rangle = \sqrt{\frac{2}{\pi}} \int_0^{S/\sigma_N} \exp(-z^2/2)\, dz \tag{F11}$$

$$= \sqrt{\frac{2}{\pi}} \left[\frac{S}{\sigma_N} - \frac{1}{6}\left(\frac{S}{\sigma_N}\right)^3 + \cdots \right] \tag{F12}$$

so that

$$\langle \tilde{V} \rangle \approx \sqrt{\frac{2}{\pi}} \frac{S}{\sigma_N} \tag{F13}$$

if one neglects higher order terms. As indicated above, the maximum value of S/σ_N in our example will be about 0.35 so that the maximum of the cubic term will be about 2% relative to the first term (before tone stopping).

We are now prepared to analyze tone-stopping in the correlator. Let $\tilde{V}_k$ be the recorded signal at time t_k. For a given station, the correlator will counter-rotate (tone-stop) a given tone as follows

$$V_{sn} = \frac{1}{N_t} \sum_{k=1}^{N_t} \tilde{V}_k \exp(-i\psi_{nk}) \tag{F14}$$

where ψ_{nk} is the model phase for the n^{th} tone at time t_k and N_t is the number of sample points in the correlation interval. We will not take into account the fact that the BLKO correlator uses a trilevel quantized model for the stopping sinusoids. Such trilevel sinusoids possess higher-order harmonics that can cause problems if tones are not properly placed in the passband. A discussion of these problems is outside the scope of this report. Trilevel quantization also results in a slight decrease in SNR and a change in stopped-tone amplitude, but these effects are not significant in most applications. However, if absolute calibration of tone amplitude is desired, the amplitude effect must be considered.

Given Eq. (F13), the expectation value of the stopped tone given in Eq. (F14) can be calculated as follows:

$$\langle V_{sn} \rangle = \frac{1}{N_t} \sum_{k=1}^{N_t} \langle \tilde{V}_k \rangle \exp(-i\psi_{nk}) \tag{F15}$$

$$\approx \frac{1}{N_t} \sqrt{\frac{2}{\pi}} \sum_{k=1}^{N_t} \frac{S_k}{\sigma_N} \exp(-i\psi_{nk}) \tag{F16}$$

where S_k is the total tone signal S at time t_k. The neglected cubic term in Eq. (F12) can be represented as a sum of three-tone beat notes. One can show that during tone stopping a given three-tone beat note will be reduced to an insignificant level provided it possesses a different frequency than the original tone frequencies. If this condition is not satisfied, the offending three-tone beat note in a system with $\bar{v}/\sigma_N = 0.12$ could fractionally contribute in amplitude as much as

$$\frac{1}{4} * \frac{1}{6} \left(\frac{\bar{v}}{\sigma_N} \right)^2 \lesssim 0.0006 \tag{F17}$$

or 0.06% to the tone under consideration. Although this is not much by itself, many equally spaced tones can generate many three-tone beat notes near a given original tone frequency and the combined effect might be non-negligible. This problem will deserve more thorough study if many tones are ever used.

Based on the decomposition of S in the first term of Eq. (F2), the stopped tone in Eq. (F16) becomes

$$\boxed{\langle V_{sn} \rangle = \frac{1}{\sqrt{2\pi}} \frac{v_n}{\sigma_N} \exp[i(\phi_n - \psi_n)]} \tag{F18}$$

if we assume that the sum note and the other "high frequency" tones sum to negligible levels. The phase difference $\phi_n - \psi_n$, presumed to be nearly constant, is the phase difference at the middle of the sum interval. (We will assume stopped-tone frequency is negligibly small. If it is not, there are straightforward, simple ways to overcome the difficulty, such as the procedure used in the PCAL program described in Appendix G.)

The system noise on the stopped tone can be calculated as follows:

$$\sigma_V^2 = \left\langle \left(V_{sn}^R - \langle V_{sn}^R \rangle \right)^2 \right\rangle \tag{F19}$$

where V_{sn}^R is the real part of the stopped tone in Eq. (F14). Using Eq. (F14) one obtains

$$\sigma_V^2 = \frac{1}{N_t^2} \sum_{k\ell} \left[\langle \tilde{V}_k \tilde{V}_\ell \rangle - \langle \tilde{V}_k \rangle \langle \tilde{V}_\ell \rangle \right] \cos \psi_{nk} \cos \psi_{n\ell} \tag{F20}$$

These expectation values can be evaluated to obtain

$$\sigma_V^2 \approx \frac{1}{2N_t} \left[1 + \frac{2}{\pi} \sum_{\tau \neq 0} R(\tau) \cos 2\pi \nu_n \tau \right] \tag{F21}$$

where the sum is over all bits except $\tau = 0$, $R(\tau)$ is the bitstream autocorrelation function for the analog signals and ν_n is the baseband frequency of the n^{th} tone. This derivation assumes that interbit correlations of system noise are small. The first term represents the noise that would be present if there were no correlation between bits. The second term accounts for small correlations between bits and will be about 10% or less, the exact size depending on the shape of the bandpass, the sample rate relative to bandwidth, and the value of the baseband tone frequency ν_n. Note that, if the small second term can be neglected, the noise on a stopped tone is the same for all tones.

Stopped-tone SNR will be defined as the maximum amplitude (modulus of Eq. 18) of the stopped tone divided by the rms noise:

$$SNR = \frac{1}{\sqrt{2\pi}} \frac{\bar{v}}{\sigma_N} \frac{1}{\sigma_V} \tag{F22}$$

which through the use of Eqs. F5 and F21 becomes

$$\boxed{SNR \approx \sqrt{\frac{2\varepsilon N_t}{\pi N_h}}} \tag{F23}$$

where we have neglected the small interbit-correlation term in Eq. F21. In analogy with fringe phase calculations, the system noise error in the stopped-tone will be

$$\sigma_\phi = SNR^{-1} \quad (SNR >> 1) \tag{F24}$$

The following example will help illustrate the size of the system noise error in phase calibrator corrections. Again, suppose we have a 2% total power level for the calibrator signal with 3 tones across the passband. When 4 seconds of BLKO data (record rate = 4 Mbit/sec) are reduced for a given tone, we obtain from EQ. (F23)

$$\text{SNR} \approx \sqrt{\frac{2 \times 0.02 \times 4 \times 4 \times 10^6}{3\pi}} \approx 260 \tag{F25}$$

The associated phase error will be

$$\sigma_\phi \approx \frac{1}{260} \text{ rad} = 0.0006 \text{ cycle} \tag{F26}$$

This phase error is the system noise error in the phase from one tone. When fringe phase is calibrated, a number of tones (N_u) in the passband will probably be used, in which case the system noise error in the overall phase would be

$$\sigma_\phi^T \approx \frac{\sigma_\phi}{\sqrt{N_u}} \approx \sqrt{\frac{\pi}{2N_t\varepsilon}\frac{N_h}{N_u}} \tag{F27}$$

For our example, the overall phase error becomes

$$\sigma_\phi^T \approx 0.00035 \text{ cycle} \tag{F28}$$

if all 3 tones are used. For a 40-MHz spanned bandwidth in a bandwidth synthesis delay measurement, the corresponding delay error will be

$$\sigma_\tau \approx \frac{\sqrt{2} \times 0.00035 \text{ cycle}}{40 \text{ MHz}} = 0.012 \text{ nsec} = \frac{0.36 \text{ cm}}{c} \tag{F29}$$

The factor of $\sqrt{2}$ is a result of the combination of two channels in the BWS process.

Before closing the discussion of the calibrator signal, a more detailed description of tone amplitude is in order. If the ideal calibrator signal in Fig. 2 is decomposed into its harmonics, it can be shown that the amplitude of the n^{th} harmonic or tone will be given by

$$F_p(\omega_n) = C \frac{\sin(\omega_n \tau_p/2)}{\omega_n \tau_p/2} \tag{F30}$$

where tone frequency ω_n is a multiple ($n\omega_p$) of the nominal pulse rate ω_p and C is a constant determined by input power. With a pulse width of τ_p = 20 psec, the tone amplitude at X-band (8.3 GHz) will fall to about

$$F_p(\omega_x) \approx 1 - \frac{(\omega_x \tau_p/2)^2}{6} \approx 0.95 \qquad \text{(F31)}$$

which represents a loss of about 5% relative to the maximum amplitude at lower frequencies. The amplitude change across the passband at S- or X-band will be even smaller. For example, if the passband is 100 MHz, the amplitude change will be about 0.1% across the band at X-band. Thus, changes in tone amplitude across the passband due to pulse shape appear to be negligible for an ideal tone generator. Actual tone amplitudes might deviate considerably from the ideal behavior described here.

APPENDIX G

THE CURRENT METHOD FOR PHASE CALIBRATION

In the text, it is assumed that phase calibration is applied at an early stage in postcorrelation processing and that the correction is applied to the stopped fringes in the frequency domain by means of a frequency-specific counter-rotation of the phase in each correlation interval. However, the current BLKO system postpones phase calibration until a later stage of postcorrelation processing at which point a program called MERGE applies corrections to the composite values for phase, BWS delay, BSA delay and phase-delay rate that are passed by PHASOR. This version of phase calibration was coded first because it could be more easily incorporated into existing software. The composite interferometer observables are extracted as described in Section X except that the phase-tracked fringes are not subjected to phase calibration. A block diagram of the current data reduction steps is shown in Fig. G1.

To obtain tone phase, the stopped tones produced by the correlator are passed to a special phase-tracking program (PCAL). In close analogy with PHASOR, this program fits the stopped-tone signal in separate time intervals (sections) within an observation with a model in which the three solve-for parameters are amplitude, phase and phase rate. As in PHASOR, the solve-for parameters obtained for the various sections are combined to obtain for each parameter a composite value for the whole observation. For each tone, the composite amplitude, phase and phase rate are specified at a reference time and frequency near the center of the observation.

In general, tone phase cannot be subtracted from fringe phase directly because the reference times and frequencies of those phase values are different. First, tone phase is projected to the correct time using its measured phase rate; then calibration phase at the correct frequency is obtained by interpolating between the (time-corrected) phases of two tones. Typically, there are tones within ±0.5 MHz of the bandpass center. The resulting calibration phases are then subtracted from the composite fringe phase channel by channel to obtain a value for corrected fringe phase given theoretically by Eq. (77). For each observable, it should be understood that "subtracting" the tone values actually means subtracting the appropriate difference between stations, as in Eq. (64).

For phase-delay rate from a given channel, the composite tone phase-rate values are used to interpolate to the reference frequency, and the resulting value is subtracted from the composite interferometer phase-rate value. For BSA delay from a given channel, the composite tone phases from that channel must be analyzed to obtain the effective slope ("group delay") as a function of frequency. In the case of two tones per channel, the slope is simply computed as phase difference divided by frequency difference. As mentioned in Section VIII and as illustrated below, one must have initial crude values for the slope in each channel in order to resolve integer-cycle ambiguities in tone phase. The correction is then carried out by subtracting this tone group delay from interferometer BSA delay for that channel. Finally, for BWS delay, the time- and frequency-corrected calibration phase values from the channels are combined in pairs as in Eq. (81a) to form tone "BWS delays" which are then subtracted from corresponding interferometer BWS delays.

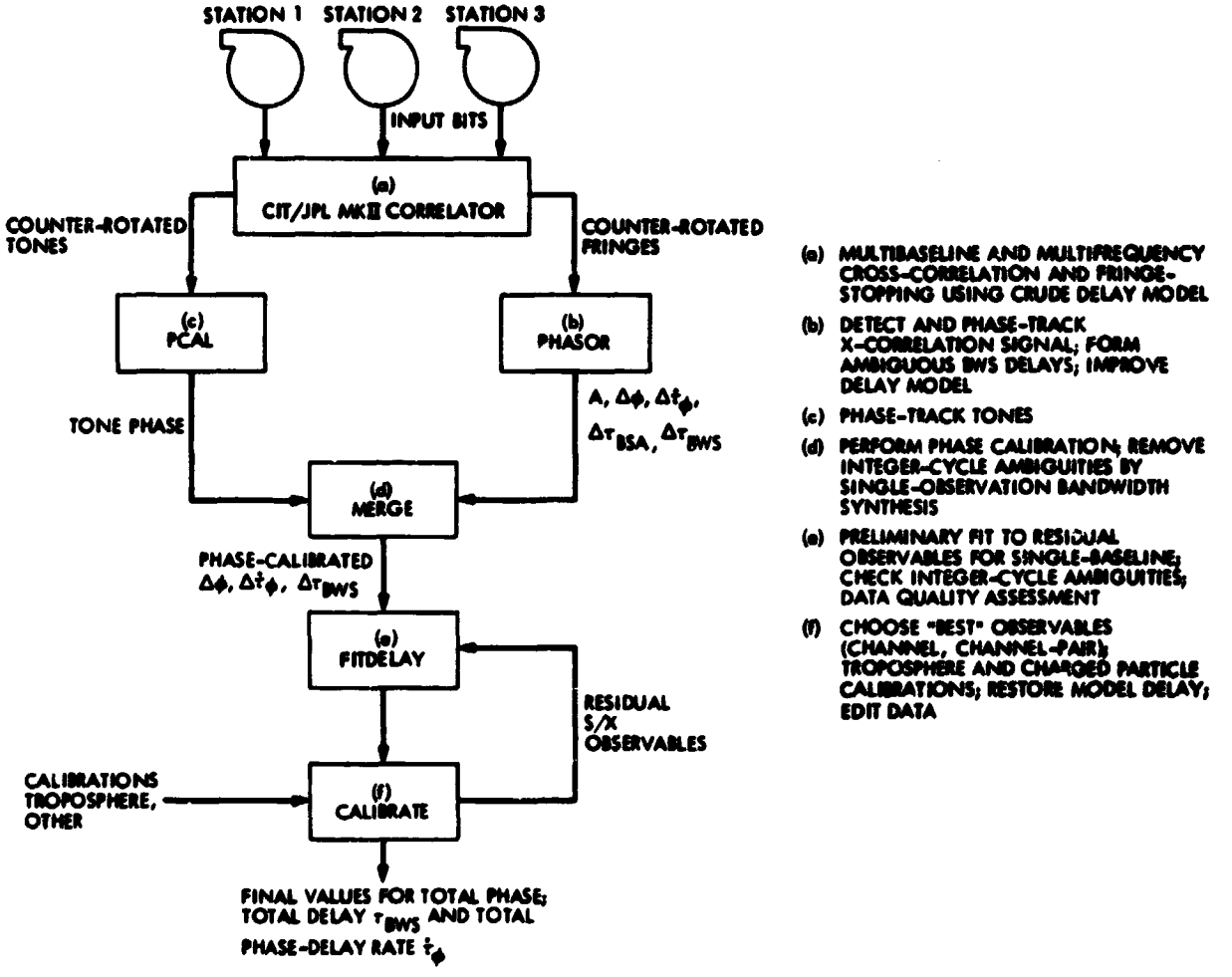

Fig. G1. Block diagram of present data reduction in the BLKO system

An example of the instrumental phase measured with tones is given in Fig. G2 for the BLKO system. The figure plots the phase for 19 tones in a 2-MHz bandpass recorded at DSS 43 for channel 1 in our example observation. Although many tones were processed in order to produce this figure, no more than three tones per passband can be processed for a two-antenna experiment if only a single pass is made through the correlator, as discussed in Appendix B. As indicated in the figure, a linear function of frequency has been subtracted from tone phase in order to reveal nonlinear effects introduced by the instrumentation. The large nonlinear trend that remains is due primarily to the narrowband IF-to-video converter. For this example, the total tone phase at the reference frequency (0.9 MHz) is equal to 1.285 cycle and is obtained by adding the indicated linear function to the plotted value. The time extrapolation mentioned above was negligible for this particular example since the reference time for tone phase was very close to that for the composite interferometer phase.

Another feature of phase calibration should be noted in this example. To reconstruct instrumental phase across the passband, one must resolve a slope ambiguity equal to $n/\Delta f$, where n is an unknown integer and Δf is the separation between the two closest extracted tones. For the present example, the ambiguity is 10 μsec so that only crude calibration of the instrumental delays discussed in Section VIII is necessary to remove the slope ambiguity. Calibrations by L. E. Young give approximate values[2] for the three delays in Eq. (62):

(a) the epoch difference in the recorder clock and the ϕ-cal clock = $\tau_{bj} - \tau_{cj} \approx 5$ μsec,

(b) the delay ("cable delay") from the clock reference point (ϕ-cal clock) to the ϕ-cal injection point = $\tau_{uj} \approx 1.5$ μsec,

(c) the delay from the injection point to the recorder = $\tau_{Ij} \approx 2.4$ μsec.

These terms give a slope of $-(\tau_{bj} - \tau_{cj} + \tau_{uj} + \tau_{Ij}) = -9$ μsec. We will ignore the correlator reference time t_s since, in this example, t_s is an integer multiple of 1 second and all tone frequencies and the reference frequency are integer multiples of 1 hertz. Thus, the resulting products of time and frequency each contribute integer cycles at desired sample points,

---

[2]The offset between the recorder clock and the ϕ-cal clock, $\tau_b - \tau_c$, is obtained by subtracting the offsets separately measured for those two clocks relative to the station 1 pps. When τ_c is measured, one must make certain that the ϕ-cal clock is based on the particular subset of positive-going zero-crossings (at the reference point discussed in Section III) that are allowed to become pulses at the output of the tone generator. Since, in our example, every 50th zero-crossing of a 5-MHz signal is converted to a pulse, the separation between passed pulses is 10 μsec. This pulse separation is related to the 10-μsec slope ambiguity for tone phase, which is due to the ambiguity in time tags for the "pulse-generating" zero-crossings at the reference point. Once those time tags have been assigned, τ_c can be determined and the slope ambiguity can be worked out, as will be illustrated.

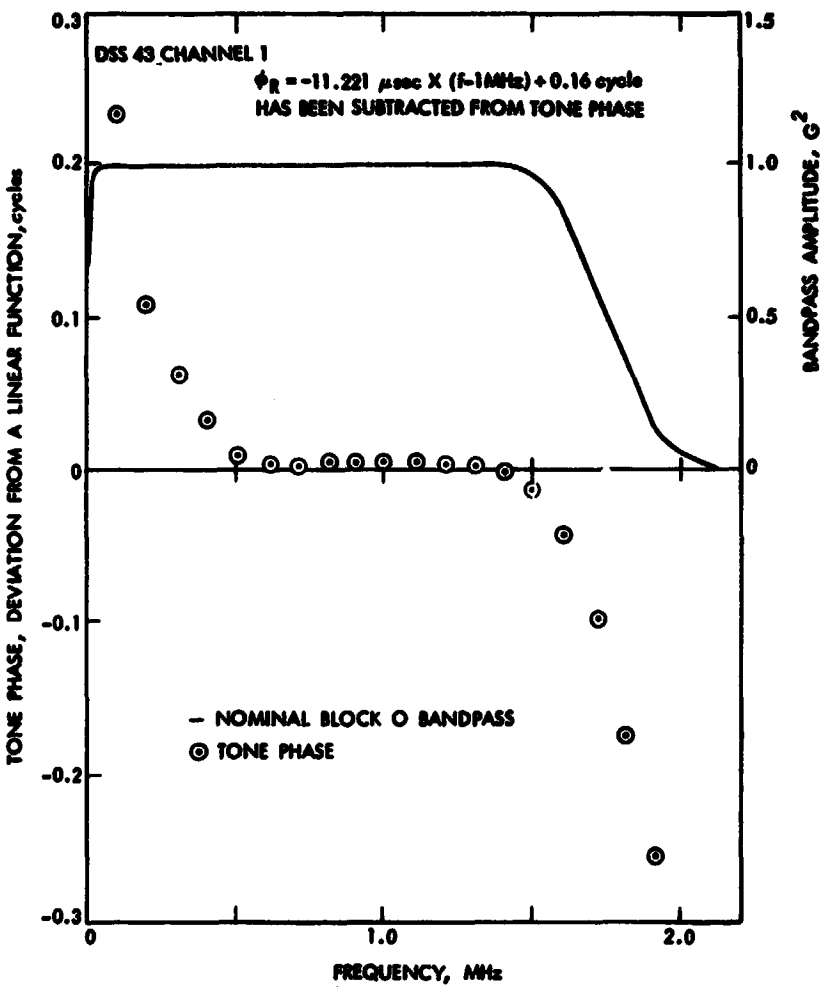

Fig. G2. An example of stopped tone phase in the BLKO system

G-2

which would increment the slope in steps of 10 μsec. As shown in Section IX, the t_s term in the slope disappears in the difference between stations anyway. In addition to these modeled delays, the artificial method used in the correlator for tone extraction introduces another unmodeled delay of 2.5 μsec, which brings the total slope to about -11 μsec. This a priori estimate of slope clearly selects as the closest ambiguity in slope the value -11.221 μsec, given that the ambiguity spacing is 10 μsec. (Although the unmodeled delay introduced by the correlator does impact single-station phase and slope determination, its effects cancel in the difference between stations and will therefore be ignored after this point.)

Nonlinear trends as large as those in Fig. G2 can lead to significant errors in phase calibration. For the reference frequency approach presented above, the true composite phase effect obtained by integrating across the passband can differ considerably from the observed phase at the reference frequency, as suggested by the asymmetrical weighting imposed on the large nonlinear phase excursions at the bandpass edges. Further, the slope (BSA delay correction) obtained by using two points in the central part of the bandpass will not be as steep as the actual "average" slope of phase. However, the actual errors in composite phase and slope are not as bad as this example suggests since an interferometer forms the difference in phase between antennas and the above single antenna errors will cancel to the extent that the system bandpasses of the stations are identical. For BWS delay, further cancellation can take place between channels at the same station. It is beyond the scope of this report to assess the magnitude of phase calibration errors. The next generation system, the BLOCK II system, will reduce such errors through the use of more tones.

Although the specific calculations will not be presented here, the composite tone phase extracted for channel 3 at DSS 43 for the same observation was equal to 1.007 cycle at the reference frequency. The results for the two channels can now be combined to obtain the DSS 43 tone correction for BWS delay for the (1,3) channel pair:

$$\Delta\tau = \frac{(1.285 - 1.007)\ \text{cycle}}{(2276 - 2271)\ \text{MHz}} = 55.6\ \text{nsec} \qquad \text{(G1)}$$

The same calculation can be carried out for the other station (DSS 14 in the example observation) to yield a BWS delay correction for that antenna. The results for the two antennas will be used in the next section in an illustration of single-observation bandwidth synthesis.

APPENDIX H

SINGLE-OBSERVATION BANDWIDTH SYNTHESIS

One of the goals of VLBI measurements is the precise determination of delay (i.e., $\Delta\tau_f$ in Eq. 77). One can easily show that system noise error in delay is inversely proportional to the highest frequency (for phase-delay) or frequency spread (for BWS delay) in the observed spectrum, provided integer-cycle ambiguities in the associated phase or phase difference can be removed. The BSA delay τ_s is based on the continuous single-channel bandpass and becomes an unambiguous estimate of $\Delta\tau_f$. However, since this bandpass is relatively narrow (2 MHz), the BSA delay is relatively imprecise. By comparison, the phase delay (ϕ_s/ω_z), which is at RF, is an extremely precise measurement of delay except for an integer-cycle ambiguity. One method for covering the range between these two extremes in frequency without integer-cycle ambiguities is bandwidth synthesis. In the BLKO bandwidth synthesis technique, one measures interferometer phase at selected frequencies (i.e., channels at $\omega_z = \omega_a, \omega_b \cdots$) and then iteratively removes the ambiguities in the difference phase between successively larger channel separations.

This appendix describes single-observation bandwidth synthesis, rather than multi-observation synthesis as outlined by Purcell (Ref. 6). When phase calibration is available, as assumed in this report, one can resolve the ambiguities in phase by using only the information found within each observation. Without phase calibration, one must use a multi-observation approach that removes ambiguities only in a relative sense by comparing adjacent observations. The single-observation approach with phase calibration is preferable since it is simpler and faster and produces an absolute measurement of delay that allows clock synchronization measurements.

The original approach to single-observation bandwidth synthesis, as developed by A.E.E. Rogers [4], is based on coherent addition of the fringes from the recorded channels within an RF band. In contrast, the BLKO approach is based on the separate extraction of phase for each channel and the explicit manipulation of those phase values to obtain BWS delay. This single-channel-extraction approach can be carried out without phase calibration [6], which was a necessary capability in the early stages of BLKO development.

The BLKO single-observation approach relies on two conditions. First, except for cycle ambiguities, the BSA delay and all channel-pair BWS delays must be approximately equivalent in expectation value. (Compare Eq. 74 and Eq. 81b.) Second system noise error in channel phase must be much less than one cycle (in practice, $\sigma_\phi \lesssim 0.03$ cycle). In this appendix, we will neglect charged particle effects and will also assume that dispersive effects before the tone-injection point can be calibrated. Although charged particle effects violate the first condition in the strictest sense, the condition is adequately met for spanned bandwidths of the order of 100 MHz or less at S-band.

When these conditions are met, single-observation bandwidth-synthesis proceeds as follows. After extracting the phase for each channel, one computes a composite BWS delay for each channel pair from the difference phase between channels as described in Section XII. The computed delays will possess integer-cycle ambiguities as represented by the last term in Eq. 81b. These ambiguities

in delay are removed by iteratively proceeding from the unambiguous but imprecise BSA delay to the BWS delay of the most widely spaced channal-pair, using at each step the result generated by the preceding channel pair. At each step, one computes the number of cycles that must be added to the k^{th} BWS delay to place it within ± 0.5 cycle/Δf_k of the $(k-1)^{th}$ delay, where Δf_k is the frequency separation for the k^{th} channel pair.

As an illustration of the bandwidth synthesis process, Table H1 presents for our example observation (see Figs. 3, 5 and 6) the BSA delay and the three BWS delays obtained at five stages in the phase calibration and bandwidth synthesis process: (a) the uncorrected delays derived from the fringes (PHASOR output), (b) and (c) the delay corrections derived from tone phase (PCAL output) for each antenna, (d) the phase-calibrated but ambiguous delays, and (e) the final unambiguous delays. For simplicity, only the BSA delay from channel 1 is used, although averaging all three S-band channels should improve the BSA delay determination. The tone BSA delay for each antenna was obtained from the phase-frequency slope of tone phase, which was equal to -11.221 μsec for the example of DSS 43 in Fig. G2. An example calculation of tone BWS delay was given in the preceding appendix for channels 1 and 3 for DSS 43. When the delay corrections are combined with the uncorrected delays, one obtains delays that are ideally free of unwanted instrumental effects but possess integer-cycle ambiguities. As discussed above and as schematically indicated in Fig. H1 for a hypothetical observation with low SNR, single-observation bandwidth synthesis can now be applied by iteratively removing ambiguities while progressing from the leftmost to the rightmost value for delay in Table H1. The final value for each of the four delay observables should be the residual delay given theoretically by the combination of delays in Eq. (77). Note that, while the final delay values for the various channel pairs in Table H1 agree fairly well, they are not in agreement at the system noise level, as one might hope. This disagreement is probably a consequence of one or more of the following dispersive effects: (a) improperly calibrated nonlinear trends in the phase-frequency response of the instrumentation (see preceding appendix), (b) dispersive effects in the input tones and (c) dispersive effects such as multipathing before the tone injection point. It is outside the scope of this report to estimate such errors. However, it should be pointed out that the differences between BWS delays are not necessarily an indication of the error that will be propagated to geophysical/astrometric parameters since large components of the differences would be constant and those components would therefore be absorbed by the clock parameter during multiparameter estimation.

A parameterized error analysis of the above BWS process leads to an associated method for computing a channel placement that helps in minimizing the number of inner channels and thereby increases precision. In this particular method, it is assumed that a priori information is too poor to help with any step in the ambiguity resolution process (except tone phase slope). To reliably compute integer cycles for the $(k+1)^{th}$ channel pair, the error (σ_k) in the delay for the k^{th} channel pair and the frequency separation (Δf_{k+1}) for the $(k+1)^{th}$ channel pair must satisfy the relation

$$\Delta f_{k+1}\, \sigma_k \leq \frac{0.5 \text{ cycle}}{3} \qquad \text{(H1)}$$

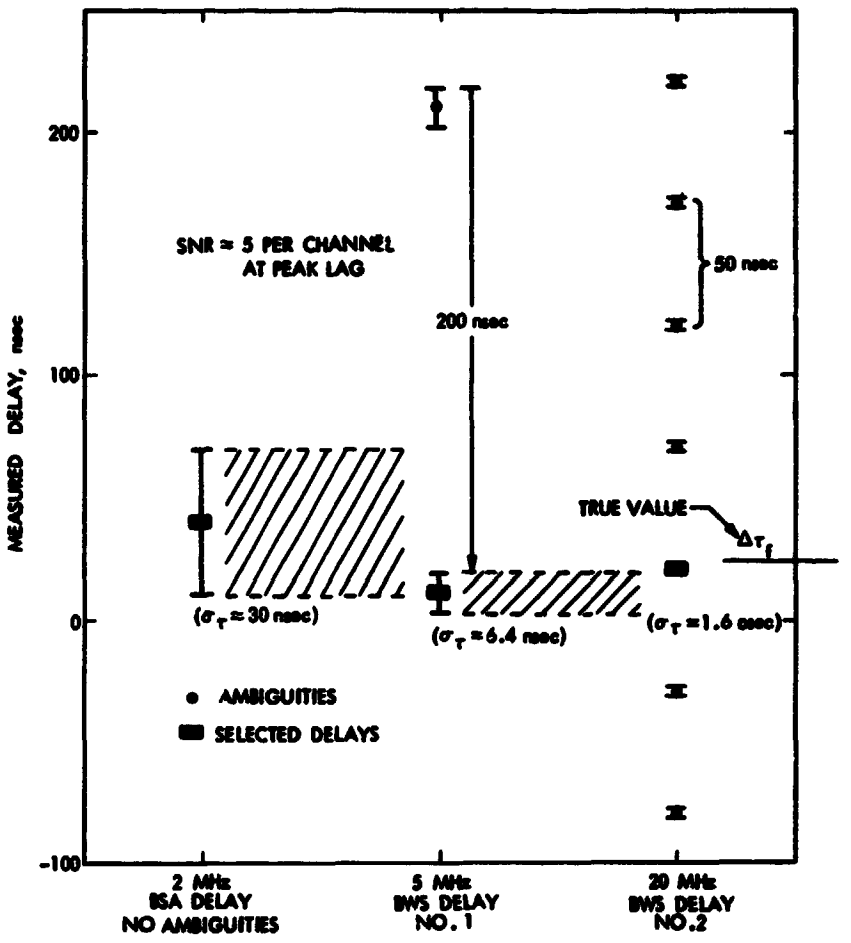

Fig. H1. Schematic example of ambiguity resolution in the BLKO system

Table H1. An example of phase calibration and single-observation bandwidth synthesis with the present BLOCK 0 system

Step \ Observable[a]	BSA delay Channel 1	BWS delay 1 Ch 1 - Ch 3, Δf = 5 MHz	BWS delay 2 Ch 1 - Ch 2 Δf = 23.2 MHz	BWS delay 3 Ch 2 - Ch 3, Δf = 28.2 MHz	
Uncorrected delays, DSS 14/DSS 43 (D_u)	170 ± 9 (see Fig. 3)	190.5 ± 1.4	-26.97 ± 0.29	11.58 ± 0.21 (see Fig. 6)	← PHASOR Output
Delay corrections from tones, DSS 14 (C_{14})	-5200 ± 3.6	135.8 ± 0.3	-17.50 ± 0.07	9.66 ± 0.06	Computed from PCAL Output
Delay corrections from tones, DSS 43 (C_{43})	-11221 ± 1.8 (see Fig. 13)	55.6 ± 0.2 (see Appendix G)	-14.31 ± 0.05	-1.95 ± 0.04	
Corrected but ambiguous delays, DSS 14/DSS 43 ($D_a = D_u - C_{14} + C_{43}$)	-5851 ± 10 ↓ unambiguous	110.3 ± 1.5 $+ \frac{n_1}{5\ \text{MHz}}$	-23.8 ± 0.30 $+ \frac{n_2}{23.2\ \text{MHz}}$	-0.03 ± 0.22 $+ \frac{n_3}{28.2\ \text{MHz}}$	
Unambiguous final observables ($\tau_g' + \tau_c + \tau_a - \tau_u - \tau_m$)	-5851 ± 10	-5889.7 ± 1.5 ($n_1 = -30$)	-5885.9 ± 0.30 ($n_2 = -136$)	-5886.6 ± 0.22 ($n_3 = -169$)	← Remove Ambiguities

[a]Relative to central lag of correlator in nanoseconds. Errors are system noise errors. Channel reference frequencies are (f_1, f_2, f_3) = (2276, 2299.2, 2271) MHz.

where the factor of 3 serves to insure a 3σ probability of success. The error in delay for the k^{th} pair is given by

$$\sigma_k = \frac{\left(2\sigma_s^2 + 4\sigma_\phi^2\right)^{1/2}}{(2\pi\ \Delta f_k)} \tag{H2}$$

where σ_s is the system noise error in phase (in radians) for a single channel (but involving two stations) and σ_ϕ (radians) is equal to the RSS of all other dispersive errors in phase for a single channel from one station. The term $2\sigma_s^2$ accounts for two channels while $4\sigma_\phi^2$ accounts for two channels at two stations. For simplicity, we assume that dispersive errors have the same magnitude for both stations and all channels and are uncorrelated between channels. The system noise error in phase (radians) for a single-sideband system is given by

$$\sigma_s = \frac{1}{\sqrt{2}\ SNR_s} \tag{H3}$$

where SNR_s is the SNR at peak fringe amplitude in the given channel. The factor of $\sqrt{2}$ fringe is the improvement in phase precision resulting from the use of all lags for the channel.

Inserting the last two equations into Eq. (H1), one obtains an expression for the maximum allowed ratio (R) of channel separations (frequency multiplier):

$$\frac{\Delta f_{k+1}}{\Delta f_k} \leq R \tag{H4}$$

where

$$R \equiv \frac{\pi}{3}\ \frac{1}{\left[SNR_s^{-2} + 4\sigma_\phi^2\right]^{1/2}} \tag{H5}$$

and where σ_ϕ is still in radians.

Given the single channel SNR and the other dispersive errors in phase, one can easily compute the frequency multiplier. Given the multiplier and the separation of the first channel pair, one can compute the successive channel separations. However, the actual spread can increase somewhat more rapidly than the above multiplier implies. As illustrated in Fig. H2, pair 2 (comprised of channels 2 and 3) is given a separation of $\Delta f_2 = R\Delta f_1$ where Δf_1 is the separation of pair 1 (channels 1 and 2). The separation of pair 3 (channels 1 and 3) is then given by $\Delta f_3 = (R+1)\Delta f_1$. When a fourth channel is added, pair #4 (channels 3 and 4) is given a separation of R times the largest previous separation or $\Delta f_4 = R\Delta f_3 = R(R+1)\Delta f_1$. The separation of pair 5 (channels 1 and 4) then becomes $\Delta f_5 = (R+1)^2\Delta f_1$. Continuing this process, one finds that the outer pair separation for a system with N_c channels would be given by $(R+1)^{N_c-2}\Delta f_1$.

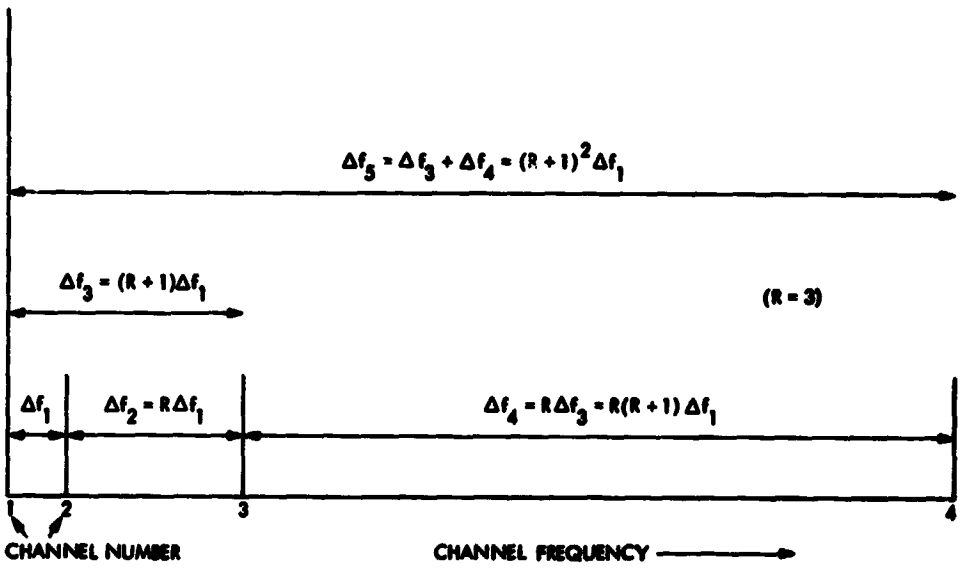

Fig. H2. An example of the geometric progression approach to BWS channel placement

This leaves us with the problem of specifying the maximum allowed separation of pair 1 in terms of the channel bandwidth. The delays obtained from bitstream alignment are based on the continuous channel bandpass and are therefore unambiguous. These delays can be used to initiate the BWS process by resolving the cycle ambiguity in the first channel pair, provided the separation of the first pair is not too large. Without presenting all of the details, we will state here that a rough estimate for the multiplier from channel bandwidth to the first channel pair is given by $\Delta f_1 = R/1.8$, where R is computed by Eq. (H5). (The factor of 1.8 comes from (a) the fact that the continuous channel bandpass makes inefficient use of bits relative to the case where all bits are at the edges of the bandpass, and (b) the fact that tones placed within the channel bandpass for intrapassband phase calibration would not be placed at the bandpass edges but would be displaced inward by a safe amount.)

Combining the above results, one obtains an expression for the separation (Δf_M) of the most widely spaced pair in terms of the channel bandwidth (W) and the number (N_c) of channels:

$$\boxed{\frac{\Delta f_M(N_c)}{W} \approx \frac{R}{1.8}\,(R+1)^{N_c-2}} \qquad \text{(H6)}$$

Relative to the first reference channel, the channel frequencies in units of the channel bandwidth would be

$$0,\ \frac{R}{1.8},\ \frac{R}{1.8}\,(R+1),\ \frac{R}{1.8}\,(R+1)^2,\ \ldots\ \frac{R}{1.8}\,(R+1)^{N_c-2} \qquad \text{(H7)}$$

For convenience, the curves connecting $\Delta f_M(N_c)$, R and N_c are plotted in Fig. H3. The right-hand vertical axis gives the total allowed dispersive phase error (numerator in Eq. H2) associated with each frequency multiplier R on the left-hand vertical axis. When using the graph to compute the required number of channels for a given spanned bandwidth and given frequency multiplier, one must adopt the next higher value of N_c, if the point falls between two curves of constant N_c.

The BWS approach outlined above is not optimal for all applications. For smaller values of the frequency multiplier ($R < 5$), the basic assumptions behind Eq. H6 (e.g., single-channel detection) can be violated. Further, if good a priori information for delay is available, it may be possible to omit some or all of the inner channels required for ambiguity resolution. More generally, totally different techniques can be used in postcorrelation data reduction. For example, if detection and estimation were carried out through coherent addition of BWS channels (Ref. 4), then one might choose to place the channels across the RF band in a pattern based on detection capability in addition to final delay precision.

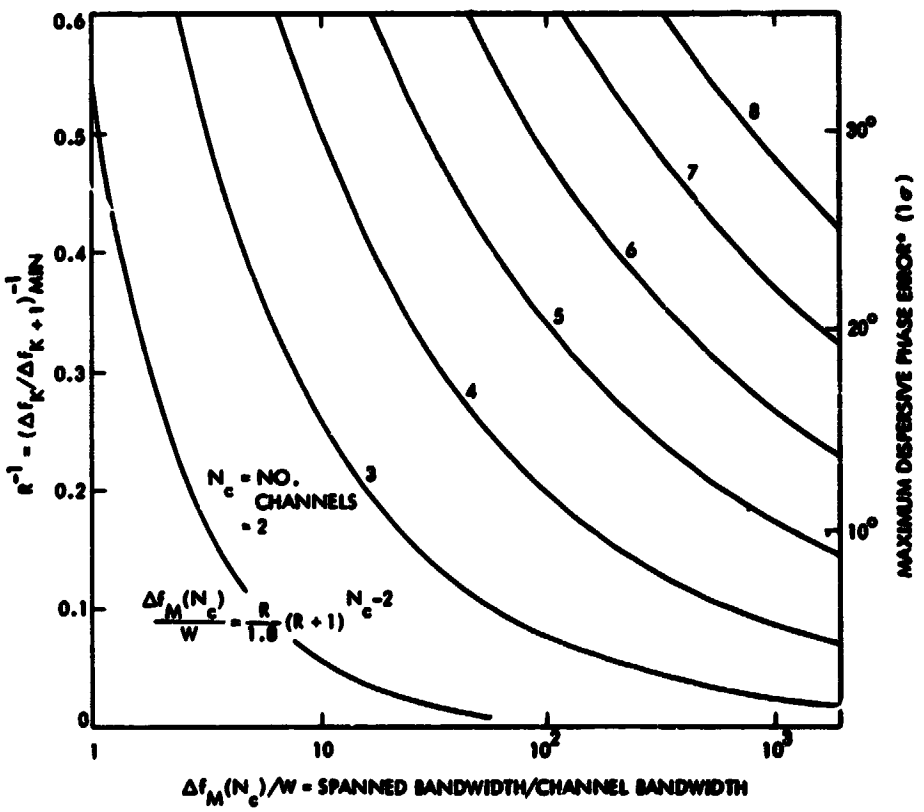

Fig. H3. The relationship between spanned bandwidth, BWS frequency multiplier and number of channels

APPENDIX I

GEOMETRIC TIME DELAY

This appendix derives an expression for the geometric delay in terms of station locations and source direction.

Suppose two antennas simultaneously receive the signal from a very distant point source. The difference in the arrival times at the two stations is referred to as the geometric delay. Due to the great distance of the source, the signal can be represented as the plane wave in Eq. (7). All quantities will be referenced to geocentric coordinates in a nonrelativistic analysis.

Let a particular wavefront reach station i at true time t_i'. This segment will reach station j at true time t_j' when the following phase equality is satisfied.

$$\vec{k}\cdot\vec{x}_i(t_i') - \omega t_i' = \vec{k}\cdot\vec{x}_j(t_j') - \omega t_j' \tag{I1}$$

Let $t_j' = t_i' + \tau_g$, where τ_g is the geometric delay. Rearranging Eq. I1, we obtain

$$\omega\tau_g = \hat{k} \cdot [\vec{x}_j(t_i'+\tau_g) - \vec{x}_i(t_i')] \tag{I2}$$

This equation defines τ_g in terms of station location and source direction but it is not computationally convenient. An accurate approximation can be used to obtain a more tractable form. Since τ_g is small ($\lesssim$0.02 sec for earth-fixed antennas), expand $\vec{x}_j$ about t_i' to obtain

$$\vec{x}_j(t_j') = \vec{x}_j(t_i') + \dot{\vec{x}}_j\,\tau_g \tag{I3}$$

One can now use Eq. (I2) to solve for τ_g:

$$\boxed{\tau_g(t_i') = \frac{\hat{k}\cdot\vec{B}(t_i')}{c}\left[1 - \frac{\hat{k}\cdot\dot{\vec{x}}_j(t_i')}{c}\right]^{-1}} \tag{I4}$$

where $\vec{B}$ is the baseline vector given by

$$\vec{B}(t_i') = \vec{x}_j(t_i') - \vec{x}_i(t_i') \tag{I5}$$

As one would expect, the geometric delay is simply the instantaneous path difference divided by the speed of light with a small correction for the motion of station j during wave transit. As noted in the text, this definition of the geometric delay uses station i as the reference station. That is, if a segment

of the wave strikes station i at time t_i', then that segment will reach station j at time $t_i' + \tau_g(t_i')$, where the time tag for τ_g is the arrival time at station i.

A comment concerning the meaning of antenna position is in order. It is customary to make the "intersection" of the two axes of rotation the point that defines the location of an antenna. Even though the signal is not received at that point, corrections can be applied to the observed delays to make this point the effective point of reception. Two types of correction are required. The first is a correction applied only to those antennas for which the axes do not, in fact, intersect, as in a DSN equatorial mount. This correction depends on pointing direction, and it, in effect, shifts one of the axes of rotation in order to define a fictitious but earth-fixed point of intersection. The second correction is a constant delay correction to account for the fact that the signal is actually received at the feed rather than at the intersection of axes. This correction is equal to the difference between the transit time that a wave would experience in its actual propagation to the injection point and its theoretical transit time to the intersection of axes. This correction is nominally the same for all sources since the antenna always points toward the source and therefore always presents the same geometry in the propagation direction. For very accurate measurements, this correction may not be constant but may depend on pointing direction.